Neurovascular coupling in a central nervous system white matter tract

Dissertation

for the award of the degree
“Doctor of Philosophy (Ph.D.)”
Division of Mathematics and Natural Sciences
of the Georg-August-Universität Göttingen

within the doctoral program *(Neurosciences)*
of the Georg-August University School of Science (GAUSS)

submitted by

Alejandro Restrepo Arango

from

Bogotá, Colombia

Göttingen 2022

Thesis Advisory Committee

Prof. Dr. Klaus-Armin Nave
Department of Neurogenetics
Max Planck Institute for Multidisciplinary Sciences

Prof. Dr. Susann Boretius
Functional Imaging Laboratory
German Primate Center

Dr. Nuno Raimundo
Department of Cellular and Molecular Physiology
Penn State College of Medicine

Members of Extended Thesis Advisory Committee

Prof. Dr. Dr. Hannelore Ehrenreich
Clinical Neuroscience
Max Planck Institute for Multidisciplinary Sciences

Prof. Dr. med. Frauke Alves
Translational Molecular Imaging
Max Planck Institute for Multidisciplinary Sciences

Prof. Dr. Luis Pardo
Oncophysiology Group
Max Planck Institute for Multidisciplinary Sciences

Date of oral examination: 20.06.2022

Herewith I declare that I prepared this Doctoral Thesis, entitled “Neurovascular coupling in a central nervous system white matter tract”, on my own and with no other sources and aids than quoted.

Göttingen, 2022 Alejandro Restrepo Arango

“Le biologiste passe, la grenouille reste”

Jean Rostand

To my family

Acknowledgments

I would like to thank Prof. Klaus-Armin Nave for giving me the opportunity and the means to embark on this project. His often devil's advocacy always pushed me to read and explore more than what I thought was necessary.

I am very grateful to Iva D. Tzvetanova for guiding me at the beginning of my Ph.D. and teaching me all there is to know about cell culture. Our constant discussions helped me learn how to think when designing experiments.

I want to give a huge thank you to Andrea Trevisiol for discussing my project every time that was necessary, for letting me use your electrodes, for always pushing me to do my best, and for introducing me to the set-up that has proven invincible over so many years. Maybe we should put it to rest now.

I would like to thank Prof. Boretius and Dr. Raimundo for their suggestions and useful advice during the annual presentations of my thesis. I would like to thank as well Renate Schweizer for her enthusiasm, help, and guidance with the fMRI experiments.

This Ph.D. would not have been possible without the amazing and huge help of the IMPRS Neuroscience office, especially with all the support and organization from Sandra Drube. All the help received from them does not go unnoticed. Thank you.

Monsieur Bacqué, pas mal ou pas terrible?

I am very grateful to all the people at the institute who supported me with technical help. Sarah Schulze, Connie Casper, Anke Schräpler, and Ursula Fünfschilling from the animal facility. Miso Mitkovski and Heiko Röhse from the light microscopy facility. Lothar Demel, Hajo Horn, Rolf Merker, Harry Scherer, and Martin Arnemann for their technical help.

A big thank you goes to Ulli Bode, Ushi Kutzke, and Gudrun Fricke-Bode for their help with the most cryptic and inexplicable technique invented by mankind, the PCR.

Suffering alone is not as fun as suffering together with more people, so thank you to all the friends that helped me in one way or another, that shared the results of bad or good experiments with me, that shared food or drinks at some point during the long days and nights, that provided me with the daily gossip or daily joke, that complained about science, academia, or the world. Thank you, Andrew, Constanze, David, Diego, Ebrahim, Kashish, Katarina, Lena, Lina, Lisa, Luis, Nicolás, Özge, Sebastian, Sharlen, Sophie, and Ting.

Although I never explained what I was working on to my family, they always supported me, no matter what hairstyle I was rocking. They always helped me and tried to cheer me up, so I would like to express my most sincere appreciation to them. Thank you for providing me with everything I needed, always.

Sonja, thank you for your invaluable support, for all the softness, for everything.

TABLE OF CONTENTS

ABSTRACT

Neurovascular coupling is the process by which blood vessels dilate upon increased neuronal activity. It has been extensively studied in the murine grey matter and there are several models explaining possible molecular and cellular pathways that communicate neuronal needs to the vascular system. However, neurovascular coupling in the white matter, which represents half of the human brain, has been constantly overlooked. I used the optic nerve as a model system to study neurovascular coupling in white matter. In the optic nerve, spiking axons release glutamate into the periaxonal space. Glutamate activates NMDA receptors located in the myelin membrane, and oligodendrocytes increase their glycolytic metabolism to support the ATP production of the underlying axon. This process of neurometabolic coupling requires that the vascular system matches the axonal activity and increases the availability of glucose and oxygen. How this is done in the white matter remains elusive. My experiments show that axonal activity induces a small vessel dilation which is both prolonged and sustained for more than 20 min after the end of the stimulation. Pharmacological inhibition suggests that the electrically-evoked dilation is mediated by the prostaglandin E2 receptor EP_4 and can be modulated by oxygen concentration. These experiments demonstrate that some of the principles that govern the response of the grey matter are also in place for the white matter. By using neurogenetics, I show that the vessel dilation is partially mediated by oligodendroglial NMDA receptors, supporting the published white matter neurometabolic model. A preliminary study using task-based fMRI immediately followed by a long resting-state fMRI shows a positive and strong BOLD signal in the corpus callosum during the resting state only when the task was performed. These data suggest that white matter neurovascular coupling is a process that mainly happens after the neuronal activation has finished, hinting that neurovascular coupling in white matter is necessary to replenish the energy stores that have been used, and not to support the axonal activity.

INTRODUCTION

The brain is a highly energy-demanding organ that depends on external energy sources for its function. These energy resources are transported and distributed through a system that is very often overlooked. The vascular system is responsible for delivering, mainly glucose and oxygen, to the almost 80 million neurons of the murine brain, and for the collection of their metabolic waste. It is of great importance to understand how the vascular system is connected to the other cells in the brain, particularly glial and neuronal cells.

1. NEUROVASCULAR AND OLIGODENDROGLIAL DEVELOPMENT IN THE CENTRAL NERVOUS SYSTEM AND THE OPTIC NERVE

The following section describes very briefly, the development of the vascular, neuronal, and glial cells in the murine brain.

1.1. Vascular development

The vascularization of the Central Nervous System (CNS) starts with the sprouting of vessels from the perineural vascular plexus between embryonic days (E) 8.5 and E10. At E9, superficial pial blood vessels enter the parenchyma (Vasudevan et al., 2008) and by E10.5 a vast network with arterial and venous hierarchy expands towards the ventricles by different processes such as vessel sprouting, endothelial cell proliferation, vessel regression, and stabilization (Carmeliet and Jain, 2011; Vasudevan et al., 2008). The vascular network continues growing with great plasticity until the first month of age (Harb et al., 2013). Importantly, the endothelial cells, which constitute the lining of the blood vessels, reach a proliferation peak at postnatal day (P) 10 (Harb et al., 2013).

As the optic nerve is heavily used during my work and is part of the CNS, I will particularly focus on its development. The optic cup is fully developed by E13, and the optic nerve stalk is recognizable from the same day (Sefton et al., 1985). Numerous blood vessels are found around the cup and the evidence shows that they remain and form the vasculature of the retina. However, the optic nerve development seems to not be dependent on blood vessels since the invasion of the nerve by blood vessels and connective tissue starts postnatally (Kuwabara, 1975).

1.2. Neuronal development

The neurons in the brain are formed by progenitor cells that come from the subventricular zone and migrate to the pial surface of the developing brain in an inside-to-outside manner. The progenitor cells migrate via radial and tangential migration, using radial glia as migratory scaffoldings (Budday et al., 2015). The cortical layers are formed first, between E11.5 and E17.5 (Molyneaux et al., 2007), followed by all subcortical regions.

In the retina, the retinal ganglion cells are the first neurons to develop in the outer retinal layer. By E13, the axons of the retinal ganglion cells are growing in the optic stalk towards the brain and by E14, the inner layer of the retina is filled with the somata of the ganglion cells (Kuwabara, 1975; Sefton et al., 1985). At this point, there are no glial cells present in the extracellular space in-between axons. The neuronal development in the optic stalk is a very rapid process. From E14 until birth, the axons grow to form bundles filling the space of the optic nerve, but are restricted by the formation, proliferation, and differentiation of glial cells. The axons will only be myelinated during the first postnatal week (Kuwabara, 1975; Sefton et al., 1985).

1.3. Oligodendrocyte development and myelination

Oligodendrocytes, the myelinating glial cells of the brain, are formed by the differentiation of oligodendrocyte progenitor cells (OPCs). During development, OPCs expand in three waves that start from different areas of the developing brain (Kessaris et al., 2006). The first wave, which is sonic hedgehog dependent (Orentas et al., 1999), starts at E12.5 by inducing the expression of the transcription factors *Olig1* and *Olig2* in precursors cells at the medial ganglionic eminence (Goldman and Kuypers, 2015). These new OPCs migrate to the dorsal forebrain. Three days later, at E15.5, the second wave of OPCs is formed and migrates to what will become the cerebral cortex. This second wave increases the number of OPCs by a factor of 3 (Tsai et al., 2016). At birth, both populations of OPCs are replaced by the third wave that originates from cortical precursor cells that express the homeobox gene *Emx1* (Goldman and Kuypers, 2015; Kessaris et al., 2006; Rowitch and Kriegstein, 2010).

In the optic nerve, cells from the stalk wall start to proliferate and divide at E15. The first cells to proliferate will differentiate into astrocytes that extend long processes into the axonal bundles and segregate them into groups. A few days later, other cells emerge in the extracellular space which will form oligodendrocytes. At P8 and P9, oligodendroglial processes expand and surround bundles of axons, forming the first signs of a future myelin sheath. By the end of the third postnatal week, all myelinated axons of the optic nerve will remain for the rest of the lifespan of the mouse. Non myelinated axons will degrade (Kuwabara, 1975).

Interestingly, the peak for endothelial cell proliferation coincides with the beginning of myelination in the corpus callosum in mice suggesting a coupling between energy availability and energetic needs. In this case, the metabolic need for myelination is only met by the blood vessels at P10 (Harb et al., 2013; Sturrock, 1980). Indeed, the coupling between the vascular system and the oligodendroglial cell lineage is more complex than just offer and demand.

2. BRAIN ENERGY METABOLISM

The CNS is used to record, process, store and reproduce information. These are very energetically expensive processes that need a constant and very fine-tuned energy supply. Any disturbance in the energy supply can cause brain damage, even in a small period of time as short as 5 to 10 min (Richmond, 1997). Twenty percent of the basal oxygen consumption of a human adult body is used by the brain, which represents only 2% of the total weight (Sokoloff, 1992). In infants, when the brain is still developing, the oxygen consumption by the brain can increase up to 50% of the total basal oxygen consumption (Clarke and Sokoloff, 1999). The majority of that oxygen will be used for the oxidation of carbohydrates (Clarke and Sokoloff, 1999) to produce adenosine triphosphate (ATP), the metabolic currency of the cells.

The CNS can be divided into two regions based on their coarse appearance, so called white and grey matter. They have different properties and different functions. Neuronal cell bodies, synapses, and glial cells are the major components of grey matter. The white matter is populated by axons and glial cells. In other terms, the white matter is the highway through which the information passes to reach their destination, the grey matter.

Both regions have very different energy expenditures that are worth noting. In this section, I will describe how they use the energy and how those energetic needs are matched by the different cell types.

2.1. Energetics of the grey matter

The grey matter is characterized by the presence of neuronal cell bodies and synapses. Ninety percent of cortical neurons are excitatory neurons that release glutamate at the presynaptic terminals. The ratio between excitatory and inhibitory neurons is 9:1 (Attwell and Laughlin, 2001). That is why all the calculations of brain energy in the cortex are done using one excitatory neuron as a model.

Neurons integrate the information received from the environment by producing an action potential that will flow from the soma to the synapse to communicate with other neurons. The action potential is a change in the membrane charge caused by the influx of sodium ions and efflux of potassium ions from the cell (Bean, 2007). When the action potential reaches the presynaptic terminal, there is an influx of calcium into the synapse that induces the release of neurotransmitters into the synaptic cleft (Südhof, 2012) where a post-synaptic neuron will detect it. This process is called neurotransmission. When neurotransmitters (for example glutamate) are released into the synaptic cleft, they bind to post-synaptic receptors and trigger an influx of sodium and/or calcium ions into the post-synaptic neuron (Schiller et al., 1998), starting the process of neurotransmission again.

Neurotransmission, which is mainly a cortical process, is metabolically a very expensive process. The cortex is the most energetically demanding region of the brain. It consumes 27.2 to 40.7 µmol ATP/g/min (Howarth et al., 2012), meanwhile, the entire brain consumes on average 21 µmol ATP/g/min (Attwell and Laughlin, 2001). Calculations predict that, at the awake state, between 15% and 19.9% of the neuronal energy is used to keep the sodium ion homeostasis at rest. To extrude the sodium ions that enter into the cell during the action potential, the neuron uses 8.7% to 16% of its energy. Housekeeping tasks, such as axoplasmic transport, and turnover of macromolecules, account for 10.6% to 25% of the neuronal energy (~ 6.79 µmol ATP/g/min). The remaining 44% to 60.8% is spent at synaptic processes (where 4.3% to 5% is used to release the neurotransmitters, 4% to 8% is used to remove the calcium entry at the pre-synapse, and the rest is used to reverse the sodium and calcium influx at the post-synapse) (Howarth et al., 2012; Yu et al., 2018). This means that the most expensive process is recovering the ionic homeostasis in the post-synapse after neuronal communication is over.

The astrocyte's processes account for 5% to 15% of the grey matter's energy expenditure (Attwell and Laughlin, 2001; J. Magistretti and Allaman, 2016). Nevertheless, they uptake almost half of the glucose of the cortex (Chuquet et al., 2010; Nehlig et al., 2004). It is calculated that 52.9% of the energy of astrocytes is spent on restoring calcium levels inside the cell after neurotransmission. Housekeeping tasks take the second biggest energy consumption with 28%. Lastly, 19.1% is used to keep the sodium ion homeostasis (Yu et al., 2018).

If the ATP production is not perfectly tuned to support neurotransmission, it causes a decrease in neuronal activity (Trevisiol et al., 2017). This can, eventually, lead to synaptic loss and neuronal death (Cardozo et al., 2019). The brain, unlike skeletal muscle or the liver, has minimal energy stores. This implies that the majority of ATP needs to be produced from circulating glucose every time that its used.

2.2. ATP production in grey matter

Glucose levels in the blood are around 3 mM to 6 mM, while, in the brain parenchyma, glucose levels are 20% to 25% lower and reach 0.5 mM to 1 mM (Dienel, 2012; Suh et al., 2007). Although neurons express the glucose transporter GLUT3, and thereby could potentially take up glucose, they express very low levels of the phosphofructokinase-2 enzyme that regulates glycolysis (Almeida et al., 2004). This suggests that neurons would prefer other energetic metabolites like pyruvate or lactate instead of glucose to produce ATP.

Glucose is mainly processed by astrocytes. They are highly glycolytic glial cells (Herrero-mendez et al., 2009) involved in a plethora of molecular, cellular, and immunological processes in the brain. Glucose enters the astrocytes via the GLUT1 transporter, and it is rapidly converted into glucose-6-phosphate in the first step of glycolysis. The end result of glycolysis is the production of two molecules of pyruvate and two molecules of ATP from one molecule of glucose. Astrocytes ensure the maintenance of high reducing equivalents by different mechanisms that are key for keeping these high glycolytic levels. Additionally, they prevent the further metabolic breakdown of pyruvate in the Krebs cycle by having low expression levels of pyruvate dehydrogenase (Laughton et al., 2007), resulting in a high availability of lactate, that can be released from the cell.

Lactate is released via monocarboxylate transporters (MCTs) into the interstitial tissue where other cells, mainly neurons, uptake it and use for further ATP production. Once in the cytoplasm, lactate can be converted back to pyruvate, by the lactate dehydrogenase, and it is then shuttled to the mitochondrial matrix where it enters the Krebs cycle. At the end of the 10 different reactions that constitute the Krebs cycle, there will be a production of one molecule of ATP, three molecules of nicotinamide adenine dinucleotide (NADH), and one molecule of flavin adenine dinucleotide (FADH) for each molecule of pyruvate. Although the Krebs cycle produces only one molecule of ATP, the other electron donors, like NADH, and FADH will give away their electrons into the electron transport chain (last step of the oxidative phosphorylation) in the mitochondrial membrane to release energy in the form of ATP. The electron transport chain will produce 28 molecules of ATP, adding up to the one produced by the Krebs cycle.

By putting together the cell-specific evidence of glycolysis in astrocytes, the oxidative phosphorylation in neurons, and the amount of energy and glucose consumption, the neuro(-glia)metabolic cooperation via a lactate shuttle hypothesis was formed (Pellerin and Magistretti, 1994).

2.3. Neurometabolic coupling in grey matter

The structure of the central nervous system is organized around optimizing neuronal activity. Upon increased neuronal activity, mainly by increasing neuronal communication, glial and vascular cells will increase their metabolism to support neuronal ATP production, in a process called neurometabolic coupling (Leybaert, 2005).

As explained before, during synaptic neurotransmission, glutamate is released into the synaptic cleft. If glutamate is not quickly cleared, the post-synaptic neuron could potentially die of calcium excitotoxicity (Arundine and Tymianski, 2003).

Astrocytes are responsible for the rapid glutamate removal from the synaptic cleft. Astrocytic processes are located around the synapses, and together with the pre and post-synaptic cells, they form the tripartite synapse (Danbolt, 2001). Two glutamate transporters are found in astrocytic process: the glutamate-aspartate transporter (GLAST) and the glutamate transporter type 1 (GLT1). When glutamate enters the astrocyte via these transporters, it is co-transported with three sodium ions and one proton, and at the same time, one potassium ion is extruded from the astrocyte (Barbour et al., 1988). Upon entry into the astrocytic cytoplasm, glutamate is transformed into glutamine. Glutamine molecules are shuttled back into the presynaptic neuron where glutaminases recycle glutamine into glutamate.

These two processes, the transport of glutamate and its conversion to glutamine, are very energetically demanding. Each molecule of glutamate that is converted into glutamine uses one ATP molecule (there are ~8000 glutamate molecules per synaptic vesicle (Wang et al., 2019)), and the sodium-potassium ATPase uses one ATP molecule for each cycle of removing three sodium ions. As a consequence of glutamate uptake, the ATP/ADP ratio of the astrocyte decreases, which results in an increase in glycolysis (Pellerin and Magistretti, 1994).

As mentioned before, the glycolysis in astrocytes will produce mainly pyruvate and lactate, which will be secreted out of the astrocyte via MCTs. Astrocytes express MCT4 and MCT1, which are also highly expressed in endothelial cells. Neurons express MCT2 (Debernardi et al., 2003; Vanlandewijck et al., 2018). As with most molecules, lactate will follow the concentration gradient, meaning that it will go from a zone of high concentration to a zone of low concentration. The 3 MCTs show differences in their affinity for lactate, with MCT2 having the highest affinity (K_m = 0.74 mM) followed by MCT1 (K_m = 3.5 mM) and MCT4 (K_m = 28 mM) (Halestrap, 2012). Practically, this means that cells with MCT2 will start uptaking lactate faster than cells with MCT4/1 (in reality this is more complicated than that since the transport of lactate is also coupled to the $NAD^+/NADH$ ratio. The on-off rates of the transporters can also play a role). Thus, once astrocytes produce lactate, and it is released into the parenchyma, mainly neurons uptake it. Once inside the neuron, as mentioned before, it will be metabolized into pyruvate to feed the Krebs cycle to produce ATP through oxidative phosphorylation.

The data supporting the astrocyte-neuron metabolic coupling comes from *in vitro*, *ex vivo*, and *in vivo* experiments using pharmacology, neurogenetics, and different imaging techniques (Barros et al., 2009; Cholet et al., 2001; Chuquet et al., 2010; Herard et al., 2005; Kasischke et al., 2004; Mächler et al., 2016; Magistretti and Chatton, 2005; Nehlig et al., 2004; Pellerin and Magistretti, 1994; Porras et al., 2004; Rouach et al., 2008; Sotelo-Hitschfeld et al., 2015). Arguments against this model have been presented as well (reviewed in ((Dienel, 2012)).

A different model of astrocyte-neuron metabolic communication proposes that the increase in cytosolic calcium levels, at the synaptic terminal during depolarization, induces the activation of the α-ketoglutarate dehydrogenase enzyme. This eventually leads to an increase in NADH and a decrease in ATP, which will induce glycolysis and lactate synthesis. However, due to the high levels of NADH, lactate cannot be further oxidized until the cell reaches low cytosolic calcium levels and high NAD^+ levels (during repolarization or in between depolarization). At this point, the reaction that metabolizes lactate into pyruvate is favoured. This model suggests that the extracellular lactate that can be converted into pyruvate is only used while the neurons are at rest. During periods of high activity, neurons prefer the fast way of using glucose for glycolysis. New evidence shows that neurons can use glucose for glycolysis (Díaz-García et al., 2021), meaning that glucose is the molecule needed to support neuronal communication (Bak et al., 2009). This has been reviewed extensively (Dienel, 2012; Yellen, 2018).

The previous evidence suggests that it should be a neuron-astrocyte coupling, which has been observed in the retina (Mangia et al., 2009). Photoreceptors use glycolysis as a very fast energy production source and shuttle the lactate so that glial cells use it for oxidative phosphorylation (Kanow et al., 2017). It is also imaginable that there is sub-cellular compartmentalization of glycolysis and oxidative phosphorylation. Neurons have a higher presence of mitochondria in the soma compared to pre and post-synaptic terminals (Seager et al., 2020). Both pre and post-synaptic terminals are places of very high energetic demands (as mentioned before), thus it makes sense that glycolysis (which is a cytosolic process) is performed at these sites and that the oxidative phosphorylation happens in the soma or further away from the synapse (Li et al., 2004; Patel et al., 2014). Although this new evidence shines a light on a broader and more complicated metabolic balance of energy production in neurons, more studies are needed to elucidate the compartmentalization and metabolites used for ATP synthesis.

Figure 1 illustrates a simplified version of the neurometabolic coupling (NMC) of the grey matter. For clarity, some concessions have been made. The shuttle of lactate to the neuron is usually depicted in the pre-synapse, however, according to the calculations, the most energetic region is the post-synapse, thereby the more reasonable destination for the astrocytes to send the lactate is this region. The lactate may be exported to the brain parenchyma, although this is not shown. The entrance of glucose to the synapse via GLUT3, which will produce glycolysis as a fast source of energy during active action potential firing, is depicted as well. Nevertheless, at rest, the metabolic balance should shift, and the Krebs cycle and oxidative phosphorylation are favoured, however, here, this is shown as if it is continuous and does not depend on the firing state of the neuron. In the post-synapse, the activation of glutamatergic receptors will trigger a cascade of signalling molecules which could use GTP molecules as a source of energy. Although they are not shown, the use of GTP is a general process occurring in this sub-cellular structure.

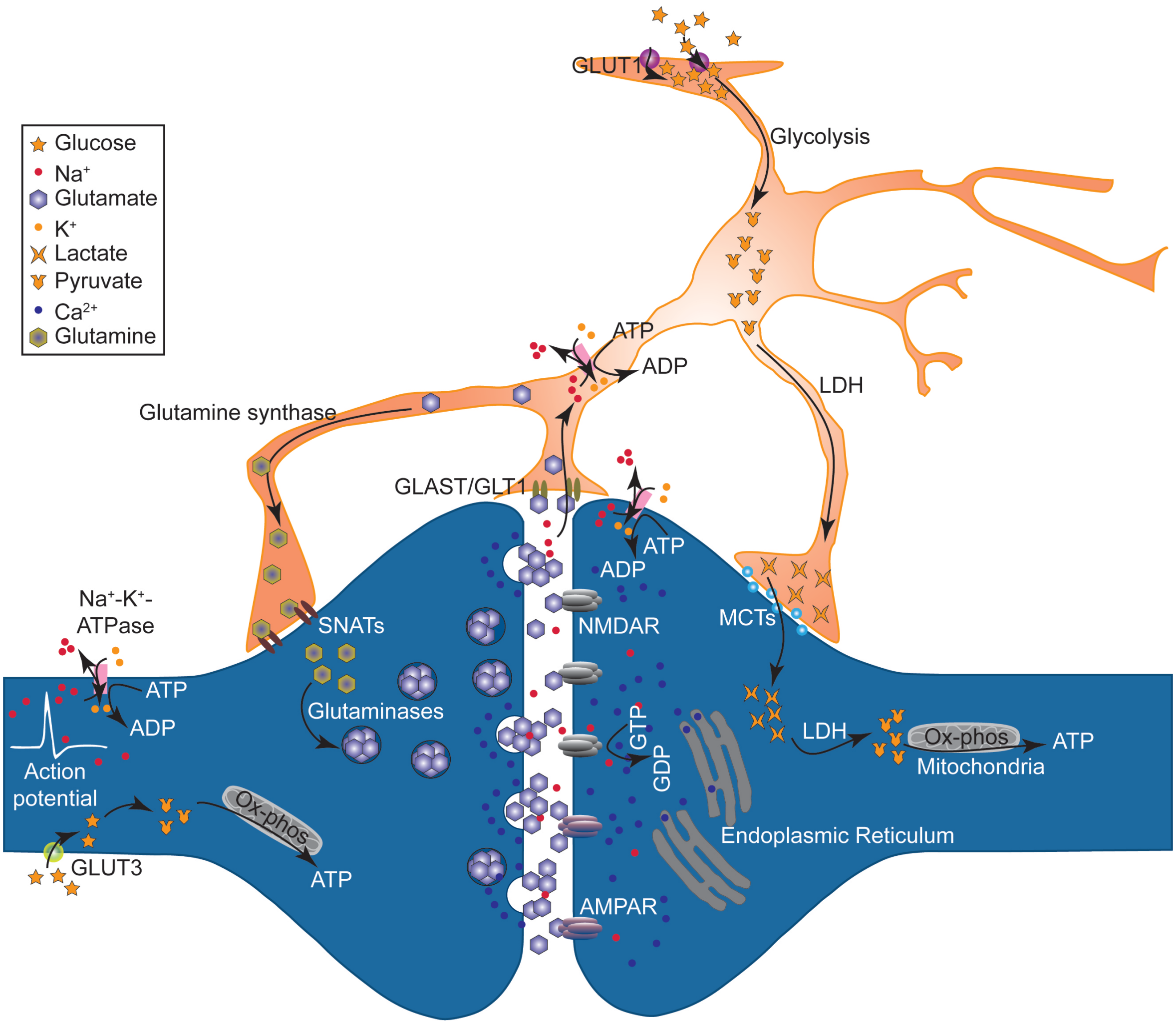

Figure 1: Neurometabolic coupling model of the grey matter. The pre- and post-synapse (blue) during neuronal communication and an astrocyte (orange) are shown forming the tripartite synapse. For a detailed explanation, please refer to the main text.

Despite the different and sometimes contradictory data, it is possible that the use of lactate as fuel is region dependent, that it changes between *in vitro*, *ex vivo,* and *in vivo* conditions, or that it is restricted to certain sub-cellular structures only. Although these hypotheses try to explain the energy consumption in the most active part of the brain (the grey matter), they leave the white matter (which is half of the human brain) outside of their considerations.

2.4. Energetics of the white matter

The above considerations only take the soma or the synapse into account, however, neurons have axons that can have a length of many centimetres. Along those axons, energy is needed to support axonal transport, action potential regeneration, and cytoskeletal organization. The problem arises when those axons are insulated from the brain parenchyma by myelin sheets (produced by oligodendrocytes), and thus, do not have direct access to glucose or lactate.

As mentioned before, the white matter is deprived of synapses, which is where the most energy is spent (2.1 Energetics of the grey matter), thus the energetic requirements are much lower. For example, the auditory cortex uses 162 µmol ATP/100 g/min, in the rat, but the corpus callosum only uses 40 µmol ATP/100 g/min (Clarke and Sokoloff, 1999), which is a decrease of 75.3%. This dramatic difference in energy, thus in glucose utilization, is caused by the insulation capacities of myelin. Myelin is responsible for the saltatory conduction of the action potential (Waxman, 1997). One advantage of this type of conduction over the one from a non-insulated axon, is the reduction in energy needed to propagate the action potential (Nave and Werner, 2014). If in grey matter the energy used for the propagation of the action potential accounts for 8.7% to 16%, in the white matter it accounts for only 0.4% to 1% (Harris and Attwell, 2012; Yu et al., 2018). As there are virtually no synapses in the white matter, the energy used for synaptic communication is around 0.1% of the total white matter energy budget. In contrast, the energy spent in keeping the resting potential of the axons (43.8% to 58%) and the housekeeping tasks (24.3% to 55.7%) make up the majority of the expenditure (Harris and Attwell, 2012; Yu et al., 2018).

It is still debatable if the reduction in energy used for action potential propagation by myelination is worth the energy used by oligodendrocytes to produce myelin (Hirrlinger and Nave, 2014) and maintaining the resting potential of the cell (Harris and Attwell, 2012). Axonal transport is one of the processes that form the housekeeping activities of the white matter neurons, and it is a very expensive one, due to the constant GTP and ATP-dependent process of microtubule polymerization and motor proteins movement. This means that the neuron needs to support ATP production along the entire axon. Failing to do so results in and/or contributes to neurodegenerative disorders such as peripheral neuropathies, amyotrophic lateral sclerosis, and others (Millecamps and Julien, 2013).

With axons almost completely insulated from the brain parenchyma, only leaving the nodes of Ranvier as patches of naked axons with direct contact with the extracellular medium, neurons need to be able to send energetic substrates into the axon. For this, neurons could use oligodendrocytes in the same way as they use astrocytes in grey matter. Oligodendrocytes could metabolically support the wrapped axons at rest or during periods of high axonal activity (Nave, 2010) forming an axo-glia metabolic coupling in the white matter.

2.5. Neurometabolic coupling in white matter

To support axonal trafficking and other housekeeping processes, neurons can mobilize mitochondria along the axon (Harris and Attwell, 2012; Nave and Trapp, 2008). But, as myelin presents a barrier, glucose or lactate can only go into the axon via the nodes of Ranvier. Theoretically, if the axon in the optic nerve is thicker than 1 µm, there is enough glucose entering the node via the GLUT3 transporter to support the oxidative phosphorylation of the axon even during stimulation. In fact, there is an excess of ATP production (Harris and Attwell, 2012). However, the majority of the axons in the optic nerve are thinner than 1 µm (Perge et al., 2009), and according to calculations (Harris and Attwell, 2012), with a diameter thinner than 0.9 µm there will be a deficit of ATP produced by the mitochondria if glucose only enters via the nodes. It is also possible that, if the length in between nodes is larger than the average (240 µm), the amount of glucose entering the nodes is not enough to flow along the axon to support all the mitochondria located at the internodes.

This opens up the possibility of oligodendrocytes shuttling metabolites back to the axon. As in the grey matter, this process needs to be linked to axonal activity, otherwise, there will be a constant flux of metabolites which could increase the acidity of the extracellular medium. Although it is thought that neurotransmitter vesicles are only released at the synapse in a calcium-dependent fashion, axons have very similar machinery for vesicle release along the total length of the axon (Kukley et al., 2007; Micu et al., 2016).

When the action potential flows through the axon, there is a depolarization which is detected by voltage-gated calcium channels located on the axonal membrane. Due to the barrier that the myelin sheath presents, there is no influx of calcium, rather, the voltage-gated calcium channels are coupled to internal calcium stores of the axon, called axoplasmic reticulum, via ryanodine receptors (Ouardouz et al., 2003). This increase in calcium induces neurotransmitter vesicle release, mainly glutamate, into the periaxonal space (Bergles et al., 2000; Kukley et al., 2007; Micu et al., 2016). Similar to grey matter, in white matter glutamate will bind to NMDA or AMPA receptors located in the myelin sheath and will induce an increase in calcium and sodium inside the myelin of the oligodendrocytes (Micu et al., 2007, 2016).

It is hypothesized that this communication will regulate the axo-glia metabolic coupling, just as it does in the grey matter. Upon oligodendroglial NMDA receptor activation, the oligodendrocytes mobilize GLUT1 transporters to the cell membrane within 30 min and increase glucose uptake (Saab et al., 2016). As oligodendrocytes are highly glycolytic cells, they increase lactate production which in turn supports axonal activity (Fünfschilling et al., 2012). Lactate alone has been shown to support axonal activity, suggesting that axons do not need glucose for energy production, instead lactate is used for oxidative phosphorylation and ATP production (Brown et al., 2003). Pyruvate has also been reported to support axonal conduction in the absence of glucose (Brown et al., 2001). These observations have been confirmed by the progressive axonal loss in a mouse model where half of the MCT1 (lactate/ pyruvate transporter) transporters are deleted (Lee et al., 2012). Interestingly, oligodendrocytes do not metabolically support the axons alone. Astrocytes can also take part in this task in the white matter as well. When astrocytes uptake glucose, they can store part of it as glycogen (Bak and Walls, 2018). Glycogen will serve as an energy reserve, which is very rare in the brain. Depending on the glucose levels, glycogen can be used as a source of energy (Rich et al., 2019). Glycogen can be metabolized into lactate and support axonal conduction even during ischemic conditions (Brown et al., 2004, 2005; Saab et al., 2016; Tekkök et al., 2005; Trevisiol et al., 2017).

The presence of gap junctions between oligodendrocytes and astrocytes (Xia et al., 2020), MCT1 expression in oligodendrocytes (Lee et al., 2012; Vanlandewijck et al., 2018), MCT1/4 expression in astrocytes (Debernardi et al., 2003; Vanlandewijck et al., 2018), and the fact that astrocytes have restricted contact with axons in the white matter (only at the nodes of Ranvier) (Köhler et al., 2019), suggests that oligodendrocytes, rather than astrocytes, preferentially support the metabolic needs of the axon. Although the model for axo-glia metabolic coupling has only been suggested recently, it is conceivable that astrocytes produce lactate upon axonal stimulation by sensing the increase in extracellular potassium (Brown et al., 2003). That lactate will be secreted and picked up by oligodendrocytes. At the same time, oligodendrocytes sense axonal activity via NMDA receptors and increase their glycolytic metabolism. Lactate or pyruvate is then shuttled back to the axon to support oxidative phosphorylation (Micu et al., 2018).

The previous model for NMC has been almost exclusively investigated in the optic nerve. One key difference between this white matter tract and other white matter regions like the corpus callosum is the virtual absence of unmyelinated axons in the optic nerve (Honjin et al., 1977) compared with the high number of unmyelinated axons in the corpus callosum (Sturrock, 1980). Recent experiments show that the NMC mechanism can vary depending on the brain region (Meyer et al., 2018; Philippot et al., 2021). Compared with the optic nerve, in the corpus callosum, lactate alone cannot support axonal activity (Brown et al., 2003, 2005; Meyer et al., 2018). However, when oligodendrocytes, rather than astrocytes, are filled with glucose, the axonal activity can be maintained after removing the glucose from the extracellular media. The axonal support was completely abolished by simultaneously blocking the entrance of glucose into oligodendrocytes via GLUT1 and by inhibiting MCT1/2 transporters and GLUT3 (individual inhibition for GLUT1 or MCT1/2, did not abolish axonal activity), suggesting that oligodendrocytes support the axonal metabolism by supplying the axon with glucose rather than lactate (Meyer et al., 2018). These data indicate that astrocytes are not involved in the axonal support in the corpus callosum. On the contrary, astrocytes seem essential in the thalamus. In the thalamus, when the continuum between oligodendrocytes and astrocytes (otherwise called panglial syncytium) is inhibited, synaptic activity is also inhibited, even if both cell types are filled with glucose or lactate. This indicates that both cell types are necessary for NMC. Additional evidence shows that oligodendrocytes, rather than supporting axonal activity, support astrocytes in shuttling lactate or pyruvate into the post-synaptic neuron (Philippot et al., 2021).

To illustrate the NMC of the white matter, I used the example of the optic nerve. Figure 2 shows the summary of the current model. It also shows the entrance of glucose via GLUT3 at the nodes of Ranvier that could support, theoretically, the energetic needs depending on the axon size. The use of ATP by the sodium-potassium pump is shown. It is worth considering that the ATP/ADP ratio may change the metabolic route used by the axon to produce energy.

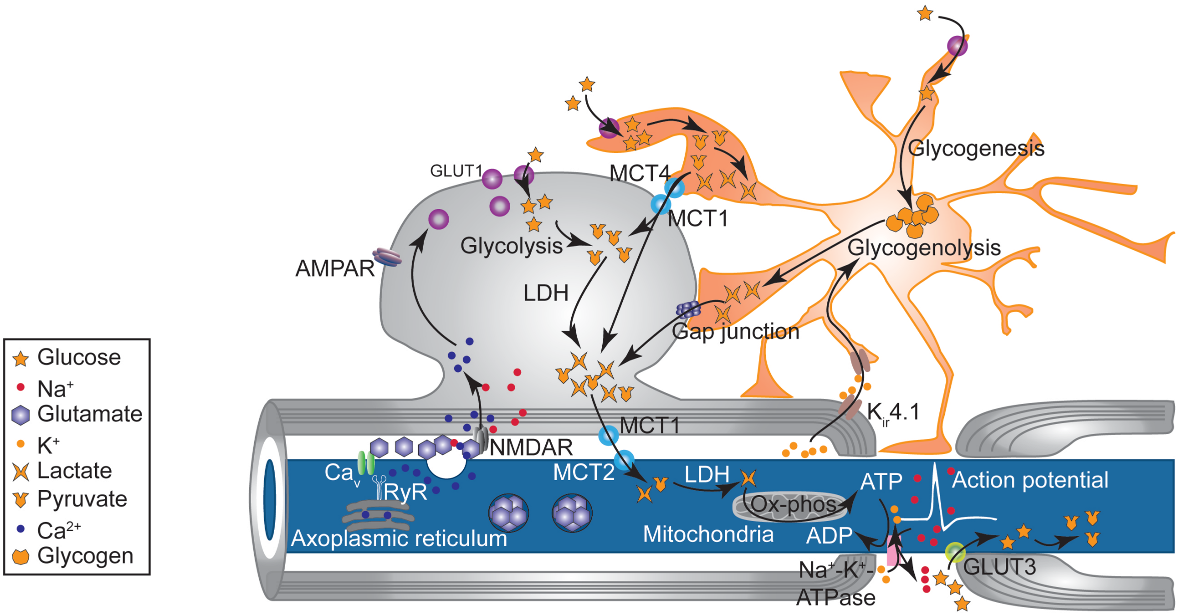

Figure 2: Neurometabolic coupling model of the white matter using the optic nerve as a model tissue. Axon (blue) during action potential firing and an astrocyte (orange) are shown. For a detailed explanation, please refer to the main text.

Since the NMC in white matter was postulated in 2010, the model is not as developed as the one for grey matter, which was postulated in 1994. Nevertheless, both models have glial lactate/pyruvate as a central player in metabolic support of neuronal activities. However, the NMC, taken as astrocytes/oligodendrocytes increase glycolysis upon synaptic/axonal activity, requires that the vascular system also increases the availability of glucose and oxygen in the region of increased activity.

3. NEUROVASCULAR COUPLING IN GREY MATTER

For NMC between neurons/axons and glial cells to work timely, there must be a precise and well-tuned delivery of metabolites in time and space. The vascular system is responsible for delivering these metabolites. Upon increased neuronal activity, the increased delivery is achieved by dilating the blood vessels, thus increasing the blood flow. The coupling between increased neuronal activity and increased vessel dilation is called neurovascular coupling (NVC), or functional hyperaemia (Leybaert, 2005). The metabolites, under healthy conditions, are almost exclusively glucose and oxygen, although the CNS can potentially use cholesterol or ketone bodies to support neuronal functions (Stumpf et al., 2019), even though under normal conditions they will not cross the blood-brain-barrier (Berghoff et al., 2022).

The vascular system is a network of tubes with different diameters transporting a liquid with very special characteristics, the blood. Depending on the size of the vessel, some characteristics change. A good example of this is that the oxygen extraction from the blood only happens at capillaries and not at arterioles or arteries. Due to changes in the partial pressure of oxygen (pO_2) in capillaries created by erythrocyte-associated transients, the oxygen diffusion takes place and thus feeds the surrounding tissue (Lücker et al., 2015;

Parpaleix et al., 2013). The conditions in larger vessels prevent the drops in pO_2 seen in capillaries. Glucose depends on transporters that are localized at the luminal and abluminal sides of endothelial cells along the entire vasculature to enter the brain (Leybaert et al., 2007). The amount of transporters correlates with the amount of glucose metabolized in the brain (Zeller et al., 1997). As oxygen is necessary for oxidative phosphorylation, which is mainly performed by neurons, it is key that all neurons have sufficient access to the oxygen delivered from capillaries.

In the cortex of a mouse, on average, a capillary will be 12 µm away from any other cell (Ji et al., 2021; Tsai et al., 2009). This means that the soma of a neuron is, on average, 12 µm away from a capillary. In the corpus callosum, the distance increases to almost 20 µm (Ji et al., 2021). As the cortex has a high capillary density, oxygen availability might not be a problem in normal physiological states. In other brain regions, other cellular adaptations have been suggested to be in place to function under certain levels of hypoxia (Shaw et al., 2021; Wakhloo et al., 2020).

The transport of glucose into the brain can be upregulated by two processes. One is to increase the difference between interstitial glucose concentration and periphery, and the second is to modify the physical properties of the transporters, for example by glycosylation (Leybaert et al., 2007). Oxygen diffusion into the brain can only be increased by the increased gradient between interstitial tissue and the blood. To increase the availability of both molecules, vessels need to dilate and cerebral blood flow (CBF) to increase. If NMC induces the increase in glucose and oxygen consumption, and NVC dilates vessels to support it, it is possible that the vessel dilation (increases glucose availability) and increase in CBF (increases oxygen diffusion) happen at different parts of the vascular tree.

Neurovascular coupling studies have been, almost exclusively, done in the grey matter. For *in vivo* studies the somatosensory cortex is the most studied region. For *ex vivo* studies, layers 4-5 of the neocortex are commonly used. The following section will describe mainly cortical grey matter vasculature.

3.1. Cortical vasculature

Pial arteries run on the surface of the brain and dive perpendicular to feed the cortex in many different places. These vessels receive the name of penetrating arterioles. Not all penetrating arterioles have the same length, meaning that not all of them will feed the same brain regions. For example, some arterioles will only penetrate to layer 1 or layer 2 of the cortex. The most numerous ones will reach as deep as layer 3 of the cortex. The different branching will end up forming the great capillary network of the cortex (Duvernoy et al., 1981).

Typically, the vascular tree (from arteries to veins) can be organized into 5 parts. Penetrating arterioles divide into pre-capillary arterioles, which in turn branch and form the capillaries. From capillaries, when the vessel size increases, the vessels are called post-capillary venules. From there, ascending venules reach the pial surface (Berthiaume et al., 2018). The inner layer of all vessels is composed of endothelial cells. In penetrating arterioles, the endothelial cells are covered by one layer of vascular smooth muscle cells, which together with the endothelial cells are embedded in the basement membrane. At the pre-capillary arteriole level, there are no vascular smooth muscle cells but rather other perivascular cells that retain contractile properties called ensheathing pericytes. In capillaries, the perivascular cells are called thin-stranded pericytes and have been shown not to express α smooth muscle actin (Grant et al., 2019). Venules and ascending venules are covered by perivascular cells that do not have contractile properties, even if sometimes they are referenced as venule smooth muscle cells (Berthiaume et al., 2018). All the vessels are covered by astrocytic end-feet (Schaeffer and Iadecola, 2021). The perivascular cells that cover the pre-capillary arterioles, capillaries, and post-capillary venules, have sparked a controversy about their name and their contractile properties.

The term pericyte was used for the first time in 1923 by K. W. Zimmermann. In his description, pericytes are peri-endothelial cells with an ovoid cell body forming a "bump-on a log" morphology that are on top of the vessels between arterioles and veins (Zimmermann, 1923). Pericytes have been shown to participate in basement membrane formation (Hallmann et al., 2005; Stratman and Davis, 2012), transcytosis across the blood-brain-barrier and vascular permeability (Armulik et al., 2010; Daneman et al., 2010; Siegenthaler et al., 2013), astrocytic end-feet polarization (Armulik et al., 2010), vascular morphogenesis (Betsholtz et al., 2005), formation of brain calcifications (Betsholtz and Keller, 2014), and blood flow regulation (Hartmann et al., 2021).

The problem with pericyte research, and more specifically their role in blood flow regulation, is that there are no specific or unique pericyte markers and there is no consensus on the definition of these cells. A common tool to study pericyte biology are the reporter lines such as the Platelet Derived Growth Factor Receptor Beta *(Pdgfrβ)* Pdgfrβ-tdtomato or the Chondroitin Sulfate Proteoglycan 4 (*Cspg4*) NG2-dsRed (Hartmann et al., 2015). Although both transgenic mice lines allow for direct observation of pericytes, they are not specific for them. All perivascular cells, including smooth muscle cells and venule smooth muscle cells, express *Pdgfrβ* and *Cspg4*. Oligodendrocyte precursors cells, which can be located in a perivascular position, just like pericytes, also express the *Cspg4* gene (Tsai et al., 2016). It is then necessary to perform a morphological study of the perivascular cell and the vessel to know where in the vascular tree the measurements are done.

The morphology of capillary pericytes has led to believe that they do not have the properties to induce vessel constriction or dilation, and thus cannot regulate blood flow. This hypothesis was corroborated by using a reporter mouse that expresses mCherry under the control of the promoter of α smooth muscle actin (SMA-mCherry). The expression pattern in these mice, both *in vivo* and in brain slices using immunohistochemistry, shows that actin is only expressed in arterioles and the next branch of the vascular tree, which corresponds to the pre-capillary arteriole (Hill et al., 2015). Single-cell RNA sequencing has also shown that there is a very low number of transcripts in pericytes (Vanlandewijck et al., 2018). However, a recent investigation found that the detection of α smooth muscle actin in brain slices is dependent on the fixation method of the tissue (Alarcon-Martinez et al., 2018). Because only the cells in the pre-capillary arteriole have the mechanism to induce constriction, the investigators claimed that blood flow is not controlled by pericytes but rather by pre-capillary smooth muscle cells (Hill et al., 2015) contradicting other data that shows that pericytes are the ones regulating blood flow (Hall et al., 2014; Mishra et al., 2016).

After a closer morphological and functional examination, the group of Andy Shih proposed that what Hill *et al.* call pre-capillary smooth muscle cells (Hill et al., 2015) is the same as what Hall and Mishra *et al.* call pericytes (Hall et al., 2014; Mishra et al., 2016). Shih's group proposes that those cells at the pre-capillary arteriole, that are positive for α smooth muscle actin and have pericyte morphology, should be called ensheathing pericytes. The pericytes at the capillary level receive the name of thin-stranded pericytes and the perivascular cells on the venules and between pre-capillary arterioles and capillaries receive the name of mesh pericytes (Berthiaume et al., 2018; Grant et al., 2019; Hartmann et al., 2015, 2021).

3.2. Neurovascular coupling history

The first studies indicating a change in CBF upon stimulus were done by Mosso and Roy, and Sherrington in the late 1880-1890s. Upon simulated brain metabolic activity or actual brain stimulation, they observed an increase in the volume of the brain. They attributed this to an increase in blood flow in the brain (Iadecola, 2017). It was only 70 years later that the first technique to quantitatively measure changes in CBF was developed by Seymour Kety and Lou Sokoloff. By developing autoradiographic techniques, they could show that there is an increase in regional CBF that is restricted to the activated brain area (Iadecola, 2017). This opened the door to new methods to study CBF and gave mankind one of the most used techniques to diagnose cerebral diseases, the blood-dependent oxygenation levels (BOLD) effect measured by functional Magnetic Resonance Imaging (fMRI).

The fMRI measures the changes in oxygenation in the blood, otherwise called the BOLD effect, which results from brain activity. In a seminal paper in 2001, Logothetis showed that the increase in regional blood flow was induced by local field potentials, meaning that synaptic activity was the cause of the increase in regional oxygenation (Logothetis et al., 2001). Although fMRI has become a routine technique to diagnose brain diseases by studying brain activity, the actual cellular basis of increased regional oxygenation upon synaptic activity is not fully elucidated.

Neurovascular research is a young field of study. This implies that there are many contradicting or opposing papers that try to elucidate the NVC mechanism. In this section I set out to review some of the proposed mechanisms from both *in vivo* and *ex vivo* data.

3.3. Neurovascular coupling mechanism

3.3.1. Neurons

Neurons are the originators of the NVC signalling mechanism. Whether it is via a direct or indirect mechanism remains to be studied. No disturbance of a single receptor or enzyme by inhibition or genetic ablation has eliminated 100% of the NVC response. The largest reduction of NVC has been reached by blocking the function of the neuronal nitric oxide synthase (nNOS) (Hosford and Gourine, 2019). nNOS is linked to NMDA receptors located at the post-synapse of neurons (Garthwaite and Boulton, 1995; Olthof et al., 2018). Upon NMDA activation, the calcium influx activates the nNOS and NO is produced (Courtney et al., 2014; Mullershausen et al., 2006). As NO is a gas, it can easily permeate through cell membranes. Upon being liberated, NO will bind to its receptor, the soluble guanylyl cyclase, to activate cyclic GMP and produce a relaxation of the smooth muscle cells that will induce an increase in vessel diameter and blood flow (Roy and Garthwaite, 2006). Additionally, neurons from the basal forebrain can induce dilation via acetylcholine (ACh) release, while norepinephrine secreting neurons from the locus coeruleus induce a large-scale vasoconstriction (Hamel, 2006). Interneurons secrete vasoactive substances that can induce dilation or constriction, such as neuropeptide Y and NO (Cauli, 2004). As there is great heterogeneity in the regional population of interneurons and neurons, the control of CBF can be accomplished by different mechanisms depending on the studied region. It is believed that interneurons have a fine-tuning role in the NVC response rather than being mediators (Attwell and Iadecola, 2002; Cauli and Hamel, 2010).

3.3.2. *Endothelial cells*

During neuronal communication, neurons extrude potassium ions (K^+) outside of the cell during the repolarization phase of the action potential (Bean, 2007). The increase in extracellular K^+ can induce vessel dilation either directly or after being uptaken by astrocytes. Interestingly, if the concentration is too high, it can cause vasoconstriction instead. The K^+ threshold seems to be 20 mM. Above 20 mM, K^+ causes vasoconstriction but below that level, it will induce a potent vasodilation (Horiuchi et al., 2002; Knot et al., 1996). Extracellular K^+ activates K_{ir} channels located in the membrane of capillary endothelial cells and smooth muscle cells and induces a cellular hyperpolarization (Longden and Nelson, 2015). As endothelial cells and smooth muscle cells are connected via gap junctions forming a syncytium (Christ et al., 1996), the hyperpolarization can spread along the cells even if it originates in only one cell. It has been proposed that capillary endothelial cells, which differ from arteriolar endothelial cells in their potassium channel signature (Longden et al., 2017), sense the increased K^+ concentration produced by increased neuronal activity via $K_{ir}2.1$ channels. Once the channels are open the hyperpolarization of the endothelial cell travels upstream to induce hyperpolarization of the smooth muscle cells located in the pre-capillary arteriole. When smooth muscle cells are hyperpolarized, voltage-gated calcium channels close and the influx of calcium stops, inducing relaxation of the cell (Webb, 2003). This translates into dilation of the penetrating arteriole and increasing CBF in capillaries (Longden et al., 2017).

3.3.3. *Astrocytes*

Neuronal K^+ is not the only source of K^+ that can induce vessel dilation. Upon neuronal activity, astrocytes increase their intracellular calcium (Ca^{2+}) concentrations which in turn causes the BK channels, located at the end-feet of astrocytes, to open. A large amount of K^+ flows outside of the astrocyte (Filosa et al., 2006; Longden and Nelson, 2015) and induces vessel dilation following the above-mentioned mechanism.

The first study showing that astrocytes are involved in NVC was done in brain slices nineteen years ago. The experiments show that glutamate being released into the synaptic cleft activates metabotropic receptors (mGluR5) in astrocytes, inducing an increase in concentration in intracellular Ca^{2+}. The Ca^{2+} increase activates the cyclooxygenases (COX) enzymes and, via prostaglandins, induces arteriolar dilation (Zonta et al., 2003). Although evidence suggests that mGluR5 is not expressed in mature astrocytes, there is more evidence suggesting that an increase in intracellular astrocytic Ca^{2+} concentrations induces activation of COX1 enzyme that will end up producing prostaglandin E_2 (PGE_2) that will activate the EP_4 receptor in ensheathing pericytes and induce vessel dilation (Hall et al., 2014; Mishra et al., 2016). In this case, the increase in astrocytic Ca^{2+} is mediated by the P2X1 ATP receptor (Mishra et al., 2016). ATP is concentrated into synaptic vesicles (Sawada et al., 2008) and it is released by the same mechanisms as glutamate or any other neurotransmitter (Fields, 2011).

PGE_2 not only activates EP_4 receptors but also other prostaglandin receptors that are part of the G-coupled protein receptor family. In particular, the EP1 receptor, which can mediate constriction if present in perivascular cells, can also mediate vessel dilation when present in capillary endothelial cells. Upon activation, the EP1 receptor mobilizes G_q proteins that activate phospholipase C to hydrolyze PIP_2. When PIP_2 levels decrease, the TRPV4 opens allowing Ca^{2+} influx into the endothelial cell (Harraz et al., 2018). The increase in Ca^{2+} activates the endothelial nitric oxide synthase (eNOS) and thus NO is released. This relaxes adjacent ensheathing pericytes and produces a local dilation (Longden et al., 2021).

Other mechanisms suggest that upon Ca^{2+} increase in astrocytes, glutamate, D-serine, ATP and even lactate can be released from the cell. All of them can directly modulate the NVC response (Kur and Newman, 2014; Lemaistre et al., 2012; Stobart et al., 2013), except lactate, which is not a vasoactive substance *per se*. Once PGE_2 is secreted, astrocytes can reuptake it via a lactate/PGE_2 transporter (Chan et al., 2002). When astrocytes increase glycolysis (2.3 Neurometabolic coupling in grey matter) and lactate is released, the high lactate concentrations inhibit the PGE_2 clearance by the astrocyte (Gordon et al., 2008), thus leaving the PGE_2 to act on either EP_4 receptor located in ensheathing pericytes (Mishra et al., 2016) or on EP1 receptor located in capillary endothelial cells (Longden et al., 2021) to produce vessel dilation.

These mechanisms have in common that the Ca^{2+} increase precedes the vessel dilation. Although there is some contradictory evidence (Nizar et al., 2013; Schulz et al., 2012), the differences may be due to different regions and/or techniques used. For example, the Ca^{2+} events in the end-feet are independent of the ones happening in the soma (Shigetomi et al., 2010). Not only does the time-scale of the end-feet Ca^{2+} events fit the time-scale of vessel dilation (Lind et al., 2013; Otsu et al., 2015), while the somatic ones do not, the release mechanisms are also different. In the end-feet, Ca^{2+} transients are independent of PIP_2, meanwhile, at the soma, they seem to be PIP_2 dependent (Bonder and McCarthy, 2014; Kanemaru et al., 2014; Srinivasan et al., 2015).

NVC regulation seems to be a complex and dynamic process that depends on the coordination of different signalling molecules in different subcellular structures and different cellular populations. It is a system that involves various cells from the vascular system plus the majority of cells of the central nervous system. In Figure 3, I present some of the proposed mechanisms for NVC using a typical glutamatergic synapse of the cortex. To put NVC in context with NMC, both processes are shown. Although it is proposed that the NVC mechanisms differ depending on the location in the vascular tree, the contractile cells are represented by a typical ensheathing pericyte. As shown here, NVC is not a lonely and secluded process, and it should be studied considering the hypothesis of NMC and synaptic communication.

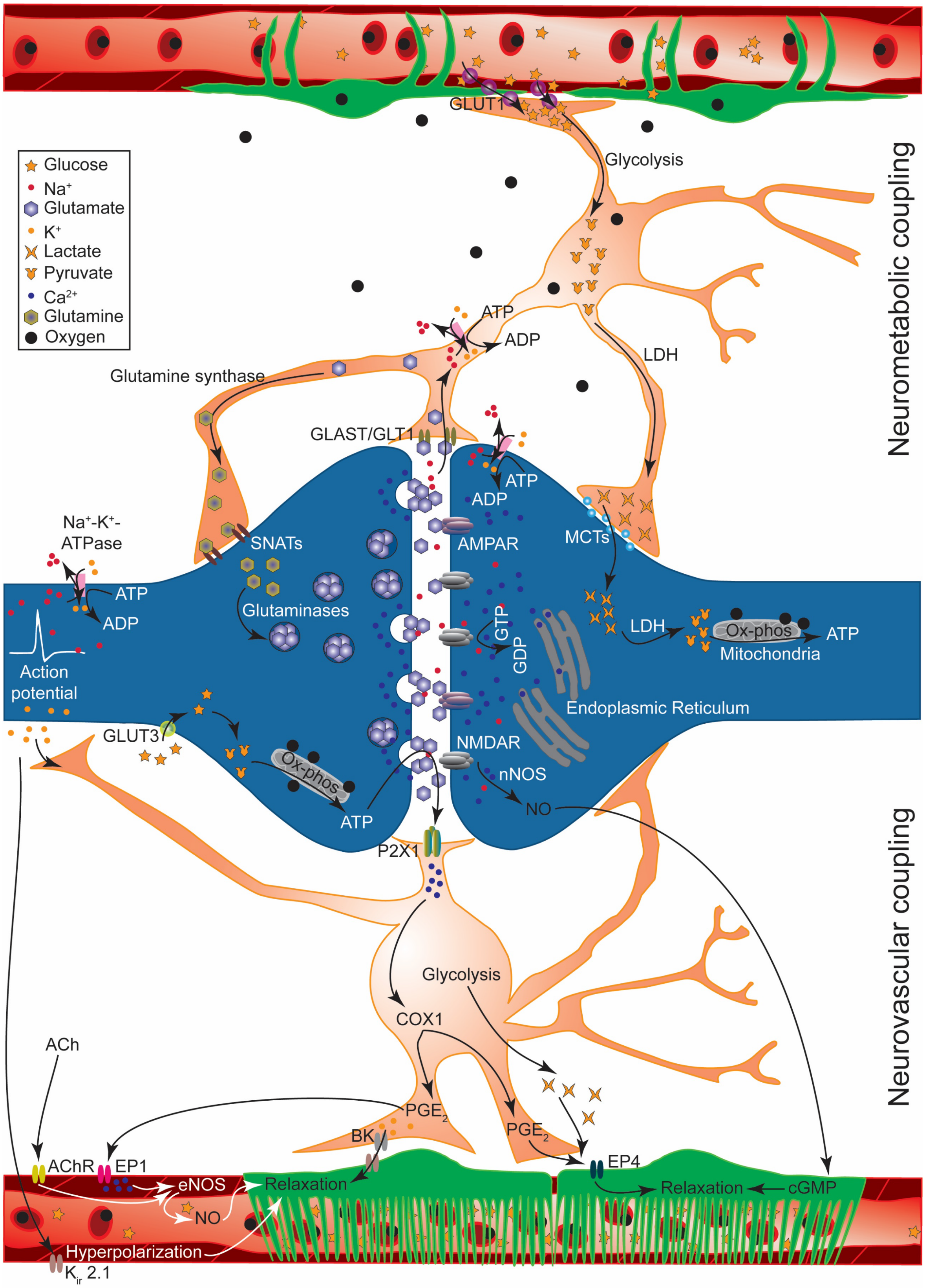

Figure 3: Neurovascular coupling model of the grey matter. The pre- and post-synapse (blue) during neuronal communication and two astrocytes (orange) are shown forming the tripartite synapse. Contractile cells (green) represent either smooth muscle cells or ensheathing pericytes. For a detailed explanation, please refer to the main text. This figure complements the neurometabolic coupling mechanisms discussed before (top part of the figure). The morphology of the pericytes between the top and bottom of the figure is intended to show that the exchange of oxygen and

glucose (NMC) happens at capillaries meanwhile the NVC is possible starting in a more upstream segment of the vascular tree, note how the hyperpolarization of endothelial cells starts in a zone not covered by ensheathing pericytes.

3.4. Why do we have neurovascular coupling?

NVC is the basis for the functional imaging used in clinics for diagnosis of mental disorders. It is thus very important to understand the mechanisms behind it, especially because fMRI does not give direct evidence of neuronal function. Although neurons can fire and function for almost 30 min using glycogen reserves as their sole energetic source (Brown and Ransom, 2007), there is a decrease in both glucose and oxygen concentration that precedes the peak in CBF (Lecoq et al., 2011; Wei et al., 2016), 3-5 secs after the onset of neuronal activity (Hillman, 2014). The initial oxygen dip in the tissue corresponds to the first part of the BOLD signal measured with fMRI. The BOLD signal has an initial undershoot in the first second (Ances et al., 2001; Devor et al., 2008; Parpaleix et al., 2013) followed by an overshoot that starts ~2 secs after the onset of neuronal activity and peaks after 4-6 secs with a maximal increase of ~2%. The BOLD effects finish with a post-stimulus undershoot that has a variable time-course.

The overshoot corresponds to an uncoupling of flow and oxidative metabolism during neuronal activation. This happens because the increase in blood flow is higher than the increase in oxygen metabolism, thus there is an increase in local oxygenation that can be measured by the fMRI (Fox et al., 1988; Ogawa et al., 1990). The excessive amount of oxygen, which is exceeding the tissue demands (Lecoq et al., 2009; Parpaleix et al., 2013), is necessary to maintain normal oxygen levels in regions away from the local stimulation (Devor et al., 2011). Interestingly, the glucose metabolic rate closely follows the increase in CBF (Fox et al., 1988), suggesting that NVC is preferentially used to increase the supply of oxygen to the tissue rather than glucose. Although there are researchers that believe that the opposite is the case (Fox et al., 1988; Heeger and Ress, 2002).

Nevertheless, when animals were kept in hyperoxic (increased oxygenation) or hyperglycaemic (increased blood glucose) conditions, they show a normal CBF and vessel dilation (Lindauer et al., 2010; Wolf et al., 1997). Furthermore, when humans are subjected to hypoglycaemic conditions, NVC still occurs in the same fashion (Powers et al., 1996), suggesting that NVC is not just a process to support the neurons during activation and restore the used energy but, instead, it may be a way that the brain has to keep energy resources for the following stimulations. There is still no consensus on why NVC is essential, but there is evidence that its disruption leads to neurological diseases or, as a secondary hit, it contributes to the pathology observed in neurodegenerative diseases (Iadecola, 2013; Kisler et al., 2017, 2020; Montagne et al., 2018).

3.5. Methods to study NVC

All the previous data for NVC has been collected by building on in two different approaches, *ex vivo* or *in vivo*. Unfortunately, there is no perfect technique and both options have caveats that should be considered.

In *ex vivo* experiments, active brain slices are used. They are obtained by removing the brain of the animal, typically mice, and sectioning the brain to make brain slices. The slices can be kept alive in a solution that mimics the cerebrospinal fluid and with constant oxygenation for around 4 hours (Grutzendler and Nedergaard, 2019). By putting one slice under a microscope, it is possible to find blood vessels and evaluate the position in the vascular tree based on the morphology of the perivascular cell. Although the surface of the slice will contain dead cells, a few micrometres below the surface it is possible to find viable neurons, astrocytes, and blood vessels. To study NVC, neuronal stimulation is done by patching neurons and inducing action potentials or by stimulating the neurons pharmacologically.

This approach has proven itself useful to identify molecular pathways that lead to vessel dilation. However, the many caveats of this technique require that any finding is verified *in vivo*.

The vessel tone is one of the determinants of blood flow resistance through the vessels and it is regulated by basal secretion of vasoactive substances like NO, prostacyclin, endothelin-1, and thromboxane. In the *ex vivo* preparation, the vascular tone is lost, causing vessels to remain collapsed or fully dilated (Mishra et al., 2014), potentially leading to false results about NVC signalling. Another caveat of the *ex vivo* preparation is that glucose and oxygen are coming from outside of the tissue, thus eliminating the main function of the vasculature. The source of glucose and oxygen also creates an unregulated and steep gradient between the intracellular concentration of glucose and oxygen and the bathing solution. Moreover, that gradient will not be the same in all the tissue, as the deeper layers of the slice will receive less glucose and oxygen. The amount of oxygen used has been shown to modify NVC pathways. For example, when experiments are done at 95% oxygenation (the classical concentration used for electrophysiological studies), PGE_2-mediated NVC is not active, contrary to when 20% oxygen is used (Gordon et al., 2008; Hall et al., 2014). In fact, by using 20% oxygenation in the bath, the cells beneath the surface will experience a near-physiological pO_2 (Gordon et al., 2008). In the retina, oxygen has also been shown to modulates the NVC response (Mishra et al., 2011).

It has been suggested that during the preparation of the tissue, several different vasoactive compounds are released which can induce both vasoconstriction or dilation in an unpredictable time-dependent manner (Grutzendler and Nedergaard, 2019). Although the slices can be kept alive for almost 4 hours, reactive gliosis occurs during the first 1.5 hours (Takano et al., 2014), which is normally the time used for the experiment. As explained before, the function of astrocytes is critical for NVC, thus if astrocytes are retracting their processes, NVC can be altered.

Despite the pitfalls of the *ex vivo* approach, it allows for a very straight forward manipulation of experimental conditions such as oxygenation, glucose concentration, pharmacological approaches, and electrophysiological stimulations which are impossible in the *in vivo* approach.

The *in vivo* technique relies on creating a cranial window in the skull of mice to observe the vasculature usually at the single vessel level to study the effect of sensory stimulation in NVC. Even though this approach is more physiological, it is limited to only certain parts of the brain. The majority, if not all, experiments are done in the somatosensory cortex, which is highly organized, and the activated areas are easily identifiable. However, there are reasons to believe that the mechanisms in the barrel cortex differ to the ones in other brain regions (Shaw et al., 2021). Two-photon microscopy offers a deeper range of imaging depths than confocal or epifluorescence microscopes used for *ex vivo* studies, and more than doppler OCT or laser speckle methods are able to achieve *in vivo* (Shih et al., 2012). Yet, the maximal resolution of the two-photon microscope should be considered, since it will most probably not be able to resolve changes in capillary dilation (50-150 nm change from baseline), creating a false conclusion that capillaries cannot dilate (Grutzendler and Nedergaard, 2019).

The cranial window used can either be closed with a coverslip or it can be open, exposing the brain to room temperature and atmospheric oxygen pressure, thus changing NVC responses. Ideally, the cranial window is sealed with a coverslip and the objective of the microscope is heated to a physiological temperature (Roche et al., 2019). Another technical aspect of the technique that increases the difficulty in interpreting the results is the use of anaesthesia. The use of anaesthesia changes brain connectivity (Xie et al., 2019) and thus can impair NVC (van Alst et al., 2019; Chen et al., 2021), and the fact that some types of anaesthesia are not entirely well described, the results of those studies can be very unreliable.

Nevertheless, an *in vivo* approach is a great tool to study hemodynamic responses in physiological conditions as well as the metabolic states of the cells around the desired vessels (Kisler et al., 2018), making it the perfect tool to study NVC and NMC.

All microscopy techniques are very invasive and cannot be used in patients, leaving only the fMRI available to study changes in brain oxygenation, which are then extrapolated into neuronal activity and vessel hemodynamic. The advantage of fMRI is that the entire brain can be imaged at the same time, there is no need for anaesthesia, and brain activity can be induced with certain tasks. Unfortunately, and due to the nature of the NVC and the BOLD effect, the white matter of the brain is always excluded from analysis in experiments using fMRI.

4. NEUROVASCULAR COUPLING IN WHITE MATTER

NVC in white matter is an almost non-existent topic. In the following section I will present why this is the case, and some evidence suggesting that white matter BOLD analysis does not follow the same rules as for the grey matter.

4.1. White matter vasculature

The corpus callosum is the largest white matter structure of the human brain. It connects the 200-300 million axonal projections between the left and right hemispheres across the longitudinal fissure (Luders et al., 2010). In humans, the vascular supply of the corpus callosum comes mainly from the medullary artery which originates from pial arteries. This artery runs perpendicular to the pial surface, through the cortex without branching, thus without supplying the cortical areas. When it arrives at the corpus callosum it turns almost 90 degrees and runs parallel to the corpus callosum (Duvernoy et al., 1981; Li et al., 2019b). Even though the venous density of the white matter is half that of the grey matter, the size of the veins is nevertheless the same (Gawryluk et al., 2014). Some evidence shows that the white matter is mainly vascularized by veins (Kirst et al., 2020), suggesting that the function of the vessels in this area is mainly to collect by-products of brain metabolism.

In both humans and mice, the white matter is vastly less vascularized compared to grey matter. In mice, the corpus callosum has a length density three times lower than the grey matter, but the vessels are longer and less tortuous (Ji et al., 2021). The lower vessel density also reflects the almost 30% difference in CBF in the corpus callosum of 48 weeks old mice (Gawryluk et al., 2014; Montagne et al., 2018).

To my knowledge, there are no studies showing NVC in white matter, neither in humans nor in mice. There are, however, a handful of studies measuring capillary CBF in the corpus callosum of mice (Li et al., 2019a). The reason for this is the technical difficulties that exist due to the nature of the tissue. A normal two-photon microscope using a green dye, like FITC to image blood vessels, has an imaging depth of 400-500 µm. The corpus callosum in mice is located at 1000 µm from the surface. If a red-shifted dye is used, like AlexaFluor 680, the imaging depth can be pushed to 900-1100 µm, which would be enough to image the corpus callosum (Tischbirek et al., 2017). Still, the signal-to-noise ratio is insufficient to reliably map the red blood cell (RBC) speed at capillaries in the corpus callosum (Li et al., 2019a). By improving the detectors of the microscope, it is possible to get a better signal improving the quality of the data. Corpus callosum measurements reveal that the white matter has the same haematocrit counts (percentage of RBC) but has a faster RBC flux compared to grey matter, meaning that the time that RBC spends in capillaries is lower (Li et al., 2019a). This has consequences on the amount of oxygen that can be extracted, which is lower in white matter compared to grey matter (Leenders et al., 1990). The same study showed that white matter has a lower capacity to adapt to global CBF perturbations like hypercapnia or hypoperfusion, probably due to the position of the tissue with respect to the vasculature. As there are not many arterioles that regulate changes in blood pressure to support CBF upon systemic challenges, the white matter is more at risk compared to grey matter, probably explaining why there is more white matter deterioration under conditions of global hypoperfusion (Li et al., 2019a), like in Alzheimer’s disease (Iadecola, 2013).

4.2. Evidence for white matter BOLD signal

As mentioned before, white matter is almost always excluded from fMRI studies. However, white matter activation has been reported during specific tasks such as the Poffenberger paradigm or the Sperry paradigm (Gawryluk et al., 2014). During the Poffenberger paradigm, the motor and visual pathways are activated, the motor fibres cross the hemispheres through the body of the corpus callosum, which then gets a positive BOLD signal. Other tasks have shown activation of other white matter regions of the brain (Grajauskas et al., 2019).

A more careful analysis of the corpus callosum BOLD activation resulted in finding completely different hemodynamic response functions (HRFs) compared to grey matter. White matter HRF shows prolonged initial dips, increased time to peak, and smaller magnitudes overall. Additionally, not all white matter has the same HRF (Li et al., 2019b).

One concern about white matter BOLD is that changes in grey matter oxygenation can reach several millimetres beyond the activated region via the venous system, thus potentially producing white matter BOLD activation. However, the venous system of the grey matter is mainly via ascending veins that reach the pial surface, there is no interaction between the two tissues (Duvernoy et al., 1981; Li et al., 2019b).

5. THE AIM OF THIS PH.D. THESIS

White matter is very different from grey matter in terms of energetic demands, NMC mechanisms, HRF, and possibly NVC mechanisms, although this remains to be studied. This is precisely the aim of this thesis, to study NVC in a white matter tract. NMC models of the white matter are in their infancy, and NVC ones are not even being generated so far. Creating models for white matter NVC is critical to understand how the BOLD effect is generated in this tissue and to understand why the white matter is so affected under certain cerebrovascular diseases. This thesis aims to study NVC in a white matter tract of the CNS by elucidating the possible cellular mechanism and to evaluate if oligodendrocytes are involved on it.

RESULTS

The study of *ex vivo* NVC in the CNS white matter is not so trivial. The majority of the white matter in the CNS is localized in the corpus callosum and the spinal cord. Almost all the white matter tracts found in the body are part of the peripheral nervous system. Ideally, there should not be any grey matter vasculature around the tissue since it could potentially mask results and dynamics related to the white matter. Lastly, to evaluate changes in vessel diameters upon axonal activity, the vasculature needs to be easily imaged while the nerve is electrically stimulated at the same time. Considering these conditions, the optic nerve seems to be a good system of choice to study the posed question. It is a CNS white matter tract, and it is not vascularized by grey matter vessels. While it has proven itself very useful to study axonal energetic demands (Trevisiol et al., 2017), myelin and astroglial calcium signalling (Butt et al., 2004; Micu et al., 2016), it remains unknown if the vasculature of the nerve is easily accessible and how it looks like.

1. OPTIC NERVE VASCULATURE CHARACTERIZATION

The murine optic nerve vasculature has been described during development; however, it remains unknown how it is organized in the adult mouse. By using a modified protocol for optical clearing based on the iDISCO protocol (Depp et al., 2021) and a reporter line that expresses eGFP in all perivascular cells (PDGFRβ-eGFP), it was possible to observe in 3D the entire vasculature of the optic nerve (the staining and imaging of the nerves was done by Andrew Octavian Sasmita).

The optic nerve is surprisingly well vascularized and presents a clear organization of the vascular tree (Figure 4). The arteriole, which is covered by vascular smooth muscle cells (Gonzales et al., 2020; Hartmann et al., 2015), is localized in the optic nerve's caudal position, towards the optic chiasm (Figure 4 A, dashed white arrows). As the arteriole goes into the rostral end of the optic nerve, the perivascular cells change shape, and the vessel becomes a pre-capillary arteriole (Figure 4 A white arrowheads). As the pre-capillary arteriole bifurcates and goes further into the tissue, the blood vessels become capillaries, identified by the presence of pericytes (Figure 4 A white arrows). Based on this preparation of the optic nerve, the pre-capillary arteriole seems to run all the way to the rostral part of the nerve, however, it is not clear if it enters the retina or whether external vessels enter at the optic nerve head to form the retinal vasculature. It would be expected to observe the venules coming from the rostral end of the nerve and developing into the vein as they approach the nerve’s caudal part, interestingly that was not the case. Instead, a big vein is coming from the rostral end (Figure 4 A yellow dashed arrows) and bifurcates into several venules almost at the caudal end of the nerve (Figure 4 A yellow arrows and Figure 4 B). The vein is on the opposite side of the arteriole (Figure 4 C).

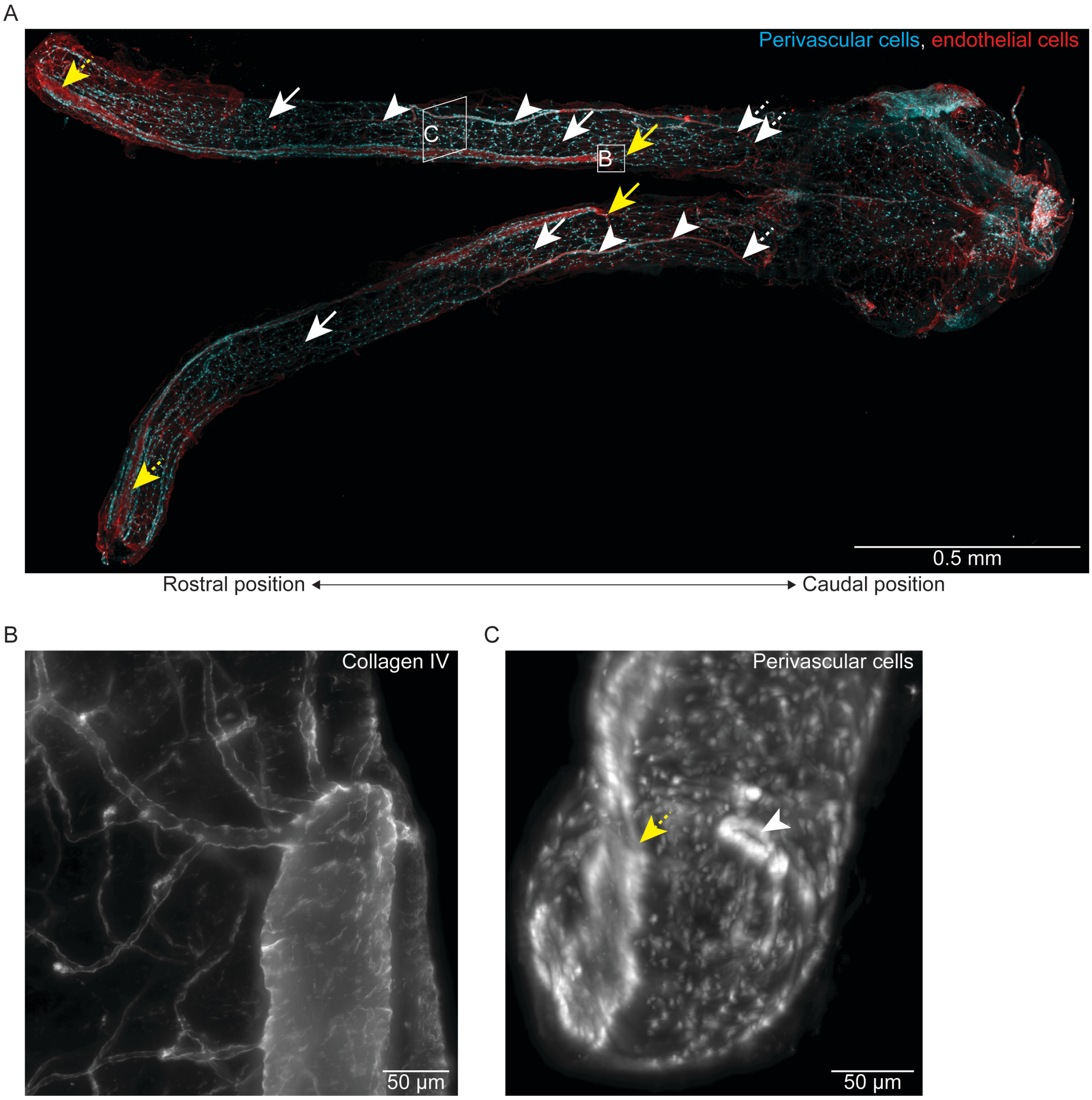

Figure 4: General organization of the optic nerve vasculature. ***A)*** *Light-sheet microscopy image of a fixed optic nerve. Perivascular cells express cytosolic eGFP (cyan) and the endothelial cells are stained for podocalyxin (red). White dashed arrows point towards the arteriole, covered by smooth muscle cells. The white arrowheads point towards the pre-capillary arteriole, covered by ensheathing pericytes. The white arrows point towards capillaries, covered by thin stranded pericytes. The yellow dashed arrows mark a big vein coming out of the rostral end of the optic nerve. The vein is covered by spider pericytes. The yellow arrows point towards small venules. The small square shows an approximate location for images shown in B and C. Those images do not belong to the same image shown in A.* ***B)*** *Confocal microscopy image of a collagen IV staining (grey) in the optic nerve showing the branching of the vein into venules.* ***C)*** *Light-sheet microscopy image of the optic nerve used to showcase the position of the venule (yellow dashed arrow) and the arteriole (white arrowhead). Perivascular cells that express eGFP cytosolically are seen in grey colour.*

The optic nerve in figure 4 shows rich vascularization. It is, however, important to keep in mind that the tissue shrinks almost 3 times during the preparation (from ~6 mm to only 2 mm, including the chiasm). This volume change could account for the observed high vascular density.

The type and morphology of perivascular cells of the optic nerve (Figure 5) seem to be very similar to the perivascular cells of the grey matter. The arteriole is covered by one layer of vascular smooth muscle cells (Figure 5 A, dashed arrows), the pre-capillary arteriole is defined by the presence of ensheathing pericytes (Figure 5 A, solid arrows), and capillaries show the thin-stranded pericytes (Figure 5 B, solid arrows). The venules are also covered by spider, or venular, pericytes (Figure 5 C, solid arrows).

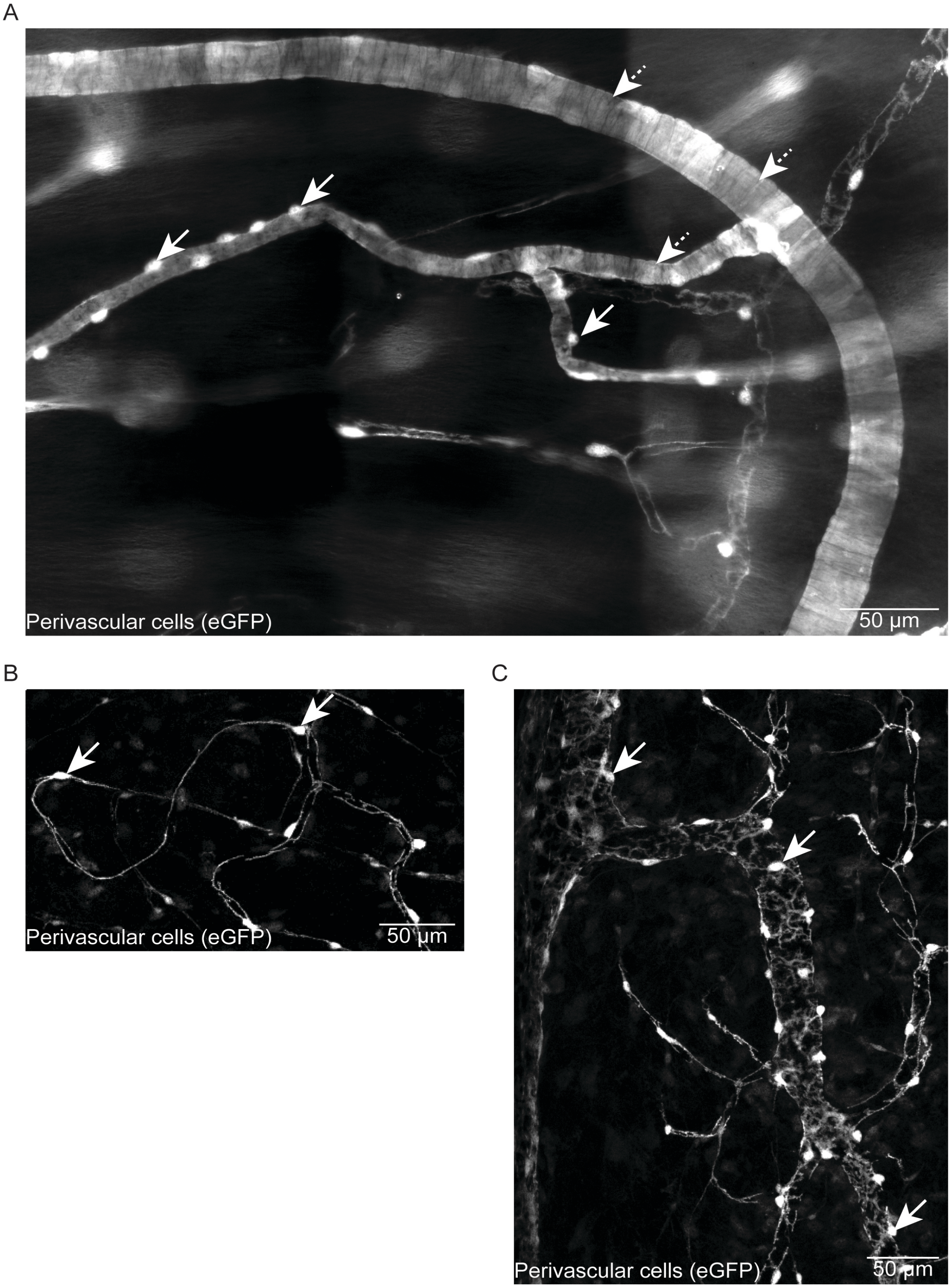

Figure 5: Perivascular cells morphology in the optic nerve. ***A)*** *The arteriole of the optic nerve is covered by morphologically defined smooth muscle cells (dashed arrows). It is possible to see the transition between smooth muscle cells and ensheathing pericyte (solid arrows). Ensheathing pericytes are characterized by a clear "bump in a log" soma, as well as abundant processes that wrap around the vessel. Additionally, they are contiguous to each other on the same vessel.* ***B)*** *Thin-stranded pericytes (solid arrows), are also found in the optic nerve.* ***C)*** *Venular pericytes show a "spider" like morphology (solid arrows). These images are exemplary images that represent typical observation of the optic nerve's perivascular cells.*

As the vasculature of the optic nerve appears to be easily accessible and contains all the cells that have contractile properties, I concluded that it is a suitable system to study NVC in white matter.

2. OPTIC NERVE VASCULATURE REACTS TO KNOWN VASOACTIVE SUBSTANCES

2.1. Cells identification and nomenclature

With the acute preparation of the optic nerve, it is possible to electrically stimulate the axons (Saab et al., 2016; Stys et al., 1991; Trevisiol et al., 2017) and simultaneously image the vasculature to follow the changes in vessel diameter. In this preparation, the optic nerve is separated from the retina and the optic chiasm and clamped in between two suction electrodes (Figure 6 A). The rostral part of the nerve, which was connected to the retina, is sucked into the stimulating electrode, and the caudal part, which was connected to the chiasm, into the recording one. This maintains the natural direction of action potential propagation inside the nerve. The nerve is bathed with a constant flow of aCSF kept at 35°C and oxygenated with carbogen (95% O_2 + 5% CO_2). While the nerve is being stimulated, imaging of the vessels is performed simultaneously using a confocal microscope. To identify the blood vessels, the animal is injected with a tracer, Dextran-Texas Red, before dissecting the optic nerve. Once it is in place, both perivascular cells and the lumen of the blood vessels are visible through the microscope (Figure 6 B). Given that the *ex vivo* preparation removes the vascular tone, a classification of the vessels by their lumen size is not reliable, instead, the classification is done using the morphology of the perivascular cells (Hartmann et al., 2015, 2021).

Contrary to the spindle shape of smooth muscle cells (Figure 6 B_I), all pericytes have the soma with a characteristic "bump in a log" shape. The difference between pericytes is in the organization of the processes. Following published work (Hartmann et al., 2015, 2021), I classified perivascular cells as ensheathing pericytes if there are several of them close together and/or single processes are not discernible (Figure 6 B_{II}). The soma of the mesh pericytes is localized between two processes that wrap the underlying blood vessel as well as thin processes that go along the vessel (Figure 6 B_{III}). Thin-stranded pericytes are characterized by thin long processes that are parallel to the vessel but not wrapped around it (Figure 6 B_{IV}). Finally, venular pericytes have unorganized processes that run along and wrap the blood vessel. This morphology is very characteristic and is unmistakable (Figure 6 B_V).

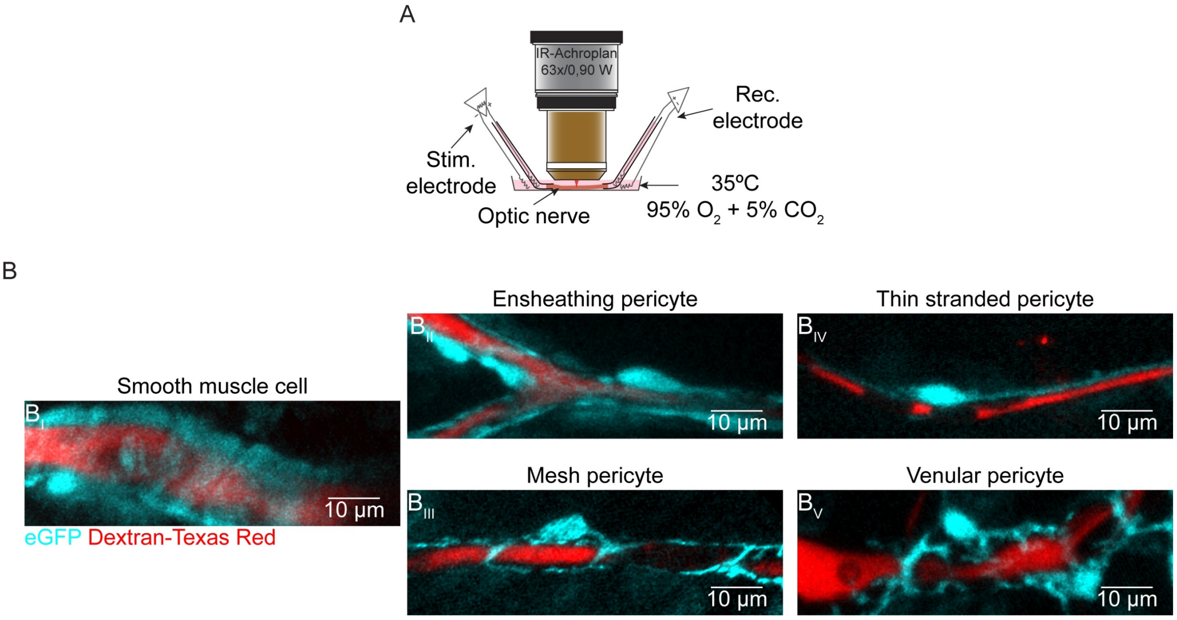

Figure 6: Ex vivo live optic nerve imaging. ***A)*** *Diagram of the setup used for live imaging and electrophysiological stimulation of the optic nerve. The optic nerve is clamped in between two suction electrodes that allow stimulation and recording of the compound action potential of the nerve. At the same time, a confocal microscope allows imaging of the blood vessels as well as perivascular cells.* ***B)*** *Representative images of all the different perivascular cells observed in the optic nerve by confocal microscopy. The morphology of each cell was used to classify them in the different cell types. The gaps in the lumen of the blood vessels (red) are caused by the complete collapse of the vessel or by neutrophils stuck inside the vessel* (Cruz Hernández et al., 2019; Rolfes et al., 2021).

2.2. Vasoactive substance effect

To test if the blood vessels in this preparation are still capable of dilating and constricting, I used two very common vasoactive substances used in *ex vivo* preparations: U46619 and acetylcholine (ACh). U46619 is a thromboxane A2 analogue that binds to the thromboxane (TP) receptor located in a variety of cells. In the brain, it is expressed by endothelial cells, smooth muscle cells, and pericytes (Vanlandewijck et al., 2018). Upon TP receptor activation, calcium concentration increases inside the perivascular cell via G coupled proteins and triggers the vasoconstriction (Jabbour and Sales, 2004).

ACh has been used since the early ’80s to induce dilation of arteries experimentally (Ludmer et al., 1986). ACh binds to muscarinic receptors on the endothelial cells inducing the production of nitric oxide via endothelial nitric oxide synthase. Nitric oxide has a paracrine activity in the perivascular cell (Garthwaite et al., 2006), and induces a relaxation of the cell causing blood vessel dilation. Recent single-cell RNA sequencing data shows the presence of 3, out of 4, subunits of the nitric oxide receptor expressed in thin-stranded pericytes, ensheathing pericytes and smooth muscle cells (Vanlandewijck et al., 2018), indicating that ACh can potentially induce dilation of pre-capillary arterioles as well as in capillaries.

To test if all perivascular cells have contractile properties in the optic nerve, I imaged ensheathing pericytes (EP), mesh pericytes (MP), and thin-stranded pericytes (TSP) during a chemical stimulation to induce a vasoactive response (Figure 7). U46619 (100 nM) elicited an almost immediate constriction in all three cell types and remained stable after 15 minutes (Figure 7 A). The constriction was reversed by ACh (100 µM), which elicited a strong dilation (Figure 7 A). Only ensheathing and mesh pericytes exhibited strong vasoactive responses to both substances (Figure 7 B and C). As both ensheathing and mesh pericytes behaved comparably to each other, I pulled them together as one population that constricted 20.38% ± 3.53% over the baseline levels, meanwhile, thin-stranded pericytes constricted 5.06% ± 5.44%, making a significant difference of 15.32% (n EP and MP= 4, n TSP= 7; p-value: 0.0014 using an unpaired two-tailed t-test). Upon treatment with ACh, ensheathing and mesh pericytes dilated 15% ± 2.80% over the constricted level (dashed line in Figure 7 A, curve EP, MP). Thin-stranded pericytes dilated 3.13% ± 5.85% over the constricted level, resulting in a difference of 12.20% in Ach-induced dilation (n EP and MP= 4, n TSP= 7; p-value: 0.0063 using an unpaired two-tailed t-test).

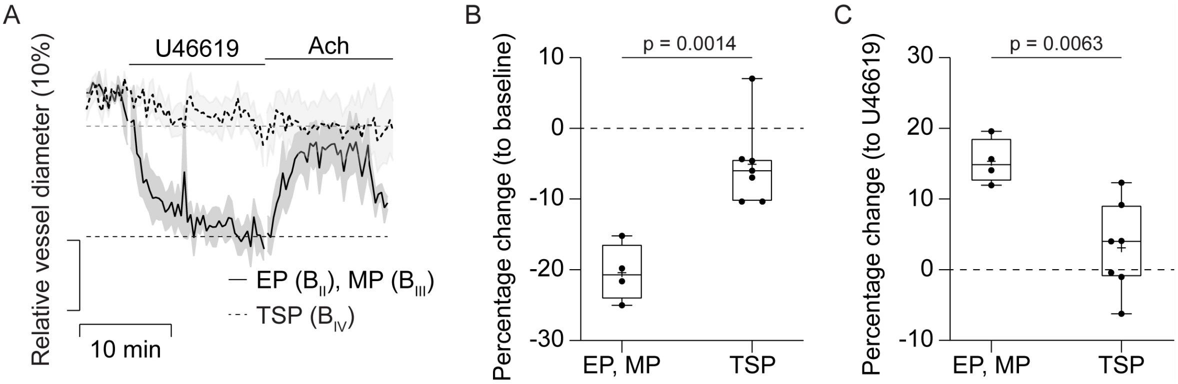

Figure 7: Ensheathing and mesh pericytes but not thin-stranded pericytes have contractile properties. ***A)*** *Optic nerves were bathed with the constrictor U46619 (100 nM) for 15 min followed by 15 min of acetylcholine (100 µM). Based on the type of perivascular cell, the vessels were pulled together in two groups.* B_{II}, B_{III}, *and* B_{IV} *refer to the images in Figure 6. Only the vessels with ensheathing or mesh pericytes (n= 4) were capable of constricting and dilating upon the chemical treatment. Vessels with thin-stranded pericytes (n= 7) show a very slow and small constriction but almost no dilation. The dotted lines show the vessel size at the end of the preconstriction (black for EP and MP, and grey for TSP).* ***B)*** *Quantification of the last 2 min of preconstriction for both groups (EP-MP, and TSP). Ensheathing and mesh pericytes constricted 20.38% ± 3.53%. Thin-stranded pericytes constricted 5.06% ± 5.44% over the baseline level (5 min before the onset of U46619 treatment). p-value: 0.0014; unpaired two-tailed t-test correction.* ***C)*** *Quantification of 2 min around the maximal dilation during acetylcholine treatment for both groups (EP-MP, and TSP). Ensheathing and mesh pericytes dilated 15% ± 2.80% over the preconstricted levels (shown by the dotted line in A). Thin-stranded pericytes dilated 3.13% ± 5.85% over the preconstricted levels (shown by the dotted line in panel A). p-value; 0.0063; unpaired two-tailed t-test.*

These data show that in white matter, similarly to grey matter (Gonzales et al., 2020), only ensheathing and mesh pericytes are capable of constricting and dilating upon chemical treatments. Additionally, the constriction with U46619 seems to be slightly smaller compared to grey matter vessels where ensheathing pericytes constrict ~35% and thin-stranded pericyte around ~5% (Gonzales et al., 2020). It is possible that the myelin that composes the white matter, acts as a diffusion barrier for pharmacological agents to penetrate.

Based on these results, the rest of this work focuses on vessels with ensheathing or mesh pericytes.

3. NEUROVASCULAR COUPLING IN THE OPTIC NERVE

The next step to study NVC is to electrically stimulate the axons of the nerve and determine if there is a concomitant vascular response. Studies from guinea pigs showed that the firing rate of the retinal ganglion cells that project their axons in the optic nerve is dependent on their axonal diameter. Most axons have a small diameter (< 0.9 µm) and fire at 4 Hz, however, the firing rate curve goes from 0 Hz to ~ 29 Hz (Perge et al., 2009).

To study the effect of stimulation on vessel dilation (Figure 8), vessels need to be preconstricted to maintain an artificial vascular tone (Mishra et al., 2014). For the preconstriction, I used U46619, which showed a robust effect (Figure 7). The electrical stimulation lasted 3 min and was followed by a recovery period without stimulation of 30 min. Since cells may die during the experiment giving false responses to electrical stimulation, I used ACh as a positive control to ensure that the imaged vessels were still alive at the end of the experiment.

I used three different frequencies corresponding to three different physiological states. The most physiological firing rate of the optic nerve and neurons in the cortex is represented by 4 Hz (Figure 8 A) (Attwell and Laughlin, 2001; Perge et al., 2009). The maximal firing rate of the optic nerve is ~29 Hz (Perge et al., 2009), thus to represent a state of maximal stimulation I used 25 Hz (Figure 8 B), while 100 Hz (Figure 8 C) represent a supraphysiological state where conduction blocks are created in the axons, thus inhibiting the proper propagation of action potentials (Trevisiol et al., 2017). In all three frequencies, the vessels dilate during the stimulation period of 3 min, however, the dilation continued during the recovery period of 30 min where it reached a maximal dilation. The vessels of the nerves that were stimulated at 4 Hz dilate 1.23% ± 1.19% during the stimulation and a further 5.64%, to reach 6.88% ± 0.54% during the recovery (n= 7; p-value: 0.0008; One-way ANOVA with multiple comparisons using 3 pairs). The vessels of the nerves that were stimulated at 25 Hz dilate 2.38% ± 1.78% during stimulation and a further 3.82%, to reach 6.23% ± 2.41%, dilation over the constricted level, during the recovery (n= 7; p-value: 0.0268; One-way ANOVA with multiple comparisons using 3 pairs). Lastly, the vessels of the nerves that were stimulated at 100 Hz dilate 2.27% ± 1.64% during stimulation and a further 6.93% during the recovery, to reach 9.20% ± 4.97% dilation over the constricted level (Figure 8 D) (n= 5; p-value: 0.0005; One-way ANOVA with multiple comparisons using 3 pairs). There were no statistical differences between the vessel dilation at the end of the stimulation between the 3 different frequencies (p-value 4 Hz vs. 25 Hz: 0.7937; p-value 4 Hz vs. 100 Hz: 0.8710; p-value 25 Hz vs. 100 Hz: 0.9998; One-way ANOVA with multiple comparisons using 3 pairs). These data suggest that the increase in frequency stimulation does not increase the vessel dilation but instead makes the vessel dilation less reliable, shown by the increased variability of each data set.

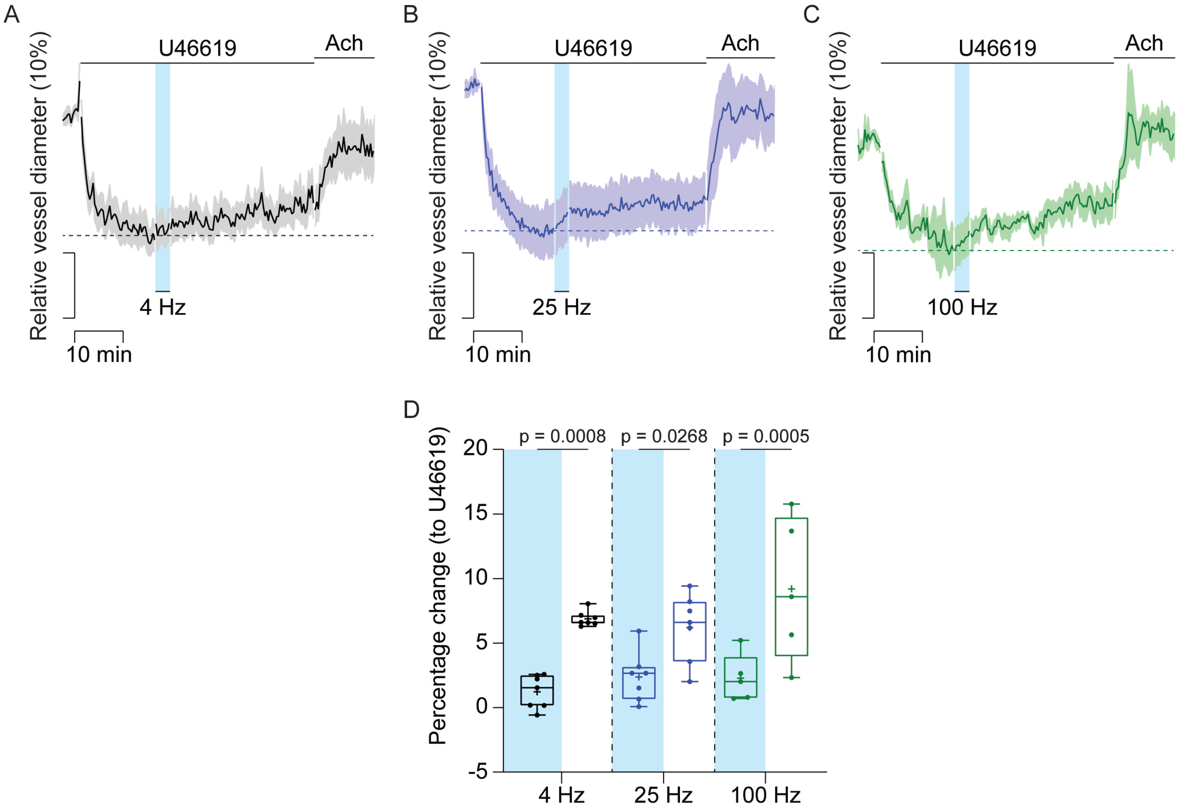

Figure 8: Neurovascular coupling can be studied ex vivo in the optic nerve. ***A)*** *Optic nerves were preconstricted with U46619 (100 nM) and stimulated at 4 Hz (n= 7),* ***B)*** *25 Hz (n= 7), and* ***C)*** *100 Hz (n= 5) for 3 min followed by a recovery period of 30 min. The experiment was terminated after the application of acetylcholine (100 µM) for 15 min. The dotted line shows the preconstriction level. The blue shaded block indicates the stimulation window.* ***D)*** *Quantification of the dilation percentage of the vessels during the stimulation (blue shaded block) and the recovery period for each frequency of stimulation. Nerves stimulated at 4 Hz dilate 1.23% ± 1.19% during the stimulation and 6.88% ± 0.54% during the recovery period (p-value: 0.0008; One-way ANOVA with multiple comparisons using 3 pairs). Nerves stimulated at 25 Hz dilate 2.38% ± 1.78% during the stimulation and 6.23% ± 2.41% during the recovery period (p-value: 0.0268; One-way ANOVA with multiple comparisons using 3 pairs). Nerves stimulated at 100 Hz dilate 2.27% ± 1.64% during the stimulation and 9.20% ± 4.97% during the recovery period (p-value: 0.0005; One-way ANOVA with multiple comparisons using 3 pairs).*

Furthermore, there is no difference in the time needed to reach a maximal dilation in all the stimulation periods (4 Hz: 2.12 min ± 0.74 min; 25 Hz: 1.72 min ± 0.71 min; 100 Hz: 2.21 min ± 0.88 min) (Figure 9 A) and the recovery period (4 Hz: 24.78 min ± 6.71 min; 25 Hz: 18.89 min ± 8.48 min; 18.03 min ± 4.64 min) (Figure 9 B). Additionally, there is no difference in the effect of the preconstriction (U46619 – p-value: > 0.99 for all comparisons using Kruskal-Wallis test with multiple comparisons using 3 pairs) or dilator (ACh – p-value: > 0.99 for all comparisons using Kruskal-Wallis test with multiple comparisons using 3 pairs) between the three groups (Figure 9 C).

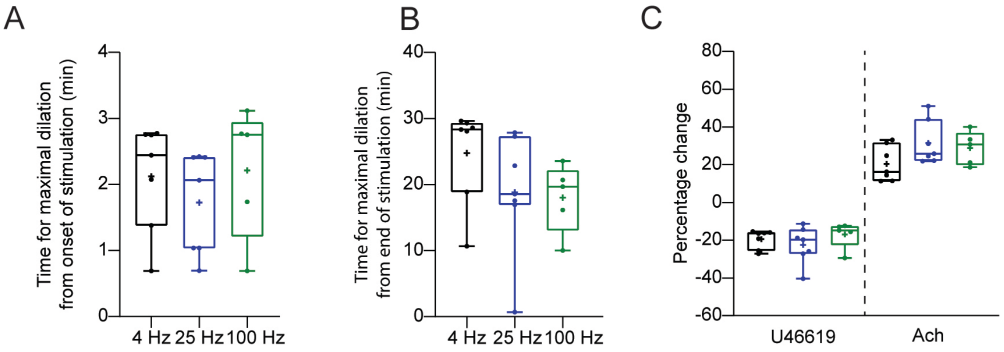

Figure 9: Time for maximal dilation is not dependent on the stimulation frequency. ***A)*** *The time of each vessel to reach the maximal dilation during the stimulation did not change with the increase in stimulation frequency: 4 Hz: 2.12 min ± 0.74 min; 25 Hz: 1.72 min ± 0.71 min; 100 Hz: 2.21 min ± 0.88 min. The one-way ANOVA with multiple comparisons using 3 pairs test did not show significant change between the three frequencies (4 Hz-25 Hz: p-value= 0.6583; 4 Hz-100 Hz: p-value= 0.9827; 25 Hz-100 Hz: p-value= 0.5968).* ***B)*** *The time to reach the maximal dilation during the recovery period did not change with the increase in stimulation frequency: 4 Hz: 24.78 min ± 6.71 min; 25 Hz: 18.89 min ± 8.48 min; 18.03 min ± 4.64 min. A Kruskal-Wallis test with multiple comparisons using 3 pairs did not show significant change between the three frequencies (4 Hz-25 Hz: p-value= 0.1920; 4 Hz-100 Hz: p-value= 0.1660; 25 Hz-100 Hz: p-value> 0.99).* ***C)*** *The percentage change of the preconstriction, over the baseline (p-value: > 0.99 for all comparisons using Kruskal-Wallis test with multiple comparisons using 3 pairs) and acetylcholine, over the preconstriction, (p-value: > 0.99 for all comparisons using Kruskal-Wallis test with multiple comparisons using 3 pairs) was comparable between the three groups.*

To confirm that the above dilation was not due to a decreased effect of the U46619 during the experiment, I performed the same experiment using a minimal basal electrical stimulation of 0.1 Hz (Figure 10). The effectivity of the U46619 is unchanged during the experiment (Figure 10 A). The vessels did not dilate during the baseline stimulation period (0.25% ± 1.04%) or during the recovery period of 30 min after that (0.27% ± 0.92%) (n= 8) (Figure 10 B). The response to the ACh was as expected.

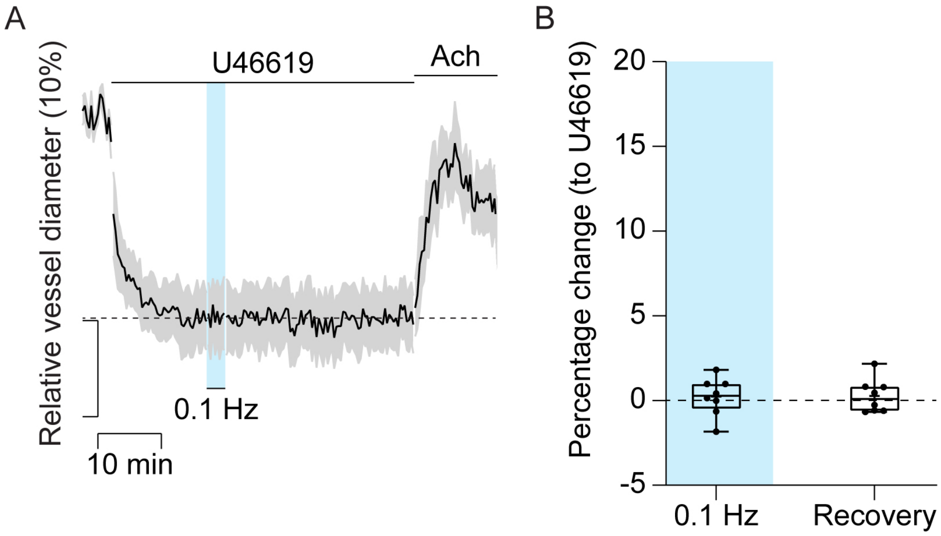

Figure 10: The constriction effect of U46619 is maintained for the entire duration of the experiment. ***A)*** *The vessel diameter does not change over time if only basal stimulation is applied (n= 8). The dotted line shows the preconstriction level.* ***B)*** *Quantification of the vessel diameter during the basal stimulation (0.25% ± 1.04% dilation over the preconstricted level) and the recovery period (0.27% ± 0.92% dilation over the preconstriction). p-value = 0.97 using an unpaired two-tailed t-test.*

To corroborate that the electrical stimulation causes vessel dilation, I inhibited the firing of action potentials along the nerve using tetrodotoxin (TTX) (Figure 11). To allow TTX (1 µM) to fully penetrate the entire optic nerve, it was applied 10 min before the electrical stimulation and was kept flowing until the ACh treatment started. For this experiment, only 100 Hz was used (Figure 11 A). The blood vessels did not dilate either during the stimulation (-1.17% ± 2.27%) or during the recovery period (-0.06% ± 4.54%) (n= 8) (Figure 11 B). The efficacy of the TTX was confirmed by plotting the compound action potential (CAP) of the nerve. The quantification of the CAP measures the area under the curve of the measured waveform (not shown). The area is proportional to the amount of firing fibres (Stys et al., 1991). There was complete inhibition of the action potential firing of the nerve, even during the superfusion of ACh (Figure 11 C), indicating that all the fibres of the nerves were silenced with the TTX. These results support that electrical stimulation via action potential generation mediates the dilation of the vessels in the optic nerve.

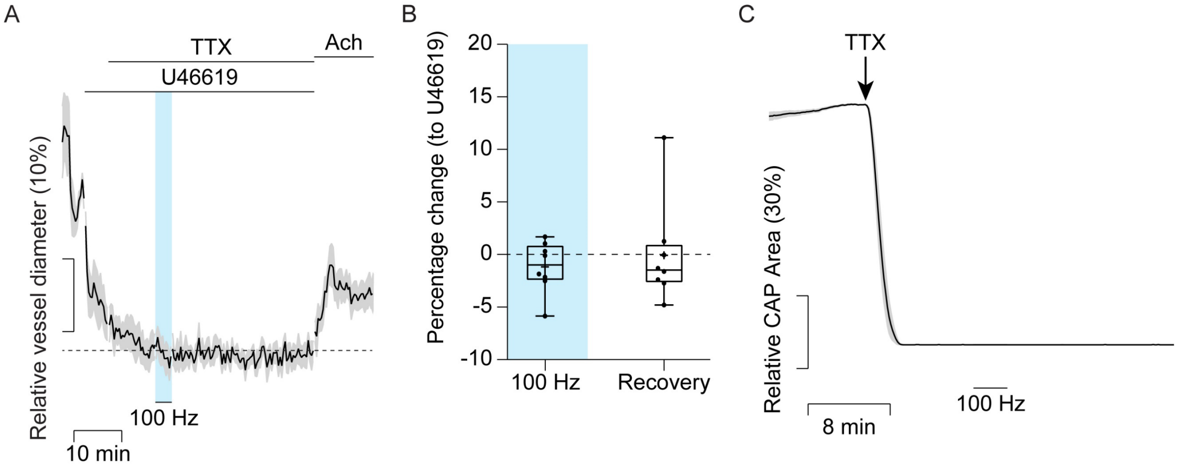

Figure 11: Vessel dilation in the optic nerve is abolished by the inhibition of action potential firing. ***A)*** *Nerves were exposed to TTX (1 µM) 10 min before a stimulation with 100 Hz and was kept during the recovery period (n= 8).* ***B)*** *Quantification of the percentage change of the vessel diameter over the preconstricted level (dotted line in panel A). During the stimulation of 100 Hz, the vessels had a further constriction of -1.17% ± 2.27%. During the recovery period, the vessels did not dilate any further than the preconstricted level (-0.06% ± 4.54%). p-value > 0.99 using a Mann-Whitney two-tailed t-test.* ***C)*** *Compound action potential area of the optic nerve during TTX superfusion. The onset of TTX treatment is indicated by the arrow.*

Since the electrical stimulation that I used was mainly supraphysiological, it is important to monitor the overall axonal activity to rule out any detrimental effects on the conduction of action potentials in the nerve. For this, I measured CAPs of the nerves during the experiment (Figure 12). The shape of the CAP waveform can be used for qualitative analysis. The area under the curve of the waveform is proportional to the number of firing axons (Stys et al., 1991) and can be analysed to see changes in axonal activity over time. Therefore, I recorded the CAP for all three stimulation frequencies and examined the waveform and the area under the curve. During stimulation, the relative CAP area decreases compared to the baseline. After 3 min of 4 Hz, 25 Hz, and 100 Hz stimulation, 95% (Figure 12 B), 84% (Figure 12 D), and 52% (Figure 12 F) of the fibres are still firing, respectively. These reduction in firing axons during the stimulation is due to conduction blocks created by fibres that are not capable of repolarizing during the stimulation. However, 20 min

Twenty min after the end of the stimulation, 98% of the fibres recover for all three frequencies (Figure 12 A, C, and E). this recovery indicates that the axons, and thus the overall conduction properties and health of the optic nerve, is not affected by the stimulation paradigms.

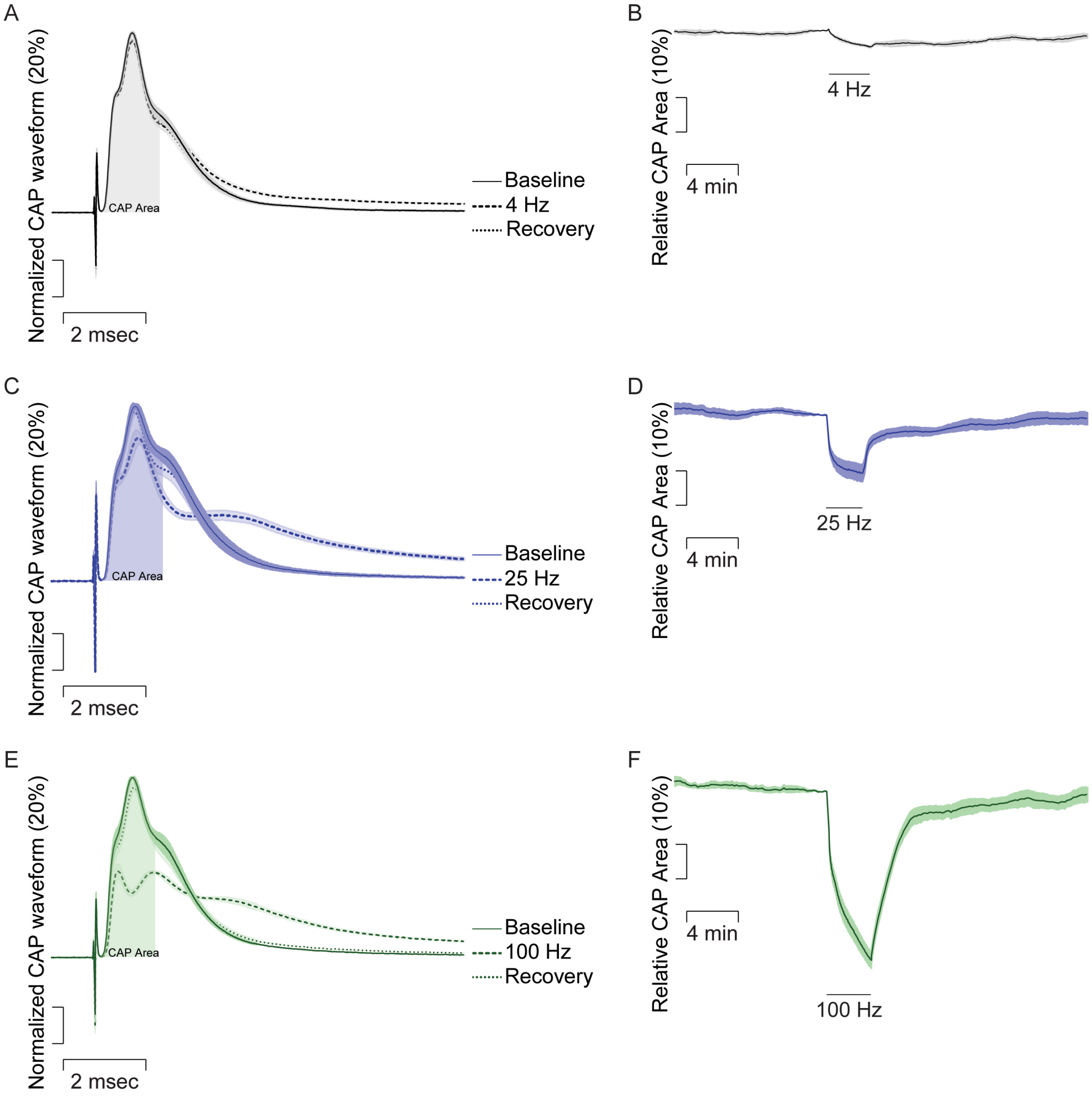

Figure 12: Action potential conduction is not affected by the stimulation paradigm. ***A)*** *Average waveform of the CAP recorded during 4 Hz,* ***C)*** *25 Hz, and* ***E)*** *100 Hz stimulations. Plotted is the*

average waveform at three time points: at the end of the baseline (solid line), at the end of the stimulation (dashed line), and after 5 min of recovery (dotted line). The shaded block shows the area used for quantification. ***B)*** *Quantification of the area under the curve of the waveform over the time for 4 Hz,* ***D)*** *25 Hz, and* ***F)*** *100 Hz stimulation. It is marked when the stimulation takes place.*

Overall, these data show that it is possible to study NVC in an *ex vivo* optic nerve preparation. The contractile properties of the perivascular cells, upon constriction with U46619, are similar to the ones reported for grey matter (Fernandez-Klett et al., 2010; Gonzales et al., 2020; Mishra et al., 2016). However, the speed of, and the dilation percentage are very different. In grey matter, upon short (5 sec) local field stimulation of cortical fibres, vessels dilate 14.5% ± 0.5% over the preconstricted levels in less than 5 min after the end of the stimulation (Hall et al., 2014; Mishra et al., 2016). In the optic nerve, upon long (3 min) stimulation of axonal fibres, vessels dilate, around 7%, depending on the stimulation frequency, in approximately 20 min after the end of the stimulation (Figure 8 and Figure 9).

It has been shown by others, and me, that different stimulation frequencies have a different effect on axon conduction (Figure 12) and ATP consumption (Trevisiol et al., 2017), but it seems not to hold true for vessel dilation. The used stimulation frequencies, except for 4 Hz, induce consumption of ATP by the axons (Trevisiol et al., 2017). According to the neurometabolic coupling hypothesis, axons that are using ATP (stimulated at 25 Hz and 100 Hz) are signalling to oligodendrocytes to induce more glycolysis. The vessels should then dilate to increase the metabolite supply. However, it seems that the increase in stimulation frequency does not induce a statistically significant increase in vessel dilation (Figure 8). Instead, there is a sustained dilation over time, that probably supports the entire optic nerve and not just single synapses as is the case for grey matter.

4. THE NVC IN THE OPTIC NERVE SUMS UP THE RESPONSE TO DIFFERENT STIMULATIONS

Based on the results from the previous section, the NVC in the optic nerve operates differently than the NVC in grey matter. Primarily, the dilated vessel does not go back to baseline after the stimulation of the optic nerve, as is the case in grey matter. Instead, vessel diameter seems to continuously increase over a 30 min period. This can be due to the more interconnected cellular organization of the white matter, compared to the grey matter. It appears to be a summation of the NVC signal that does not allow the vessel diameter to return to baseline.

To further characterize the NVC in white matter, I stimulated the optic nerve with a single frequency of 16 Hz, which is below the maximal firing limit of 25 Hz (Perge et al., 2009). In addition, NVC at 16 Hz stimulation might be still functional since this frequency has been shown to cause ATP consumption (Trevisiol et al., 2017), and probably, the conduction blocks are not as strong as with higher stimulation frequencies. I used a repetitive stimulation paradigm in which different stimulation durations was followed by different recovery periods (Figure 13). In this paradigm, the nerve is stimulated for 10 min, 5 min, 2.5 min, 1 min, and 6 sec with recovery periods of 30 min, 15 min, 7.5 min, 6 min and 6 min in between each stimulation. Although it is difficult to compare this stimulation paradigm with the NVC response from the previously shown data, it is interesting to see that the vessel diameter progressively dilates to reach a maximum after 70 min (15.2% ± 3.59% over the preconstriction levels) and then decreases even if the nerves are still being stimulated (Figure 13 A).

The 10 min stimulation induces dilation of 1.48% ± 1.05%. This percentage is in between the dilation evoked by 4 Hz and 25 Hz (Figure 8). The second stimulation (5 min) induces dilation of 6.68% ± 2.25% over the preconstricted level. This represents an increase of 0.85% over the vessel diameter after the previous recovery period (30 min). The third stimulation (2.5 min) induces a dilation of 11.97% ± 3.20%, which represents an increase of 2.53% over the level after the second recovery period (15 min). After the following recovery period (7.5 min), where the vessels reach the maximal dilation of 15.22% ± 3.29%, the stimulations and recovery periods do not induce further dilation of the vessels (Figure 13 B). Instead, the vessel diameter starts to decrease despite being stimulated. The observed ACh response ensures the viability of the vessels after the experiment, verifying that the lack of dilation is not due to the cells dying or losing contractile properties.

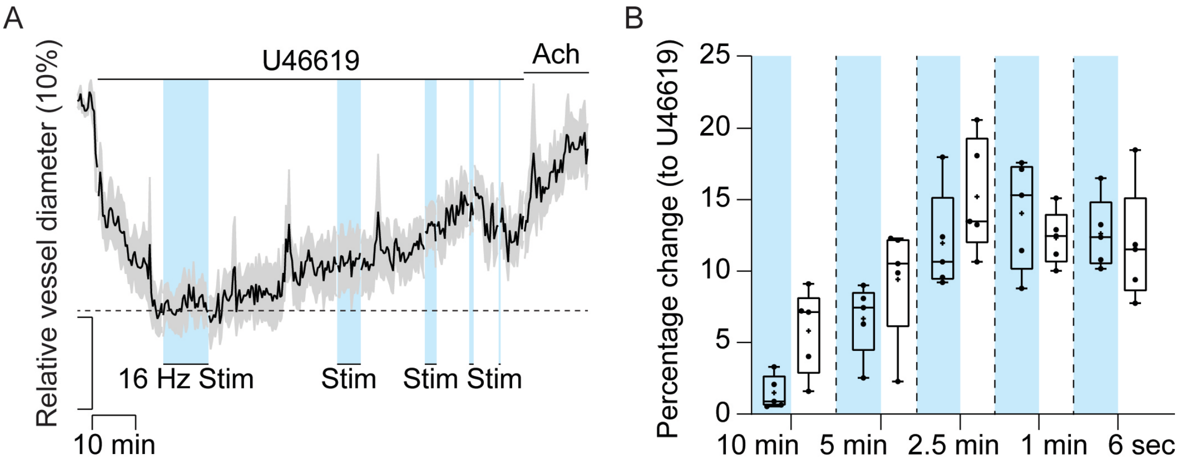

Figure 13: White matter NVC accumulates stimulations. ***A)*** *Optic nerves (n = 5) were stimulated with 16 Hz for different periods of time and different recovery periods in between each stimulation. The blue boxes show the period of stimulation.* ***B)*** *Quantification of the percentage change of the vessel diameter over the preconstricted levels. The 10 min stimulation induces a 1.48% ± 1.05% followed by a recovery period of 30 min where the vessels dilate to a further 5.82% ± 2.66%. The 5 min stimulation dilates the vessels to a further 6.68% ± 2.25% followed by a dilation of 9.43% ± 3.69% during the 15 min recovery period. The third stimulation of 2.5 min dilates the vessels to 11.97% ± 3.20% over the preconstricted level. The following recovery period reached the maximal dilation of 15.22% ± 3.59%. From here, the stimulations do not induce dilation, instead, the vessels start to decrease their diameter. After 1 min stimulation, the percentage change over the preconstricted level is 14.05% ± 3.40%, which is a decrease of 1.16% compared to the previous recovery period. During the following 6 min recovery, the vessel size is reduced to 12.34% ± 1.71%. The last stimulation, which lasts 6 sec, brings the vessel diameter to 12.62% ± 2.23% over the preconstricted levels. The last recovery period let the vessel reach a vessel diameter of 11.81% ± 3.66% over the preconstriction.*

It would be interesting to know if the dilation, after a single 10 min stimulation, would go back to baseline after 70 min of recovery, as it seems to be the case (Figure 13).

5. WHITE MATTER NEUROVASCULAR COUPLING MECHANISM

5.1. EP_4 receptor

The published pathway of grey matter NVC indicates that astrocytes secrete prostaglandin E2, which activates the EP_4 receptor in perivascular cells (Vanlandewijck et al., 2018) and induces vessel dilation in the cortex (Mishra et al., 2016). To evaluate if the EP_4 receptor is involved in NVC in white matter, I used the EP_4 receptor inhibitor L161,982 (1 µM) in the *ex vivo* optic nerve preparation (Figure 14). L161,982 was added 10 min before U46619 to evaluate if prostaglandin E2 is involved in maintaining the remaining vascular tone of the vessels in the optic nerve (Figure 14 A). The superfusion of L161,982 does not change the vessel size compared to the control experiment, in which only the vehicle (DMSO) was superfused (Figure 14 B). Before the addition of U46619, the vessel size of the DMSO treated vessels was -1.76% ± 2.00%, and the vessel size of the L161,982 treated vessels was -1.94% ± 5.21%. As there is no considerable reduction in vessel size with the EP_4 inhibitor, I conclude that prostaglandin E2 is not required to maintain the white matter's vascular tone. This is consistent with grey matter data (Mishra et al., 2016).

The quantification of the percentage change of the vessel diameter (Figure 14 C) shows no difference between the control and the inhibitor. Vessels of the nerves treated with the inhibitor dilated 2.43% ± 0.96% after the 25 Hz stimulation, while DMSO treated nerves showed a vessel diameter change of 1.73% ± 1.84% (n L161,982 = 7; n DMSO = 5; p-value: > 0.99 with a Kruskal-Wallis test using 4 pairs for multiple comparisons). During the recovery period, vessels dilate further to 7.57% ± 3.99% under L161,982 treatment. With DMSO superfusion, vessels increase a further 5.40% ± 4.35% over the preconstricted level (p-value: > 0.99 with a Kruskal-Wallis test using 4 pairs for multiple comparisons). Although in this experiment there seems to not be a statistically difference between the vessel diameter at the end of the stimulation and at the end of the recovery period, like in previous experiments, there is a clear trend of diameter increase during the recovery period (DMSO stim vs. recovery: p-value= 0.3026; L161,982 stim vs. recovery: p-value= 0.3245 with a Kruskal-Wallis test using 4 pairs for multiple comparisons).

The time needed to reach a maximal dilation did not show any difference between treatments either. During the stimulation (Figure 14 D), the vessels needed 1.87 min ± 0.64 min for DMSO treated nerves to reach a maximal dilation, and 2.21 min ± 0.16 min for L161,982 treated nerves (p-value = 0.4318 using a Mann-Whitney test). During the recovery period (Figure 14 E), the vessels treated with DMSO needed 21.31 min ± 6.97 min, and the vessels treated with L161,982 needed 18.87 min ± 5.54 min to reach the maximal dilation (p-value = 0.5949, using an unpaired t-test).

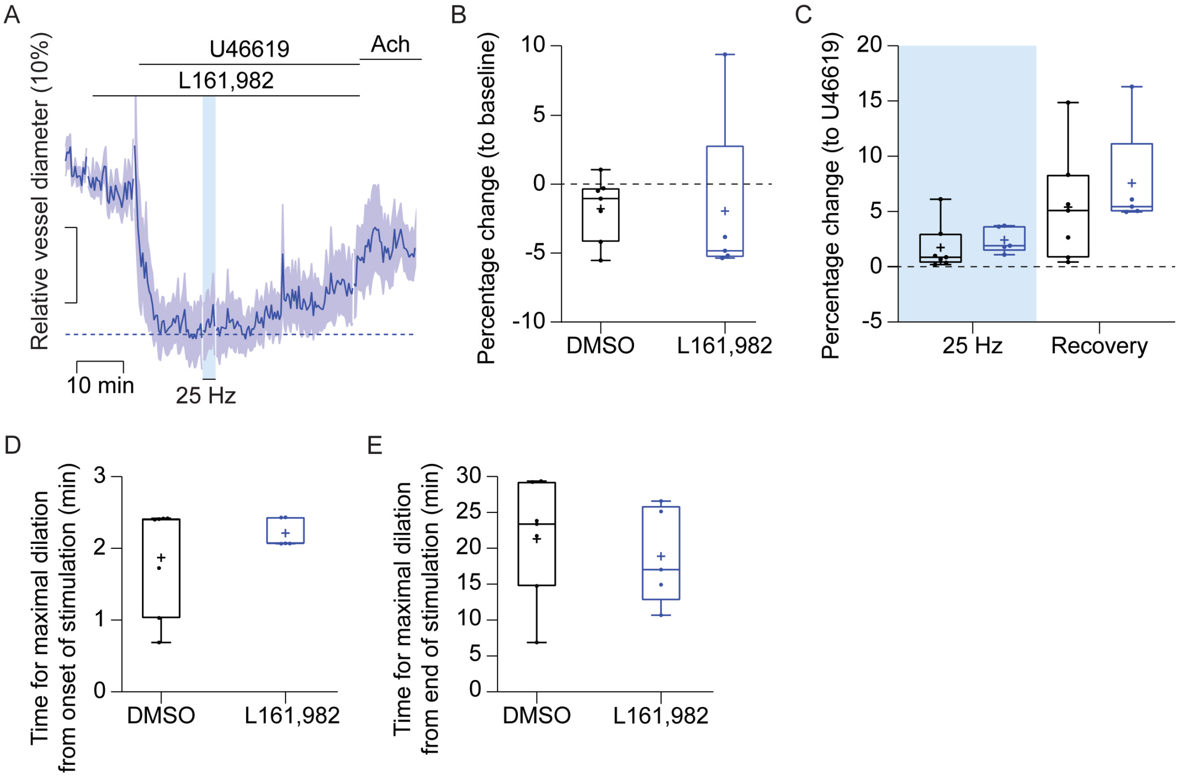

Figure 14: EP_4 receptor is not involved in NVC in the optic nerve. ***A)*** *EP_4 receptor inhibitor L161,982 was superfused 10 min before the application of U46619 to evaluate the dependence of the vascular tone on prostaglandin E2 and kept for the entire duration of the recovery period. The dotted line shows the preconstriction level. The blue shaded block shows where the stimulation happens.* ***B)*** *Quantification of the vessel diameter after L161,982 demonstrate that the vascular tone is not dependent on prostaglandin E2 (DMSO percentage change to the baseline -1.76% ± 2.00% (n = 7); L161,982 percentage change to baseline -1.94% ± 5.21% (n = 5). p-value = 0.4318 with a Mann-Whitney unpaired test).* ***C)*** *Quantification of the vessel diameter after stimulation at 25 Hz and recovery for 30 min. DMSO treated nerves dilate 1.73% ± 1.84% after stimulation, while, L161,982 treated vessels dilate 2.43% ± 0.96% (p-value > 0.99 with a Kruskal-Wallis test using 4 pairs for multiple comparisons). After 30 min recovery, the control nerves dilated 5.40% ± 4.35% over the preconstricted levels. The vessels treated with L161982 dilated 7.57% ± 3.99% over the preconstricted levels (p-value: > 0.99 with a Kruskal-Wallis test using 4 pairs for multiple comparisons).* ***D)*** *Time needed to reach the maximal dilation during the stimulation period. DMSO treated vessels needed 1.87 min ± 0.64 min to reach the maximal dilation. L161,982 increased the time to 2.21 min ± 0.16 min (p-value = 0.4318 using a Mann-Whitney test).* ***E)*** *Time needed to reach the maximal dilation after the recovery period. DMSO treated vessels needed 21.31 min ± 6.97 min. L161,982 decreased the time to 18.87 min ± 5.54 min (p-value = 0.5949, using an unpaired t-test).*

I conclude that prostaglandin E2, via EP_4 receptor, is not responsible for the vessel dilation in the optic nerve, contrary to the grey matter (Hall et al., 2014; Mishra et al., 2016). Nevertheless, it is still possible that prostaglandin E2, or another prostaglandin, is mediating the response via another receptor.

5.2. COX enzymes

Prostaglandins are produced from a prostaglandin precursor which is synthesized by two cyclooxygenases, COX1 and COX2 (Vane et al., 1998). In cortical astrocytes, COX1 has been shown to produce prostaglandin H2, which can be metabolized to produce prostaglandin E2 or prostacyclin (Mishra et al., 2016).

To study if COX1 or COX2 are involved in NVC in the optic nerve, I used indomethacin (25 µM) to block, in a non-selective way, both enzymes (Mishra et al., 2016; Vane et al., 1998) (Figure 15). Indomethacin was applied 10 min before the 25 Hz stimulation started (Figure 15 A). The quantification of the vessel dilation to the preconstricted levels shows no difference between the inhibitor and the DMSO control. After the 25 Hz stimulation, there is a difference in dilation of 0.09% between the control and the inhibitor (DMSO: 1.70% ± 1.01% (n= 6); Indomethacin: 1.79% ± 1.12% (n= 5); p-value > 0.99 using a Kruskal-Wallis test with multiple comparisons using 4 pairs). Thirty min after the end of the stimulation, there is a difference of 0.20% between both treatments (DMSO: 6.44% ± 3.25%; Indomethacin: 6.64% ± 2.64%; p-value > 0.99 using a Kruskal-Wallis test with multiple comparisons using 4 pairs). As before, there is a difference between the stimulation and the recovery in the percentage change of the diameter of the vessels. For the DMSO treated vessels, there is an increase of 4.73% (p-value = 0.0178 using a Kruskal-Wallis test with multiple comparisons using 4 pairs), and for the indomethacin treated vessels, there is an increase of 4.84% (p-value = 0.0220 using a Kruskal-Wallis test with multiple comparisons using 4 pairs) (Figure 15 B).

The kinetics of vessel dilation is again not changed between both treatments (Figure 15 C and D). During the stimulation, control vessels reach a maximal dilation after 1.55 min ± 0.55 min while the indomethacin-treated vessels need 1.79 min ± 0.33 min to reach the maximal dilation (p-value = 0.4634 using a two-tailed unpaired t-test). During the recovery period, the DMSO-treated vessels reach the maximal dilation at 26.00 min ± 3.31 min. However, the vessels treated with the inhibitor need 18.92 min ± 5.89 min to reach the maximal dilation (p-value = 0.0501 using a two-tailed unpaired t-test). Although there is a considerable difference, the variability of the vessels treated with indomethacin is very high, thus making it difficult to assess if there is a real difference in kinetics or not.

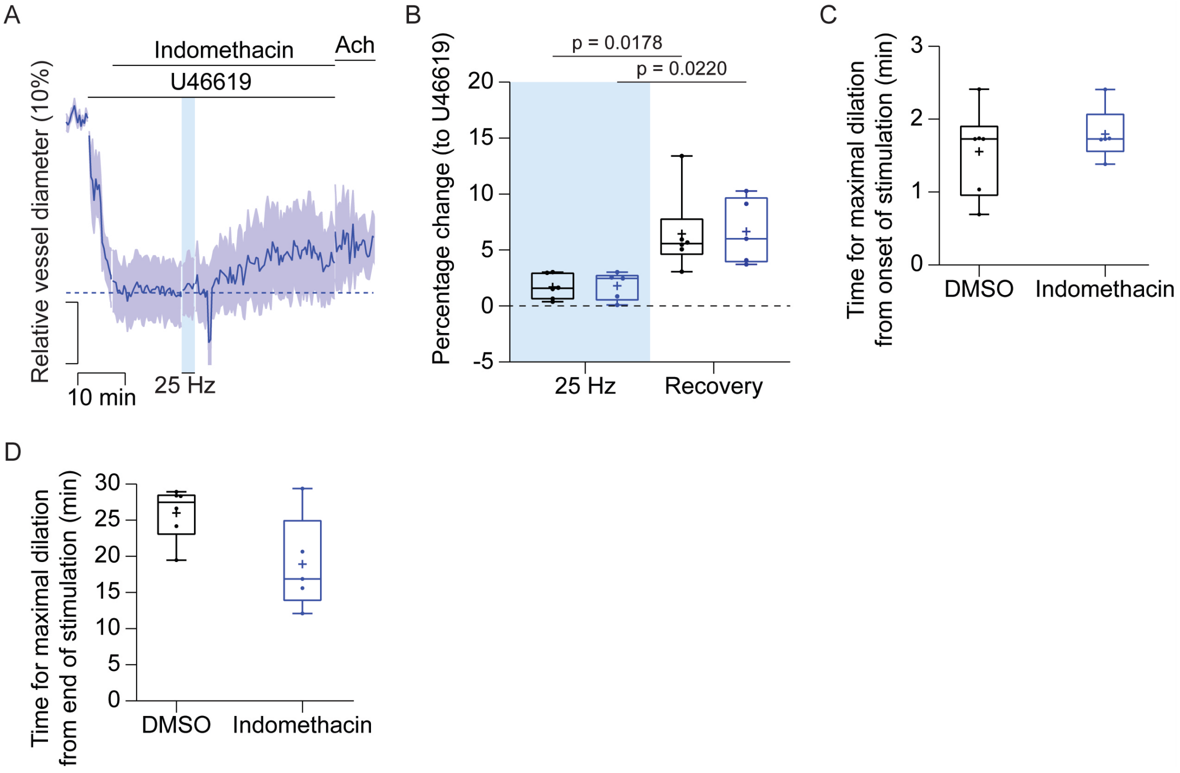

Figure 15: Cyclooxygenases are not involved in NVC in the optic nerve. ***A)*** *Indomethacin was superfused 10 min before the onset of the stimulation and kept for the duration of the recovery period. The dotted line shows the preconstriction level. The blue shaded block shows when the stimulation takes place.* ***B)*** *Quantification of the vessel diameter after stimulation at 25 Hz and recovery for 30 min. DMSO treated nerve dilate 1.70% ± 1.01% after stimulation, meanwhile indomethacin treated vessels dilate 1.79% ± 1.12% (p-value > 0.99 with a Kruskal-Wallis test using 4 pairs for multiple comparisons). After 30 min recovery, the control nerves dilated 6.44% ± 3.25% over the preconstricted levels. The vessels treated with indomethacin dilated 6.64% ± 2.64% over the preconstricted levels (p-value: > 0.99 with a Kruskal-Wallis test using 4 pairs for multiple comparisons). However, the difference between stimulation and recovery does show differences between the treatments. There is an increase of 4.73% between stimulation and recovery with DMSO (p-value = 0.0178 using a Kruskal-Wallis test) and an increase of 4.88% between stimulation and recovery with indomethacin (p-value = 0.0220 using a Kruskal-Wallis test).* ***C)*** *Time needed to reach the maximal dilation during the stimulation period. DMSO treated vessels needed 1.55 min ± 0.55 min to reach the maximal dilation. Indomethacin kept the time to 1.79 min ± 0.33 min (p-value = 0.4634 using a two-tailed unpaired t-test).* ***D)*** *Time needed to reach the maximal dilation after the recovery period. DMSO treated vessels needed 26.00 min ± 3.31 min. Indomethacin decreased the time to 18.92 min ± 5.89 min (p-value = 0.0501, using a two-tailed unpaired t-test).*

These data show that neither one of the two COX enzymes are involved in NVC in the optic nerve. Together with the negative data of the EP_4 receptor inhibitor, I can conclude that the NVC pathway is different in white matter compared to grey matter.

6. WHITE MATTER NEUROVASCULAR COUPLING MECHANISM AT 20% OXYGENATION

However, this comparison does not consider that my experiments were done using 95% oxygen concentration, while the experiments in grey matter were done using 20% oxygen. As mentioned in the Introduction, the oxygen concentration can change the NVC pathway.

Therefore, I decided to test if the EP_4 receptor for prostaglandin E2 is involved in NVC in the white matter at more physiological oxygenation levels, 20% (Gordon et al., 2008). I used the L161,982 inhibitor, as before, but the oxygenation of the aCSF was done using a mixture containing 20% O_2 (Figure 16). To evaluate if the prostaglandin is responsible for the vascular tone at physiological oxygenation, L161,982 was superfused 10 min before the addition of U46619 (Figure 16 A). The quantification of the vessel diameter before the addition of U46619 shows that prostaglandin E2 is not involved in maintaining the vascular tone (Figure 16 B). Interestingly, the quantification of the vessel diameter changes during the stimulation and recovery period (Figure 16 C) demonstrating that the inhibition of the EP_4 receptor blocks the vessel dilation both during the stimulation (DMSO: 1.38% ± 1.02% (n= 5); L161,982: 0.27% ± 2.35% (n=6)) and the recovery period (DMSO: 4.67% ± 3.34%; L161,982: -1.37% ± 4.09%). Although the p-value is not significant for the stimulation (p-value = 0.9698, using a One-way ANOVA with multiple comparisons using 4 pairs), it is significant during the recovery (p-value = 0.0280, using a One-way ANOVA with multiple comparisons using 4 pairs). Although there is no statistical significance between the dilation during the stimulation, it is clear that the inhibitor blocks the vessel dilation in both the stimulation and recovery phases.

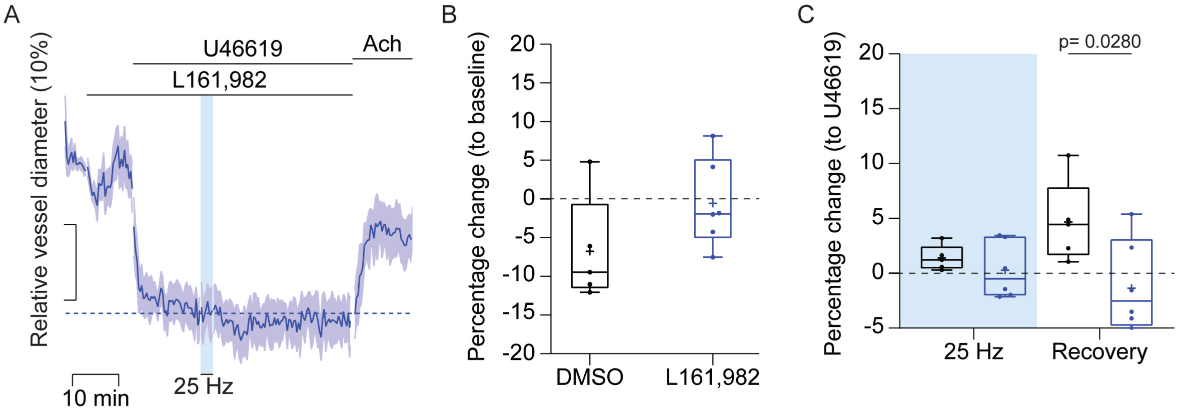

Figure 16: EP_4 receptor at 20% oxygen is involved in NVC in the optic nerve. ***A****) EP_4 receptor inhibitor L161,982 was superfused 10 min before the application of U46619 to evaluate the dependence on prostaglandin E2 of the vascular tone using 20% oxygen and kept for the entire duration of the recovery period. The dotted line shows the preconstriction level. The blue shaded block shows where the stimulation happens.* ***B)*** *Quantification of the vessel diameter after L161,982 shows that the vascular tone is not dependent on prostaglandin E2 (DMSO percentage change to the baseline – 6.75% ± 6.13% (n = 5); L161,982 percentage change to baseline -0.54% ± 5.21% (n = 6). p-value = 0.1355 with a two-tailed unpaired t-test).* ***C)*** *Quantification of the vessel diameter after stimulation at 25 Hz and recovery of 30 min. DMSO treated nerve dilate 1.38% ± 1.02% after stimulation, meanwhile L161,982 treated vessels dilate 0.27% ± 2.35% (p-value = 0.9698 with a one-way ANOVA using 4 pairs for multiple comparisons). After 30 min recovery, the control nerves dilated 4.67% ± 3.34% over the preconstricted levels. The vessels treated with L161982 constricted 1.37% ± 4.09%*

over the preconstricted levels (p-value: = 0.0280 with a one-way ANOVA using 4 pairs for multiple comparisons).

These data show that the prostaglandin E2 receptor, EP_4, is involved in NVC in the *ex vivo* optic nerve at 20% oxygenation. Although more pharmacology is needed, it seems that the NVC pathway in grey and white matter are similar. Additionally, it confirms that NVC pathways of white matter can changed by the oxygen concentration, like in grey matter.

7. NO CHANGE IN VASCULAR ARCHITECTURE IN MICE LACKING OLIGODENDROGLIAL NMDA RECEPTORS

As discussed in the introduction, in the white matter, the axon is wrapped by oligodendrocytes, preventing it from communicating directly with blood vessels. Previous research from the lab has shown that the NMDA receptor located in the myelin of oligodendrocytes is the receptor used by oligodendrocytes to sense axonal activity and thus increase their glycolytic metabolism to support the axonal energetic needs (Saab et al., 2016).

It is conceivable that if this receptor is knocked-out from the oligodendrocytes, the NVC signalling should be altered or completely abolished, in the case of the NVC signalling occurring only via oligodendrocytes. This would mean that oligodendrocytes replace the astrocytes as NVC mediators in the white matter.

To investigate if oligodendroglial NMDA receptors are involved in NVC, I performed experiments using the oligodendrocyte specific NMDA receptor knock-out mouse that additionally expresses eGFP in all perivascular cells (Cnp-Cre +/-; NR1 fl/fl; Pdgfr-β-eGFP + – termed cKO from now on). The control animals to which I compared the cKO, are the same ones used during the previous section of this work (Cnp-Cre +/+; NR1 fl/fl; Pdgfr-β-eGFP + – termed Ctr from now on) (3. Neurovascular coupling in the optic nerve).

As described in (Material and methods 1. Animals) the deletion of the NMDA receptor is linked to the expression of the CNPase enzyme (the Cre recombinase is under the control of the CNPase promoter), which is active from very early stages of development, leading to a deletion of the NMDA receptor in virtually all mature oligodendrocytes.

To compare if there is a difference in NVC in the mutant versus the control mice, I checked first that the general vasculature of the mice is not changed (Figure 17). For this, I used fixed tissue from the cortex and corpus callosum of 6 months old Ctr and cKO mice (Figure 17 A) and counted the number of pericytes (Figure 17 B) and the average vascular length (Figure 17 C). The number of pericytes per mm^2 was not changed between both groups in both grey (Ctr: 183.71 pc/mm^2 ± 29.23 pc/mm^2; cKO: 179.91 pc/mm^2 ± 31.04 pc/mm^2. n Ctr = 5, n cKO= 3; p-value: 0.9980; one-way ANOVA with multiple comparisons using 3 pairs) and white matter (Ctr: 88.77 pc/mm^2 ± 18.95 pc/mm^2; cKO: 97.68 pc/mm^2 ± 21.75 pc/mm^2. n Ctr = 5, n cKO= 3; p-value: 0.9519; one-way ANOVA with multiple comparisons using 3 pairs). This number of pericytes seems to be lower than previously reported (237.5 pc/mm^2 ± 12.4 pc/mm^2 (Hartmann et al., 2015)), although these calculations were done in a different part of the cortex. Most likely this difference probably reflects the difference in the genetic background of the mice (Schaffenrath et al., 2021).

The average vascular length density was also not changed between the genotypes. In the white matter of Ctr mice, it was 0.360 m/mm^3 ± 0.063 m/mm^3 and the cKO have 0.353 m/mm^3 ± 0.098 mm/mm^3 (n Ctr = 5, n cKO= 3; p-value: > 0.9999; one-way ANOVA with multiple comparison using 3 pairs). In the grey matter the control mice have 0.780 m/mm^3 ± 0.058 m/mm^3 and the cKO have 0.793 m/mm^3 ± 0.045 m/mm^3 (n Ctr = 5, n cKO= 3; p-value: 0.9991; one-way ANOVA with multiple comparison using 3 pairs). These values match published values for vascular length density calculated using serial-two-photon microscopy in mice (Ji et al., 2021).

The significant difference between pericyte number and average vascular length between grey and white matter (p-value: < 0.0001; one-way ANOVA with multiple comparisons using 3 pairs) has already been reported (Gross et al., 1986) and it is one of the main vascular differences between the two regions.

In the optic nerve, the pericyte number and inter pericyte distance is also not changed between both genotypes. Due to the heavy myelination of the optic nerve, the staining with classical markers is difficult. It will result in a heavy background due to antibodies getting “stuck” in the myelin membrane. Nevertheless, it is possible to distinguish pericyte somas due to their “bump on a log” morphology (Figure 17 D). Slicing the optic nerve to improve the staining is not desirable because the vasculature is a structure that needs to be studied in a sufficient volume. Thus, I did an immunohistochemistry in the whole optic nerve and evaluated the number of pericytes and the distance between pericytes in both Ctr and cKO animals. The number of pericytes per field of view (425.10 µm x 425.10 µm) in Ctr animals (n= 3) is 6 and for the cKO (n= 4) is 8.25 (p-value = 0.2772 using an unpaired two-tailed t-test) (Figure 17 E). By measuring the distance between pericyte somas, an approximation for changes in capillary density can be made (Kovacs-Oller et al., 2020). In this case, Ctr animals have an inter-pericyte distance of 114.56 µm and the cKO has one of 87.16 µm (p-value = 0.2286 using an unpaired Mann-Whitney test) (Figure 17 F). These distances are considerably larger than the average 50 µm calculated in the cortex of humans or the 72 µm measured in the retina of normal patients (De Oliveira, 1966), which can be a characteristic of the white matter, although more analysis should be done.

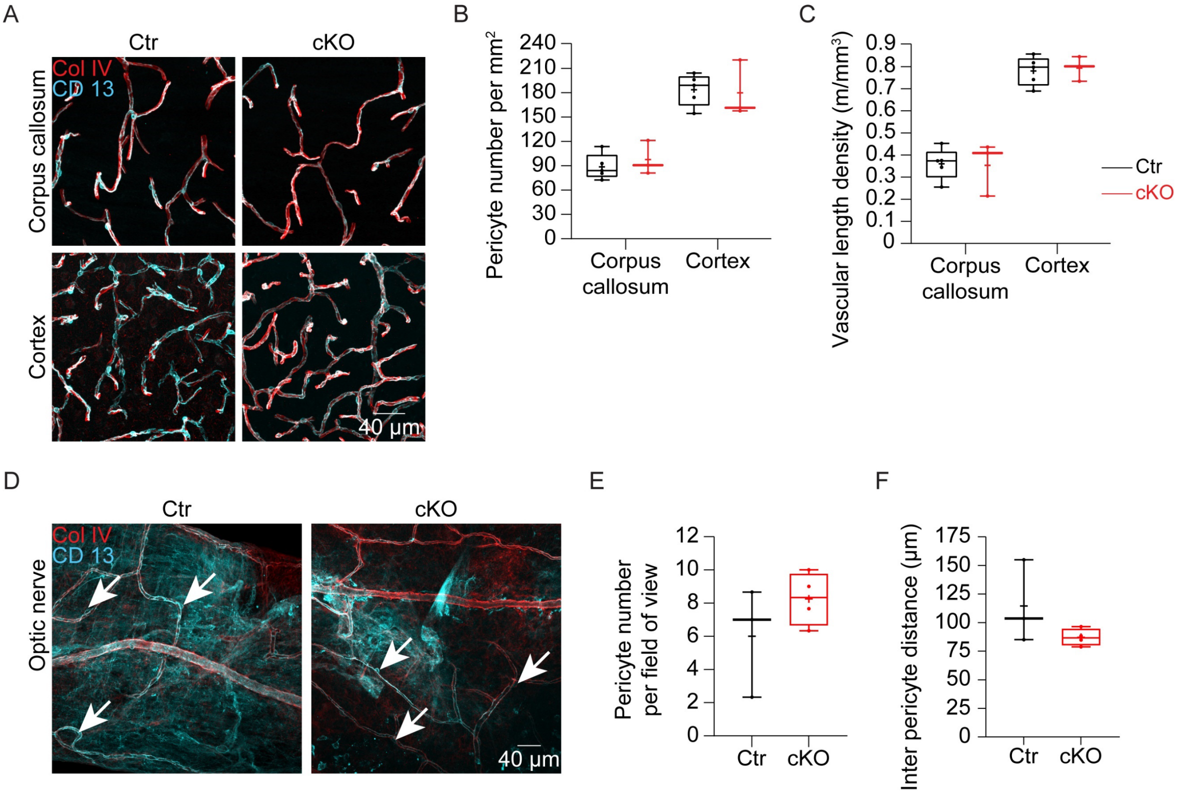

Figure 17: Oligodendroglial NMDA receptor deletion does not affect the CNS vasculature. ***A)*** *Maximum intensity projections of 37.1 µm z-stack taken from 6 months old Ctr and cKO mice. Images were taken from the cortex above the corpus callosum and the middle section of the corpus callosum. CD13 is a marker for pericytes, and Collagen IV is a marker for the basement membrane of blood vessels in which the pericytes are embedded.* ***B)*** *Quantification of pericytes number in 6 months old mice in both the cortex and the corpus callosum. In the corpus callosum of Ctr animals there are 88.77 pc/mm^2 ± 18.95 pc/mm^2, in cKO there are 97.68 pc/mm^2 ± 21.75 pc/mm^2 (n Ctr = 5, n cKO= 3; p-value: 0.9980; one-way ANOVA with multiple comparison using 3 pairs). In the cortex, Ctr mice have 183.71 pc/mm^2 ± 29.23 pc/mm^2 and cKO have 179.91 pc/mm^2 ± 31.04 pc/mm^2 (n Ctr = 5, n cKO= 3; p-value: 0.9519; one-way ANOVA with multiple comparison using 3 pairs).* ***C)*** *Quantification of the average vascular length density in both the cortex and the corpus callosum. In the corpus callosum, Ctr mice show an average vascular length of 0.360 m/mm^3 ± 0.063 m/mm^3 and the cKO have 0.353 m/mm^3 ± 0.098 mm/mm^3 (n Ctr = 5, n cKO= 3; p-value: > 0.9999; One-way ANOVA with multiple comparison using 3 pairs). In the cortex, Ctr animals have 0.780 m/mm^3 ± 0.058 $m/mm^3$and cKO have 0.793 m/mm^3 ± 0.045 m/mm^3 (n Ctr = 5, n cKO= 3; p-value: 0.9991; one-way ANOVA with multiple comparison using 3 pairs).* ***D)*** *Maximum intensity projections of 106.46 µm z-stack taken from 14 weeks old Ctr and cKO mice. Images were taken from the acutely prepared optic nerve. Arrows show pericytes soma used for quantification of pericyte number and inter-pericyte distance.* ***E)*** *Pericyte number calculated on the entire field of view of the microscope 425.10 µm x 425.10 µm x 106.46 µm. Ctr (n= 3) has on average 6 pericytes in that field of view and the cKO (n= 4) animals have 8.25 (p-value = 0.2772 using an unpaired two-tailed t-test).* ***F)*** *The inter-pericyte distance of Ctr animals is 114.56 µm and the cKO is 87.16 µm (p-value = 0.2286 using an unpaired Mann-Whitney test).*

The deletion of the NMDA receptor from oligodendrocytes reduces their glucose uptake and reduces the energetic support of the axonal activity (Saab et al., 2016). A possible cause, besides the decrease in Glut1 receptor mobilization to the membrane (Saab et al., 2016), is that the vessel size in the white matter of these animals is decreased. For this, I tested the diameter of the vessels in previous experiments in a *post-hoc* manner (Figure 18). These measurements correspond to the average diameter during the first 2 min of the experiment, before the nerve is bathed with U46619. There is no difference in the Full-Width Half Maximum of the vessels between the two groups (Ctr: 4.22 µm ± 0.87 µm; cKO: 4.32 µm ± 0.93 µm; n Ctr = 28 and n cKO = 34; p-value: 0.9384 using a Mann-Whitney two-tailed test). Thus, the decrease in oligodendroglial glucose metabolism is only due to the reduction in membrane Glut1 transporters caused by the NR1 deletion and not by changes in vessel diameter.

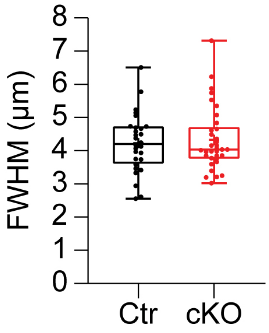

Figure 18: Vessel diameter is not changed in ex vivo optic nerves after oligodendroglial NMDA receptors deletion. After having a viable response using a preconstrictor (U46619) and a dilator (acetylcholine), the diameter of vessels (having ensheathing or mesh pericytes) was calculated according to the Gaussian fit in their fluorescence profile during the baseline using the Full-Width Half Maximum of the fitted curve.

Although a better quantification of pericyte numbers is needed for the optic nerve, these data suggest that there is no difference in the general architecture of the vasculature caused by the deletion of NMDA receptors in oligodendrocytes.

8. OLIGODENDROGLIAL NMDA RECEPTORS ARE INVOLVED IN NVC IN THE OPTIC NERVE

Although the vessel size of the cKO is not changed compared to Ctr animals, it is possible that the decrease in glucose uptake by oligodendrocytes (Saab et al., 2016) is due to changes in contractile properties of the vessels. Next, I evaluated if the contractile properties of the vessels are changed compared to the Ctr animals (Figure 19). I checked the contractile properties of the vessels by applying the constrictor U46619 (100 nM) for 15 min followed by ACh (100 µM) for 15 min (Figure 19 A). Ctr animals (n= 4) constricted 20.38% ± 3.53% (Figure 7) and cKO (n= 4) constricted 20.20% ± 7.15% (p-value = 0.9702 using an unpaired two-tailed t-test) (Figure 19 B). After 15 min of ACh (Figure 19 C), the cKO animals dilated 14.50% ± 6.76% over the preconstricted level. The Ctr animals dilated 15.33% ± 2.80% (p-value = 0.8499 using an unpaired two-tailed t-test).

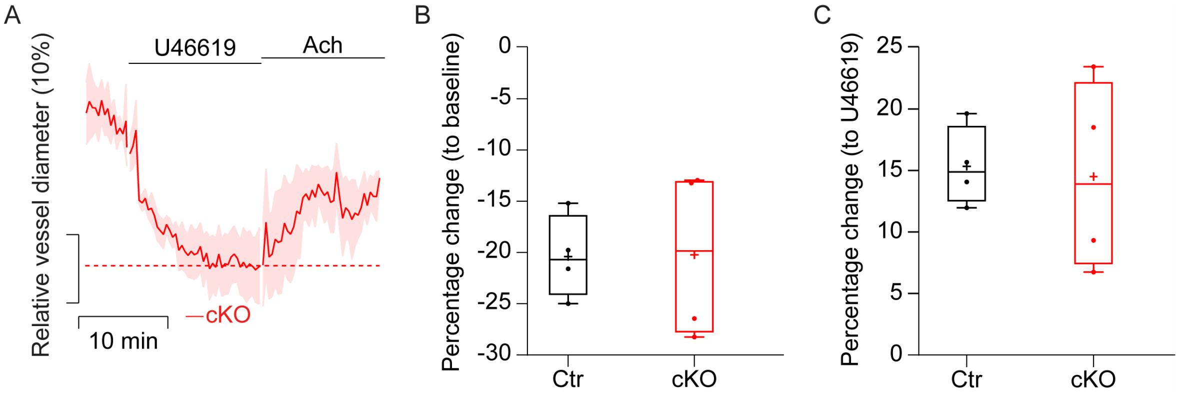

Figure 19: Oligodendroglial NMDA receptor knockout does not change the contractile properties of the perivascular cells. ***A)*** *Optic nerves were bathed with the constrictor U46619 (100 nM) for 15 min followed by 15 min of acetylcholine (100 µM). The dotted line shows the vessel size at the end of the preconstriction.* ***B)*** *Quantification of the last 2 min of preconstriction for both groups. Ctr animals constricted 20.38% ± 3.53%. cKO animals constricted 20.20% ± 7.15% over the baseline level (p-value: 0.9702 using an unpaired two-tailed t-test).* ***C)*** *Quantification of 2 min at the maximal dilation during acetylcholine treatment for both groups. Ctr animals dilated 15.33% ± 2.80% over the preconstricted level. cKO animals dilated 14.50% ± 6.76% over the preconstricted levels (p-value = 0.8499 using an unpaired two-tailed t-test).*

Because there is no difference in the contractile properties of the cKO animals compared to Ctr animals, it is possible to use this technique to evaluate if the neurovascular response is different in the mutant animals. This allows me to evaluate if oligodendrocytes play a role in white matter NVC via the NMDA receptor.

The deletion of NMDA receptors from oligodendrocytes induces a decrease in the action potential conduction only at high frequencies in the spinal cord axons (Saab et al., 2016). To evaluate if the NVC was affected in the same way in the optic nerve, I replicated the previous experiments (Figure 8) using the NMDA receptor knockout mice (Figure 20).

A comparable reduction of the dilation of the vessels for all three frequencies used can be observed. There was a decrease in vessel size of 1.12% (Figure 20 A and D), 1.71% (Figure 20 B and D), and 1.05% (Figure 20 C and D) compared to Ctr mice for 4 Hz, 25 Hz, and 100 Hz, respectively (Figure 8 D). After 30 min recovery, cKO animals show a lower dilation compared to Ctr animals, for 4 Hz there was a decrease of 3.93%, for 25 Hz it was 4.19%, and for 100 Hz the difference was 4.44% (Figure 20 and Figure 8).

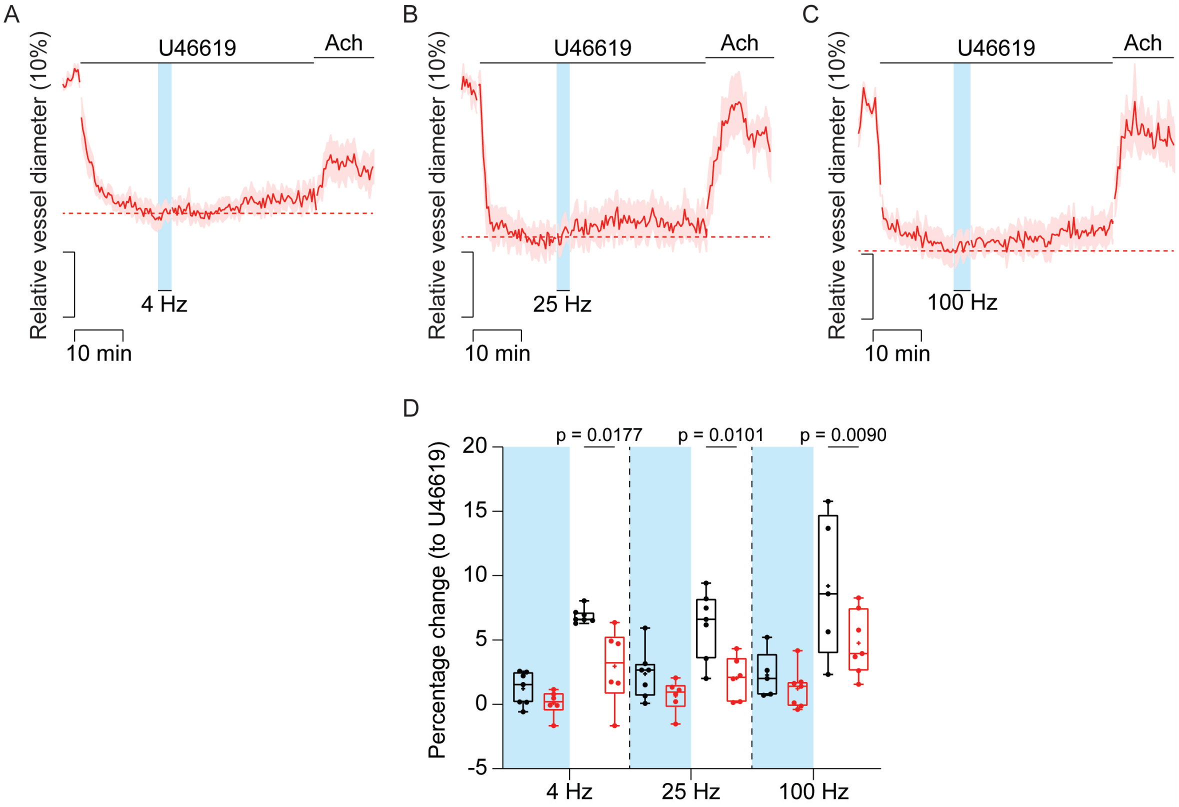

Figure 20: Oligodendroglial NMDA receptors are involved in white matter NVC. ***A)*** *Optic nerves from cKO mice were preconstricted with U46619 (100 nM) and stimulated at 4 Hz (n= 6),* ***B)*** *25 Hz (n= 6), and* ***C)*** *100 Hz (n= 7) for 3 min followed by a recovery period of 30 min. The experiment was terminated after the application of acetylcholine 100 µM for 15 min (n= 6). The dotted line shows the preconstriction level. The blue shaded block shows the stimulation period.* ***D)*** *Quantification of the dilation percentage of the vessels during the stimulation (blue shaded block) and during the recovery period (white block, next to the blue shaded block) for each frequency of stimulation. Ctr animals are the same as shown in Figure 8. Vessels of nerves stimulated at 4 Hz dilate 1.23% ± 1.19% for Ctr and 0.10% ± 0.90% for cKO mice during the stimulation (p-value = 0.9430; using a one-way ANOVA using 6 pairs for multiple comparisons) and 6.88% ± 0.54% and 2.95% ± 2.67% during the recovery period for Ctr and cKO mice, respectively (p-value: 0.0177; using a one-way ANOVA using 6 pairs for multiple comparisons). Ctr nerves stimulated at 25 Hz dilate 2.38% ± 1.78% during the stimulation, cKO nerves dilated 0.66% ± 1.12% (p-value = 0.6988; using a one-way ANOVA using 6 pairs for multiple comparisons). During the recovery, Ctr nerves dilated 6.23% ± 2.41%, and mutant nerves dilated 2.04% ± 1.52% (p-value = 0.0101, using a one-way ANOVA using 6 pairs for multiple comparisons). During the 100 Hz stimulation, Ctr nerves dilate 2.27% ± 1.64% and cKO mice 1.22% ± 1.45% (p-value = 0.9673; using a one-way ANOVA using 6 pairs for multiple comparisons). During the recovery of 100 Hz, Ctr mice had a dilation of 9.20% ± 4.97%, meanwhile, cKO nerves had a dilation of 4.76% ± 2.31% (p-value = 0.0090; using a one-way ANOVA using 6 pairs for multiple comparisons).*

Interestingly, the time needed to reach the maximal dilation in each case was not different in the mutants compared to the control animals (Figure 21).

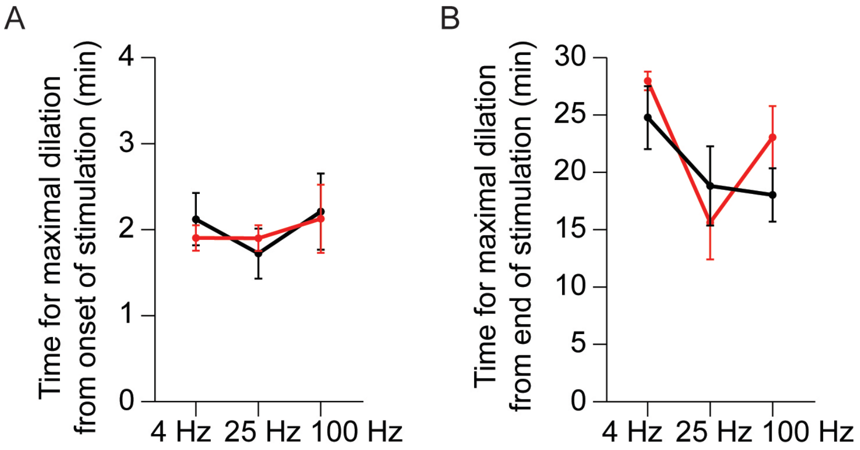

Figure 21: Oligodendroglial NMDA receptor deletion does not affect NVC kinetics. ***A)*** *The time needed to reach the maximal dilation during the stimulation at three different frequencies between Ctr and cKO mice. Ctr animals needed 2.12 min ± 0.74 min to reach the maximal dilation during stimulation, while the cKO mice needed 1.90 min ± 0.33 min (p-value > 0.99 using a Kruskal-Wallis test with 3 pairs multiple comparisons) during the 4 Hz stimulation. During 25 Hz stimulation, Ctr mice reached the maximal dilation at 1.72 min ± 0.71 min, and cKO did at 1.90 min ± 0.33 min (p-value > 0.99 using a Kruskal-Wallis test with 3 pairs multiple comparisons). At 100 Hz stimulation, Ctr mice needed 2.21 min ± 0.88 min and cKO 2.12 min ± 0.97 min (p-value > 0.99 using a Kruskal-Wallis test with 3 pairs multiple comparisons).* ***B)*** *The time to reach the maximal dilation during the recovery period does not change with the deletion of NMDA receptors in oligodendrocytes. After 4 Hz stimulation Ctr mice reached the maximal dilation at 24.78 min ± 6.71 min and cKO at 27.99 min ± 1.81 min (p-value > 0.99 using a Kruskal-Wallis test with 3 pairs multiple comparisons). After 25 Hz stimulation Ctr mice dilated maximally at 18.89 min ± 8.48 min and cKO did at 15.63 min ± 7.19 min (p-value > 0.99 using a Kruskal-Wallis test with 3 pairs multiple comparisons). During the recovery after 100 Hz, Ctr nerves reached a maximal dilation at 18.03 min ± 4.64 min and cKO at 23.07 min ± 6.65 min (p-value =0.5589 using a Kruskal-Wallis test with 3 pairs multiple comparisons).*

The NVC in cKO animals exhibits the same speed as in controls, however, it does not dilate to the same levels, suggesting possible complementary pathways in the white matter that do not rely on oligodendroglial NMDA receptors.

To assess if the axonal conduction was impaired at high frequencies in the optic nerve, thus causing the impaired NVC seen above, I compared the waveforms of the CAP of the nerves that were stimulated at 25 Hz and 100 Hz (Figure 22). The waveforms of each nerve differed from one another. The waveform depends on several variables, including how good the nerve fits inside both suction electrodes and how long the nerve is. To compare them, it was necessary to normalize each waveform to the maximum and minimum of the waveform of the baseline. This means that at the baseline levels (Figure 22 A and D), the waveform will reach a maximum and during the stimulation (Figure 22 B and E) or recovery (Figure 22 C and F), the waveforms will be compared to that maximum. This will make it possible to compare in a qualitative way how much the NMDA receptor mutation will affect the axon conduction compared to the control animals.

During the stimulation at both 25 Hz and 100 Hz, there is a reduction in the height of the waveform in the two groups (Figure 22 B and E). This means there is a reduction in the action potential conduction, but it seems not to be more pronounced in the cKO animals. Interestingly, after just 5 min of the recovery, both waveforms are overlapping again (Figure 22 C and F). This deviates from the axonal conduction properties of the spinal cord which are only affected at high frequencies, such as 100 Hz (Saab et al., 2016). As there seems to not be any differences in axonal conduction, I conclude that the impaired NVC is not caused by axonal conduction defects of the mutant.

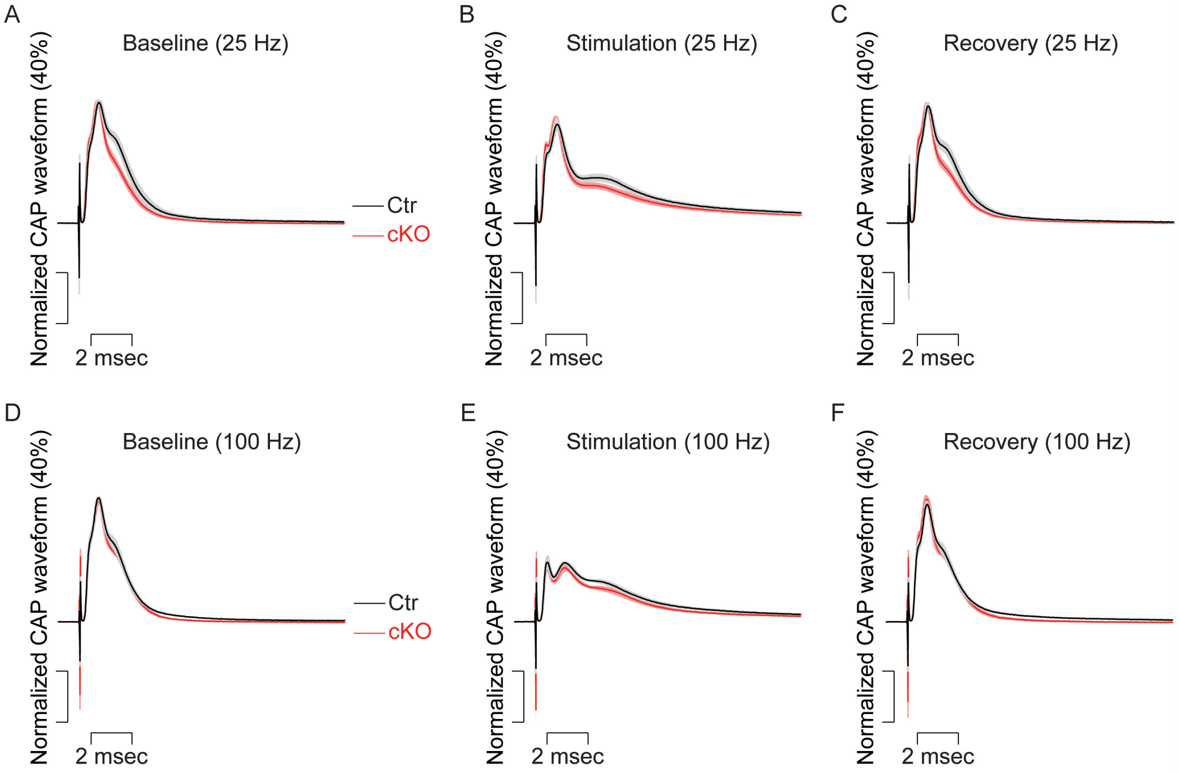

Figure 22: Axon conduction is not impaired in mutant animals. ***A)*** *Waveform of the CAP recorded during the baseline before 25 Hz stimulation.* ***B)*** *Waveform of the CAP recorded at the end of the 25 Hz stimulation.* ***C)*** *Waveform of the CAP recorded after 5 min of recovery after the 25 Hz stimulation.* ***D)*** *Waveform of the CAP recorded during the baseline before 100 Hz stimulation.* ***E)*** *Waveform of the CAP recorded at the end of the 100 Hz stimulation.* ***F)*** *Waveform of the CAP recorded after 5 min of recovery after the 100 Hz stimulation.*

9. POTASSIUM BUFFERING IS NOT AFFECTED BY NMDA MUTATION

One additional information that we can derive from the previous data is related to potassium buffering in the optic nerve and its involvement in NVC. The quantification of the CAP reflects changes in the repolarization of certain axons. By calculating the area under the waveform of the CAP (Figure 23), we can compare if the repolarization speed of the axons is slower in the mutants than in the controls. Again, the data is shown only for 25 Hz and 100 Hz experiments. At the end of the stimulation at 25 Hz (Figure 23 A), the area of the CAP of the mutant nerves decreased 11.25% from baseline, compared to controls that decreased 16.73% (p-value= 0.0956 using a two-tailed unpaired t-test). However, the recovery after the stimulation is indicative of the potassium buffering. After 5 min of recovery, both curves are overlapping, meaning that there is no difference in the hyperpolarization of the fibres, thus, the potassium buffering is not changed. The exact thing is also happening after 100 Hz stimulation (Figure 23 B), there is a comparable decrease in firing axons (Ctr: 48.78%; cKO: 51.68%; p-value= 0.4206 using a Mann-Whitney test) but the hyperpolarization has the same kinetics. In this case, the cKO animals even have a better recovery of the firing properties than the Ctr mice. The wavy pattern of the CAP in this figure is due to the oscillatory changes in temperature in the chamber during the recordings. These data show that potassium buffering is not related to the impairment of the NVC in the mutant animals, as it is not affected.

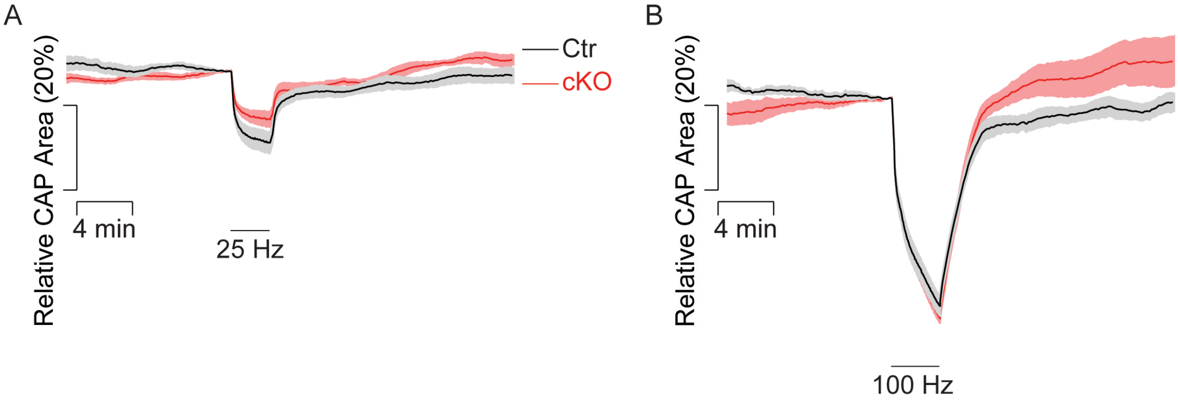

Figure 23: Potassium buffering in the optic nerve is not affected by oligodendroglial NMDA receptor deletion. ***A)*** *Quantification of the area under the curve of the waveform along the time shown in Figure 22. It is marked when the 25 Hz stimulation takes place for both Ctr and cKO mice.* ***B)*** *Quantification of the area under the curve of the waveform along the time shown in Figure 22. It is marked when the 100 Hz stimulation takes place for both Ctr and cKO mice.*

In conclusion, the oligodendroglial NMDA receptor is partially involved in the optic nerve's NVC by an unknown mechanism that seems not to be related to the potassium buffering capacity of glial cells.

10. *IN* VIVO WHITE MATTER BOLD IN THE HUMAN BRAIN

The study of NVC *ex vivo* has several drawbacks (3.5 Methods to study NVC). The most important one is that the main function of the vasculature is eliminated. The availability of glucose and oxygen instead of being limited to the transport via vessels comes from outside the tissue. Nevertheless, the *ex vivo* experiments are useful to study the mechanisms that are involved in NVC (Grutzendler and Nedergaard, 2019). For cortical NVC studies, *in vivo* experiments have been a great resource and can be considered as the standard technique for this field of research. Despite the improvement in reaching a more physiological condition, *in vivo* experiments have some drawbacks (3.5 Methods to study NVC). If anaesthesia is used, the brain connectivity is probably changed (van Alst et al., 2019; Xie et al., 2019), resulting in different NVC mechanisms and responses. If awake mice are used, careful control of the preparation is necessary to avoid artefacts or contradictory data due to changes in temperature at the observed site (Roche et al., 2019).

In humans, these caveats can be minimized by using functional Magnetic Resonance Imaging (fMRI). fMRI allows for unrestricted access to the entire brain vasculature without the need for anaesthesia, and the callosal fibres can be activated by performing certain tasks (Tettamanti et al., 2002; Weber et al., 2005). As mentioned in the introduction (4.2

Evidence for white matter BOLD signal), white matter blood oxygenation level-dependent (BOLD) activation has been debatable. Just a few studies are being published about this topic (Courtemanche et al., 2018; Fraser et al., 2012; Gawryluk et al., 2014; Li et al., 2021). The analysis pipelines that are developed for fMRI are for grey matter BOLD signals, where the hemodynamic response function (HRF) is known. In white matter, the HRF may be different (Guo et al., 2022; Li et al., 2021), which has to be taken into account in the analysis of white matter BOLD activation.

The *ex vivo* data shown above, suggests a delayed and sustained dilation after a short period of axonal activity in a white matter tract. To try to replicate those findings *in vivo*, I collaborated closely with Dr. Renate Schweizer (Functional Imaging Laboratory – German Primate Center) to study human white matter BOLD activation upon a task-based followed by a resting-state fMRI. As this is very preliminary and has not been done before, fMRI measurements were only performed on one subject, the author of this thesis.

To induce white matter activation, an interhemispheric task was used. One of the most common tasks for interhemispheric activation is the Poffenberger task (Marzi, 1999). In this task a button is pressed with the index finger of one hand upon a visual stimulus in either the right or the left hemifield. This combination triggers both interhemispheric and intrahemispheric activations. The interhemispheric activation activates fibres that cross hemispheres via the commissures, which are white matter tracts that communicate both hemispheres. Naturally the corpus callosum is one of them. Published research has shown BOLD activation in white matter using such tasks (Gawryluk et al., 2014), however, they have been analysed using grey matter parameters (Mazerolle et al., 2008), which poses a problem.

Typically, the BOLD response in grey matter ranges between 2% and 4% (Hillman, 2014), meaning that the increase in oxygenation measured is only 2% higher than during baseline. *Ex vivo* data has shown that vessel diameter in grey matter increases ~15% during neuronal stimulation (Mishra et al., 2016), and *in vivo* data shows ~8% dilations (Rungta et al., 2021). If we consider that the BOLD effect is caused by post-synaptic potentials, which are not existent in white matter, we should expect a BOLD activation lower than 1% in white matter. Considering the results shown above, with the optic nerve, the dilation of the vessels upon maximal physiological stimulus is only ~4%. This would mean that we should expect a BOLD activation in the white matter much lower than 1%, however, the maximal dilation of the white matter is reach ~20 min after the end of the stimulation. If the BOLD signal is measured after the stimulation is over, instead than during the stimulation, it is possible that a bigger BOLD signal can be detected.

Following that rationale, and the data shown above, the fMRI measurements consisted of a task-based fMRI of 6.20 min immediately followed by a resting-state fMRI of 30 min. The Poffenberger task was used during the task-based fMRI. As a form of control, the subject was exposed to only resting-state fMRI measurements, without any task. This control will reveal if the white matter activation is caused by the previous task or not. For this thesis, only the resting-state period of the fMRI measurements were analysed (Figure 21).

Because there is no described HRF model for this specific white matter activation, and it is very difficult to know what to expect, a model-free analysis was performed using

Independent Component Analysis (ICA). The ICA showed, as expected, components with grey matter activation during the resting-state, independent of a task being present before the resting-state (Figure 21 A upper). These grey matter activations are associated with the ongoing activation and deactivation of the various networks of the brain occurring during resting-state fMRI (Pariyadath et al., 2014). Only two examples are shown. The shown components represent the primary visual network (Zhang et al., 2015) (Figure 21 A left) and the left central executive network (Doll et al., 2015) (Figure 21 A right). The voxels that make a component, in this case the red-yellow voxel shown in the spatial map, are grouped together based on exhibiting the same time-series profile (Figure 21 A bottom). The two components have time series typical of grey matter BOLD showing lower frequencies indicating the 'on–off' fluctuation of the network. Both the activation maps and the time courses of these resting state network components serve as controls, indicating that the resting state fMRI measurements with and without task resulted in the regular and expected grey matter related resting-state results, validating the measurements.

During normal grey matter BOLD signal analysis, only grey matter activation components are selected to clean up the data and reduce the number of components. In the present case, the analysis was done the opposite way, only components with white matter activation were selected and the data set was then denoised using these components to reduce grey matter activation. As the task performed here, a variation of the Poffenberger paradigm (Tettamanti et al., 2002; Weber et al., 2005), activates visual and motor fibres that cross between brain hemispheres through regions II and III of the corpus callosum (Wahl et al., 2007), it would be expected to observe ICA components with spatial maps showing white matter activation in that area. Fittingly this was visible only in the measurements when the Poffenberger task was performed before the resting-state (Figure 21 B top, right). The spatial map of the component shows a large circumscribe BOLD-activation limited to the corpus callosum. When there was no task, no components with activation of the corpus callosum was observed. Even if white matter activation was present, it remained very small and very scattered (Figure 21 B top left). The drawback of the observed components exhibiting BOLD activation specifically in the corpus callosum indicating activation of the white matter vasculature, is the unexpectedly high frequency of the associated time series which is usually identified as classical noise pattern (Figure 21 B bottom).

This indicates that the long latency of the NCV detected in the *ex vivo* experiments at the optical nerve were not instrumental in the explorative detection of white matter BOLD activation. Also, although these experiments were repeated 4 times, in the same subject, the white matter activation was only visible in 3 out of the 4 measurements. Therefore, additional in-depth analysis of the present data, adaptation of existing tools for white matter and further measurements are needed to not only improve the detection of the white matter BOLD activation but to potentially specify white matter activation based on different latencies and time courses.

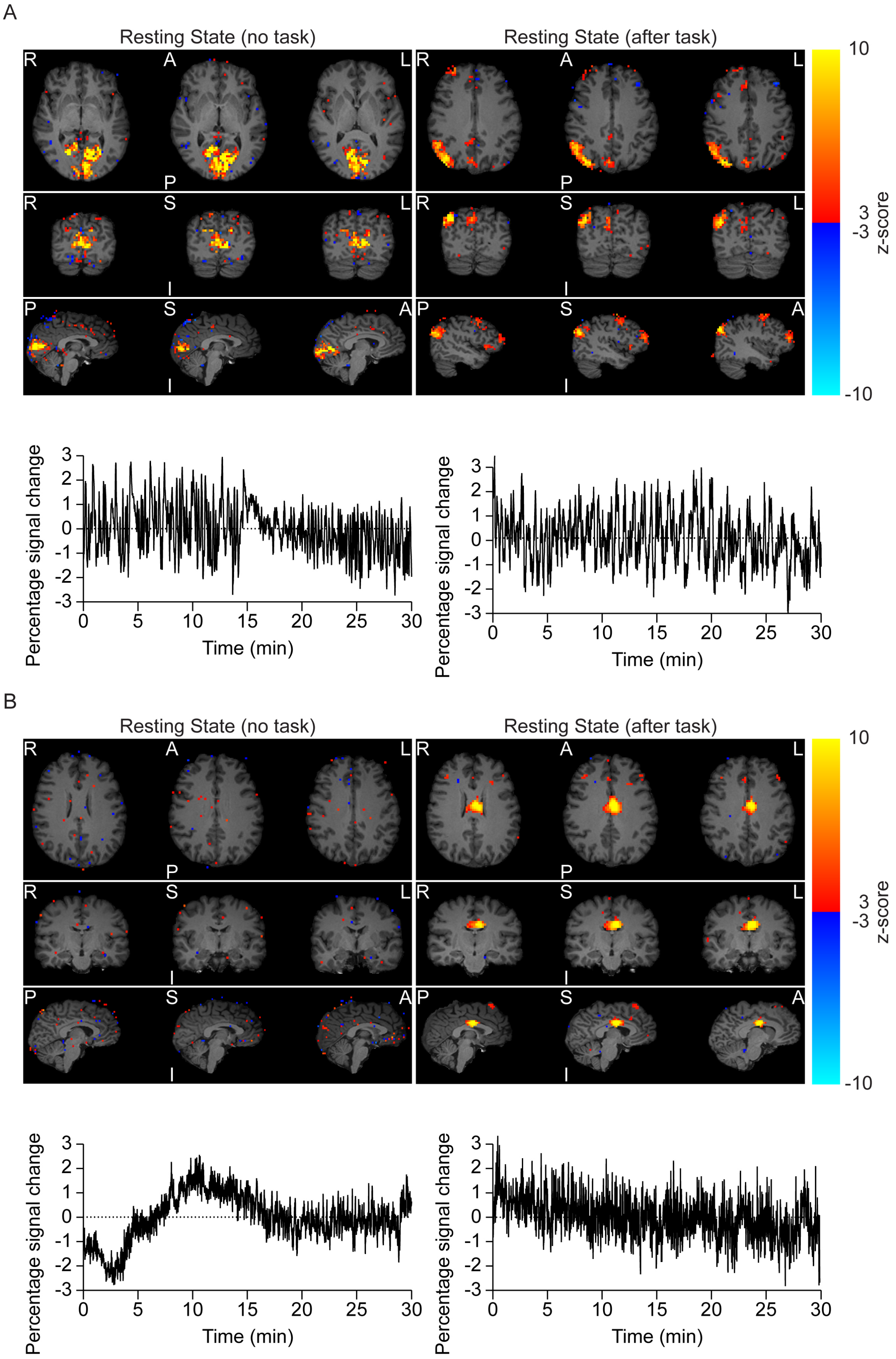
A
Resting State (no task)
Resting State (after task)
R
A
L
P
S
I
10
3
-3
z-score
-10
Percentage signal change
3
2
1
0
-1
-2
-3
0
5
10
15
20
25
30
Time (min)
B
Resting State (no task)
Resting State (after task)

Figure 24: BOLD signal in the white matter after the Poffenberger paradigm. ***A)*** *The upper part shows the spatial map of activation during the resting-state phase of the experiment. The spatial map on the left (control) represents the measurements in the absence of a Poffenberger task. This represents the control of these experiments. The spatial map on the right shows the resting-state phase of the measurements after a Poffenberger task was done. L: left side; R: right side; A: anterior; P: posterior; S: superior; I: inferior. Warm colours indicate a positive correlation, cold colours represent a negative correlation. The bottom part shows the time series curves of the two components, left: resting-state without previous task; right: resting-state after the previous task. The shape of the curve is characteristic of the grey matter BOLD signal. The colour scale represents the z-statistic values.* ***B)*** *Upper part: cleaned data after selecting for white matter components. The spatial map shows that only upon a task (right) there is white matter activation. The control measurement (left, no task) shows no white matter activation. Bottom part: time series curves of the two components after cleaning the data. The colour scale represents the z-statistic values.*

DISCUSSION

The brain has very little energy storage. The neuron, the basic unit of the CNS, needs the support of glial cells to produce ATP. Neuronal activity is coupled to glial metabolism (neurometabolic coupling – NMC) and the vascular system (neurovascular coupling – NVC). With increasing neuronal activity, astrocytic and oligodendroglial metabolism increases to produce more pyruvate or lactate that the neuron uses to produce ATP. At the same time, blood vessels dilate to increase the availability of both glucose and oxygen, necessary for ATP production.

The grey matter is the most energetically demanding region of the brain, the cortex alone uses 27.2 to 40.7 µmol ATP/g/min (Howarth et al., 2012). Meanwhile, the entire brain consumes on average 21 µmol ATP/g/min (Attwell and Laughlin, 2001). Out of all the different cellular processes taking place in the grey matter, neuronal communication is the most energy-consuming one (Howarth et al., 2012; Yu et al., 2018).

Although the models for NMC in grey matter were first postulated in 1985 (Kadekaro et al., 1985) and the first experimental evidence was published in 1994 (Pellerin and Magistretti, 1994), it took longer for the first mechanism of NVC to be published. In 2003 the first evidence that astrocytes sense synaptic glutamate and communicate to the vasculature to induce dilation was shown (Zonta et al., 2003). Nowadays, at least 12 different enzymes/receptors/molecules have been shown to modulate the NVC in grey matter in one way or another.

The idea of NMC in white matter was postulated in 2010 (Nave, 2010), 16 years later than for grey matter, and the first experimental evidence followed two years later (Fünfschilling et al., 2012). For NVC the lag is even longer. There are only a handful of papers about white matter BOLD activation (Gawryluk et al., 2014) but there are no papers about white matter NVC mechanisms. This study is the first time that NVC is studied in a white matter *ex vivo* tissue. By using the optic nerve as a model tissue, I showed that axons communicate their energetic needs to the vasculature, presumably by an already proposed pathway of NVC (Mishra et al., 2016). Additionally, I showed that oligodendroglial NMDA receptors seem to modulate the response, albeit this mechanism remains to be elucidated. This supports the model for NMC of white matter.

The optic nerve is an ideal tissue to study different metabolic mechanisms of the white matter (Asadollahi et al., 2022; Brown et al., 2003; Saab et al., 2016; Trevisiol et al., 2017). Nevertheless, the vasculature of the nerve has not been fully described. Two remarkable things can be appreciated (Figure 4). The first one is the size difference between the artery/arteriole and the vein that runs along the entire nerve. The second is that there seems to be only one artery/arteriole in each nerve, although this should not be surprising. In the cortex, in a column of 420 µm x 420 µm x 400 µm, there are only two ascending venules and two penetrating arterioles (Sweeney et al., 2018). On average, the optic nerve is ~200 µm thick, thus having only one big vein and one artery/arteriole is to be expected.

Following the pericyte nomenclature proposed by Andy Shih's group (Grant et al., 2019), I identified ensheathing pericytes, mesh pericytes, and thin-stranded pericytes based on their morphology. By using two very common vasoactive molecules, I demonstrated that the contractile properties of the perivascular cells are retained after the acute preparation of the optic nerve. Only ensheathing and mesh pericytes respond with a constriction and dilation to U46619 and ACh respectively (Figure 6 and Figure 7). U46619 is a thromboxane A2 analogue that binds to the TP receptor and induces an increase in calcium in the perivascular cell that will lead to constriction of the vessel (Glück et al., 2021; Mishra et al., 2016). ACh is a vasodilator that upon binding to its receptor, induces NO production that induces relaxation of the perivascular cell (Manicam et al., 2016; Yamada et al., 2001). Although mesh pericytes in the grey matter have been reported not to express α smooth muscle actin (Grant et al., 2019), and thus do not have contractile properties, my functional experiments show that in the white matter they can regulate vessel diameter.

The detection of α smooth muscle actin in pericytes is dependent on the tissue preparation (Alarcon-Martinez et al., 2018). It is therefore possible that the evidence suggesting no contractile properties in mesh pericytes was due to the tissue processing. Currently, we lack *in vivo* data to confirm that mesh pericytes do not regulate blood vessel diameter. In the grey matter, these perivascular cells are also located after capillaries towards the venules and veins side of the vascular tree (Hartmann et al., 2015), which are widely accepted not to have contractile functions. In the optic nerve, the venules and veins are not far apart from each other, making their identification very easy. Additionally, the morphology of the venous perivascular cells is also very different from the morphology of mesh pericytes (Figure 5 and Figure 6).

The NVC hypothesis predicts that upon increased neuronal activity, the blood vessel diameter will increase, while in absence of neuronal activity, the vessel size should go back to baseline levels. Interestingly, in the optic nerve, pre-capillary arterioles dilate during the stimulation, either with 4 Hz, 25 Hz, or 100 Hz, but the vessels keep dilating during the next 25 min (Figure 8 and Figure 9). This time frame correlates with the 30 min necessary for GLUT1 mobilization to the membrane upon glutamate exposure (Saab et al., 2016). In grey matter the increase in cerebral blood flow is dependent on stimulation frequency (Enager et al., 2009). In the optic nerve, this seems not to be true. There is an increase in vessel dilation between 4 Hz and 25 Hz but there is no effect between 25 Hz and 100 Hz, possibly indicating that after 25 Hz the response will reach a maximal electrically evoked dilation. More experiments are needed to confirm this. The stimulation-evoked dilation (Figure 10 and Figure 11) level that is reached at the end of the recovery period is the same for all three frequencies. This would suggest that this is an all or none response because low frequencies have the same effect as very high frequencies (Figure 8). More experiments using lower stimulation frequencies are needed to have a strong conclusion on this matter.

The data also shows that with increased stimulation frequency, there is an increase in the variability of the response. The physiological firing range of the retinal ganglion cells ranges between 0.1 Hz and ~30 Hz, with 4 Hz as the frequency at which the majority of axons fire (Perge et al., 2009). At 25 Hz and 100 Hz, some axons will not be able to repolarize as fast as the stimulation which will cause conduction blocks in those fibres. This explains the increased variability because the axons that stop firing, cannot communicate with the vessels, thus they stop dilating while other axons will continue to fire and thus the vessel dilation will continue. By using ACh as a positive control at the end of the experiment I rule out that the prolonged dilation is an artefact caused by the cells dying over time, or by losing their contractile properties. As mentioned before, for the ACh response to be possible, both the endothelial and perivascular cells need to be functional.

The delayed and sustained dilation can be due to a summation of dilating signals that remain after the electrical stimulation is over. If the optic nerve is stimulated for different periods of time, the vessel dilates over the first 70 min, after which it decays, even if the stimulations continues (Figure 13). This suggests that 70 min might be enough time for the vasculature to accomplish its role, either by replenishing glycogen stores used during the first stimulation or by giving enough oxygen to the entire optic nerve to support the ATP production. However, as the *ex vivo* experiments remove these functions from the vasculature, this may be an artefact of this experiment in particular. Nevertheless, I think that the most probable reason is that after 70 min there is a saturation of vasodilating signalling.

In the optic nerve, astrocytes and oligodendrocytes are connected via gap junctions thus forming a big syncytium. The gap junctions between oligodendrocytes and astrocytes are heterotypic, formed by the pairs of connexins (Cx) Cx32/Cx30 or Cx46/Cx43 (Köhler et al., 2019; Lundgaard et al., 2014; Orthmann-Murphy et al., 2008). This huge pan glial syncytium has been shown to promote metabolite movement from one optic nerve to the other in a matter of days (Cooper et al., 2020). It is perfectly conceivable that vasodilatory signals remain in the pan glial syncytium after the end of the stimulation, or that they stay in the vascular syncytium (Longden and Nelson, 2016) causing the observed prolonged dilation, although this type of signalling is generally fast (Longden et al., 2021). According to (Hariharan et al., 2022) the electrical signal that travels through the endothelial syncytium at a speed of 0.2 cm/sec. In their experiments, the signal took 10 sec to travel 270 µm (Hariharan et al., 2022). The mouse's optic nerve is approximately 5 mm long, thus it would take 175 sec (~3 min) for the signal to travel from the most rostral pericyte to the pre-capillary arteriole, located on a caudal position (Figure 4).

Extrapolating from the model for the grey matter, it is possible that all astrocytes are signalling to the vasculature at the same time. Since the vascular system supports the entire optic nerve, the vasodilatory signal coming from different parts of the nerve prevents vessels from returning to the baseline levels. This could potentially be tested by performing the optic nerve NVC experiments in mice lacking the coupling between oligodendrocytes and astrocytes or between astrocytes.

As mentioned in the introduction, a caveat of the *ex vivo* work is that the tissue is normally in a hyperoxic environment. The effect of oxygen as a modulator of the NVC response was disregarded from the beginning (2003) until 2008 when it was shown that the classical 95% oxygen concentration would inhibit dilation of arterioles while the same arteriole, at 20% oxygen would dilate (Gordon et al., 2008). *In vivo*, the partial oxygen pressure (pO_2) in the rat brain ranges from 12.7 mmHg to 64.4 mmHg (Offenhauser et al., 2005). In a typical 100 µm thick brain slice oxygenated at 20%, the measured pO_2 values are at the low end of the physiological values, 18.94 mmHg at 50 µm below the surface (Gordon et al., 2008). Considering that in the optic nerve, due to the scattering of light by myelin, the imaging of the blood vessels can only be done in the range of 10 µm – 50 µm from the surface of the tissue, the imaged blood vessels in this thesis will be in normoxic conditions when 20%

oxygen is used. The modulation of NVC by oxygen has also been documented in the retina (Mishra et al., 2011).

The effect of oxygen in modulating the NVC response in the grey matter can be due to a change in enzyme function (Hall et al., 2014) or to the inhibition of a prostaglandin transporter (Gordon et al., 2008). To test if in the optic nerve the oxygen concentration is having the same effect as in grey matter, especially at the pre-capillary level (Hall et al., 2014), I inhibited either the prostaglandin E2 receptor (EP_4) or the cyclooxygenases enzymes (COXs) that produce prostaglandins at both 20% or 95% oxygen. The results show that, as with the grey matter vasculature, the NVC pathway is different between the two conditions (Figure 14 and Figure 15 and Figure 16). Unfortunately, due to lack of time, the inhibition of COXs enzymes at 20% oxygenation is missing. It would be interesting to evaluate if there is an increase in cell death in the inner part of the nerves under 20% oxygenation compared to 95%. Although more data is necessary, the dilation amplitude in control experiments under 20% or 95% seems not to change (Figure 5 and Figure 14 and Figure 15 and Figure 16). This means that the oxygen concentration does not affect the size of vessel dilation.

A key step in NVC, at least in grey matter, is the increase in astrocytic calcium concentration (whether end-feet or soma, remains to be elucidated). Just as in grey matter, in the optic nerve, astrocytes also increase their intracellular calcium concentration upon electrical stimulation of the axons (Hamilton et al., 2008). The action potential triggers axonal ATP and glutamate release through the nodes of Ranvier. Both neurotransmitters will increase the calcium concentration in astrocytes (Hamilton et al., 2008). If the NVC mechanism of the grey matter is extrapolated, then astrocytes can induce vessel dilation in the white matter, via axonal ATP release. However, 99% of the surface of the axon is myelinated, and the node of Ranvier is a highly crowded space with a high amount of sodium channels, glucose transporters, sodium-potassium ATP pumps, and other proteins, making glutamate/ATP vesicular release at these sites unlikely. Instead, there is compelling evidence that vesicular glutamate release along the axon happens in specific places along the internodes (Doyle et al., 2018; Kukley et al., 2007; Ziskin et al., 2007).

Along the internodes, the depolarization caused by the action potential causes vesicular glutamate release into the periaxonal space. NMDA receptors located in the myelin membrane of oligodendrocytes detect the glutamate and induce an increase in calcium concentration in the oligodendrocyte (Micu et al., 2016). As oligodendrocytes are coupled to astrocytes via gap junctions, calcium waves may flow to astrocytes so they can communicate with the vasculature. By using genetically encoded calcium sensors specifically in oligodendrocytes and/or astrocytes, it would be possible to dissect if there is such a calcium wave in the optic nerve.

This model suggests the oligodendroglial NMDA receptors as the most upstream receptor for any kind of NVC signalling in the optic nerve. To confirm this hypothesis, NVC optic nerve experiments were performed in oligodendrocyte-specific NMDA receptor knock-out mice. The results show a decrease in vessel dilation during both the stimulation and the recovery period (Figure 20). However, the time course of the response is unchanged compared to control mice. The time necessary to reach the maximal dilation seems not to differ significantly (Figure 21). These data suggest that the oligodendroglia NMDA receptors are not the only receptor involved in the NVC response, which is expected. It is unlikely that such an important process would depend on only one pathway. Interestingly, the deletion of these receptors does not impact the general vascular architecture of the optic nerve, the corpus callosum, or the cortex of mice, or the resting vessel diameter of the optic nerve's vessels (Figure 17 and Figure 18). This is somehow counterintuitive because if the NVC response is decreased to such levels (Figure 20), I would expect that the tissue adapts by increasing the number of vessels to support the same area more inefficiently, but this seems not to be the case. It is possible that the energetic demands of the axons are covered in excess, or that they are simply not that demanding and thus the reserves are sufficient to support the axon metabolically for a long time, thus there is no rush to resupply the demands by NVC. Nevertheless, these mice show signs of neurodegeneration starting at 10 months of age, indicating that NMDA receptors are very important for normal white matter homeostasis.

The link between oligodendroglial NMDA receptor deletion and decreased NVC in the white matter remains to be further studied. A key factor could be a second messenger that permeates through the NMDA receptors. The candidates for this second messenger are calcium and, to a lesser extent sodium. It has been shown that in astrocytes, after glutamate stimulation, the increase of both sodium and calcium levels induces an increase in GLUT1 receptors (Porras et al., 2008). It is imaginable that the activation of NMDA receptors in oligodendrocytes also increases the concentration of sodium, which can flow as a sodium wave into astrocytes. The basal concentration of sodium in oligodendrocytes and astrocytes is roughly the same at ~15 mM (Ballanyi and Kettenmann, 1990; Rose and Chatton, 2016). There is evidence that an increase in sodium can produce a release of calcium from internal stores in astrocytes, although this response may be specific for cortical astrocytes (Felix et al., 2020; Ziemens et al., 2019). Thus, sodium could act as a second messenger responsible for NVC in white matter. By studying calcium dynamics in oligodendrocytes after NMDA receptor inhibition or deletion, it would be possible to study how much calcium or sodium influx into oligodendrocytes is changed and thus correlate this with the NVC response.

The work performed in this thesis, in addition to other research from the lab, points to the following mechanism in the optic nerve (Figure 25). Oligodendroglial NMDA receptors detect glutamate that is released into the peri axonal space that increases the calcium concentrations inside the oligodendrocytes. By an unresolved mechanism, astrocytes secrete prostaglandin E2, produced by cyclooxygenases. Prostaglandin E2 induces dilation of pre-capillary arterioles via the EP_4 receptors. It remains to be studied if lactate release promotes vasodilation at 20% oxygen, as shown in grey matter (Gordon et al., 2008). As NMDA receptor knock-out mice do not have repolarization differences in the compound action potential (Figure 23), I can rule out that the decrease in NVC is caused by a dysregulation of the potassium buffering. Potassium is a very important vasodilator (Harraz et al., 2018; Longden et al., 2017). It would be interesting to perform these experiments in an oligodendrocyte-specific K_{ir} 4.1 to evaluate the role of potassium release in the optic nerve NVC.

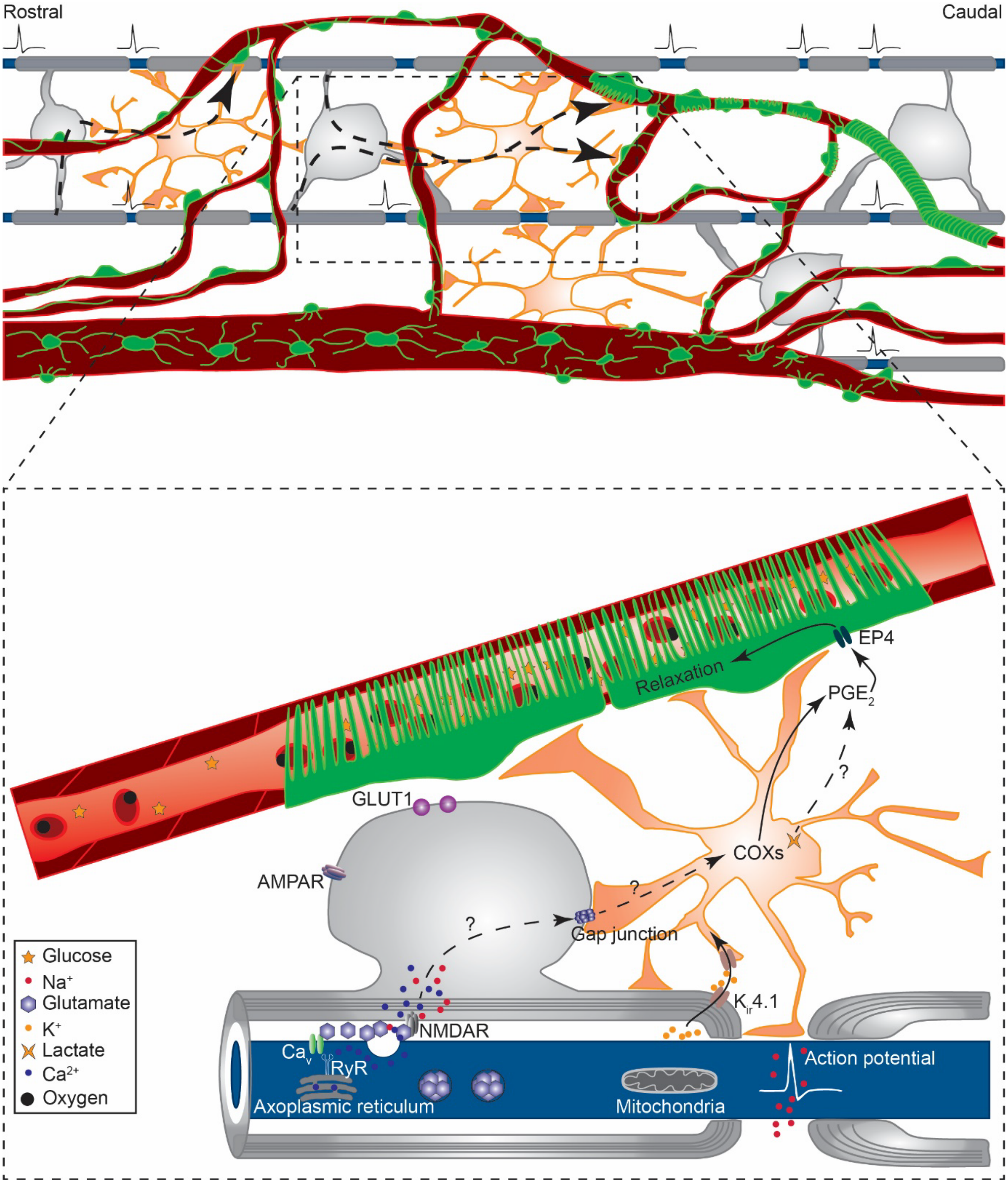

Figure 25: Neurovascular coupling model of the optic nerve. Scheme showing the cellular organization of the optic nerve. Note that the arteriole is mainly located towards the caudal part of the nerve. Oligodendrocytes (grey) wrap the axons (blue) with myelin processes. Astrocytes (orange) directly contact the axons at the nodes of Ranvier and oligodendrocytes either at the myelin or at the soma, and they have contact with perivascular cells (green) with their end-feet. For simplification, only one node of Ranvier, and a pre-capillary arteriole are shown. The action potential is shown to occur only at the nodes of Ranvier representing the saltatory conduction. The dashed arrows show the suspected path the NVC signalling must take. The NVC signalling starts with the NMDA receptors at the myelin. By an unknown mechanism, the astrocytes activate the cyclooxygenases and secrete PGE_2 *that will act on the* EP_4 *receptors on the ensheathing pericytes to dilate the pre-capillary*

arteriole. Dashed lines represent unknown mechanisms and solid arrows represent what was tested in this work.

I am aware that these results should be replicated *in vivo*. However, the study of *in vivo* white matter NVC in mice seems not to be possible at the moment. Access to the callosal vasculature is not easy, although there is some evidence that it is possible to study CBF in callosal capillaries, a highly specialized set-up is needed (Li et al., 2019a). It is also possible to perform a surgery where part of the cortex is removed (Bottes and Jessberger, 2021; Shaw et al., 2021), so the microscope has better access to the callosal vasculature, but the mouse needs to be anesthetized for this procedure. The role of anaesthesia in modulating the NVC response is not fully understood. There is evidence that certain types of anaesthesia change brain connectivity (Xie et al., 2019). It would be wise to avoid anaesthesia that alters cellular respiration like isoflurane or that acts on NMDA receptors like ketamine. Even if the imaging setup is ready and the previous problems are overcome, the stimulation of the trans callosal fibres is still something to think about. It is possible to insert an electrode to stimulate the neurons from the sensory cortex that will cross the corpus callosum but it is necessary to block NMDA receptors to prevent cortical spreading depression (Enager et al., 2009). Those blockers could interfere with the NMDA receptors of oligodendrocytes, thus inhibiting the NVC coupling of the white matter. A way to overcome this would be to use an optogenetic approach to stimulate the same fibres. Something like this was done in 2020, however, fMRI was used to measure BOLD effects in the cortex of mice (Chen et al., 2019), but animals were still under anaesthesia.

To try to overcome all these potential problems, I made a huge leap and looked at the human white matter *in vivo* using fMRI. To replicate the *ex vivo* experiments, a known task that activates the trans callosal fibres (Tettamanti et al., 2002; Weber et al., 2005) was used before a long resting-state measurement. As expected, during the resting state, it was possible to detect different networks that are known to be active during resting-state fMRI (Doll et al., 2015; Zhang et al., 2015). Although BOLD activation seen in white matter is normally considered noise, because of its very low and seemingly undetectable signal, here it was selected as signal and the data was denoised to preserve it. Cleaning the data revealed a strong and specific activation of the middle of the corpus callosum, which is where the fibres activated with the Poffenberger task cross the hemispheres. The spatial map is very specific; however, the time series characteristic of the components has the same pattern as classical noise. Although these experiments were repeated 4 times, in the same subject, the white matter activation was only visible in 3 out of the 4 measurements. Just like with the *ex vivo* experiments, no white matter activation was detected when the task before the resting-state was omitted (Figure 24). Recent evidence suggests that the hemodynamic response function of the white matter has a prolonged initial dip, increased time to peak, and smaller magnitude overall (Li et al., 2019b), additionally it seems to change depending on the white matter region that is analysed.

In conclusion, I present a new technical approach to studying white matter neurovascular coupling. By studying electrophysiological evoked vessel dilation, I showed that oligodendrocytes are partially responsible for the NVC response of the optic nerve. By an unknown mechanism, oligodendrocytes induce the production of, most probably, astrocytic prostaglandin E2, that acts via EP_4 receptors located in ensheathing and mesh pericytes located in the pre-capillary arteriole. White matter activation in humans was also detected only after a specific task, indicating the response could be specific to neuronal activation. There are many different questions and hypotheses to test, but I hope that this work will motivate researchers to explore this vastly understudied area.

MATERIAL AND METHODS

1. ANIMALS

All mice used during this thesis were bred and kept in the animal facility of the Max Planck Institute for Experimental Medicine (now Multidisciplinary Sciences). The animals were handled according to the local animal care guidelines and approved by the institutional board of animal welfare and the animal welfare office of the local Lower Saxony authorities (LAVES). Animals were housed in standard cages and lived in a 12h/12h light-dark cycle with food and water *ad libitum*.

During this work, I have used and crossbred several published lines. The obligatory NR1 subunit of the NMDA receptor is encoded by the *Grin1* gene that is in chromosome 2. The line *Grin1*$^{flox/flox}$ (Tsien et al., 1996) has two *lox P* sites, one between the exon 10 and the exon 11, and the second one is after the exon 22, at the end of the sequence of the *Grin1* gene. Upon recombination of the lox P sites, this arrangement allows for the complete deletion of the 4 transmembrane domains and the entire c-terminal sequence of the NR1 subunit (Tsien et al., 1996). For all the experiments investigating the role of the NMDA receptor, animals were bred to be *Grin1*$^{flox/flox}$ (abbreviated as NR1 fl/fl). Animals were genotyped by me, Gudrun Ficke-Bode or Ursula Kutzke.

To induce recombination of the *lox P* sites, I used a Cre recombinase expressed under the promoter of the *Cnp1* gene (Lappe-Siefke et al., 2003). The *Cnp1* gene expresses the enzyme 2′,3′-cyclic nucleotide 3′-phosphodiesterase (Cnpase) which is a specific marker for mature oligodendrocytes. The Cre recombinase was inserted into the coding region of the *Cnp1* gene as a replacement for the genomic fragments that include most of the exons 1 to 3 (Lappe-Siefke et al., 2003). Animals that do not express the Cre recombinase are denoted as Cnp-Cre +/+, meanwhile, animals that do express the Cre recombinase are denoted as Cnp-Cre +/-. Animals were genotyped by me, Gudrun Ficke-Bode or Ursula Kutzke.

To observe the morphology of all perivascular cells, I used a reporter line that expresses eGFP under the control of the promoter for PDGFR-β (Gong et al., 2003). The BAC vector containing the *egfp* reporter gene was inserted into the *Pdgfr-β* gene before the first coding region. When the transgene is present in the animal, the genotype is denoted as Pdgfr-β-eGFP +. Animals were genotyped by me or Ursula Kutzke.

The genotypes used for this work are presented in the following table (Table 1). All animals were kept on a mixed N/J C57BL/6 background.

Table 1: Genotypes used.

	Cnp-Cre	NR1	Pdgfr-β -eGFP
Control (Ctr)	+/+	fl/fl	+
Conditional knock-out (cKO)	+/-	fl/fl	+

NR1 and Cnp-Cre animals were already present in the animal house of the Max Planck Institute for Experimental Medicine (now Multidisciplinary Sciences). The PDGFR-β-eGFP line was kindly provided by Dr. Annika Keller (Department of Neurosurgery, University Hospital Zürich).

2. GENOMIC DNA ANALYSIS BY PCR DNA-AMPLIFICATION

To identify the genotypes of the mice, two different methods were used interchangeably. The first method was done by chloroform DNA extraction. In this method, tail (or ear clips) biopsies are digested with 400 (200) µl of extraction buffer (Table 2) for ~2 hours at 60°C with constant shaking.

Table 2: Extraction buffer.

Reagent	Concentration
SDS	0.5%
NaCl	0.1 M
Tris (pH 8.0)	0.05 M
EDTA	3 M

After digestion, the supernatant is transferred to a new tube. DNA extraction is done with 75 (37.5) µl of 8 M potassium acetate (sterile filtered; pH not adjusted) and 400 (200) µl of chloroform, which are added to the tubes with the supernatant. Samples are then spinned at 700 g (5415 D, Eppendorf). After 10 min, 100 (200) µl of the supernatant are extracted and transferred to a new tube. Then 400 (200) µl of 100% ethanol are added to the tube and the samples are mixed by inverting the tubes carefully. Next, samples are centrifuged at maximum speed (5415 D, Eppendorf) for 10 min at room temperature (RT). The supernatant is discarded, and the tubes are left until ethanol completely evaporates. Lastly, 200 (100) µl of Tris-HCl (10 mM Tris pH 8.0) is added to the tubes. Samples are vortexed and stored at 4°C for further analysis.

The second method is done using the NexttecTM Tissue & Cells kit. For this method, I followed the manufacturer's instructions (Nexttec Biotechnologie GmbH). Biopsies are digested in 300 µl of lysis buffer (265 µl buffer G1, 10 µl buffer G2, 25 µl buffer G3) for 60 min at 62°C with constant shaking at 1200 rpm. Then, NexttecTM cleanPlates96 are equilibrated with 350 µl per well of Prep buffer for 5 min at RT. Plates are then centrifuged for 1 min at 350 G (Allegra X-15R, rotor: SX 4750). After equilibration of the plates, 120 µl of the lysate is loaded into a column and centrifuged for 1 min at 750 G (Allegra X-15R, rotor: SX 4750) into fresh tubes. The lysates are diluted 1:5 in ddH_2O.

The isolated DNA is amplified by Polymerase Chain Reaction (PCR) (Mullis et al., 1986) to identify the genotype of the mice. To run all the PCRs, I follow the instructions of the GoTaq DNA polymerase kit (Promega), as shown in (Table 3).

Table 3: PCR master mix.

Reagent	Volume (µl)
ddH_2O	12.65
dNTP mix (2mM)	2.00
5x GoTaq buffer	4.00
Forward primer (50 pM)	0.10
Reverse primer (50 pM)	0.10
GoTaq polymerase (5 U/ µl)	0.15
DNA sample	1.00

2.1. Primers

Each gene had its own set of primers for the PCR. The primers have been designed by the original creators of each transgenic mouse and are synthesized by the AGCT lab at the Max Planck Institute for Experimental Medicine (now Multidisciplinary Sciences).

Forward primer NR1 (# 24233)

5’-CTGTCAGTTCAAGGCCAGCAT -3’

Reverse primer NR1 (# 24234)

5’-GTGCTGGGATCCACATTCATG -3’

Forward primer 1 CNP-Cre (# 1955)

5´-GCCTTCAAACTGTCCATCTC-3´

Forward primer 2 CNP-Cre (# 2016)

5´-CATAGCCTGAAGAACGAGA-3´

Reverse primer CNP-Cre (# 7315)

5´-CCCAGCCCTTTTATTACCAC-3´

Forward primer Pdgfr-β-eGFP (# 4618)

5’ GTGGAAGCAGAGAGGAGAGCATTTG 3’

Reverse primer Pdgfr-β-eGFP (# 38749)

5’ GGTCGGGGTAGCGGCTGAA 3’

2.2. PCR programs for genotyping

The PCR programs for each gene of interest are presented below (Table 4).

Table 4: PCR programs for genotyping of each gene.

NR1		**Cnp-Cre**		**Pdgfr-β-eGFP**	
Temperature (°C)	*Time*	*Temperature (°C)*	*Time*	*Temperature (°C)*	*Time*
95	Pause	95	Pause	95	Pause
95	5 min	95	3 min	94	5 min
(95	30 sec	(50	30 sec	(94	15 sec
63.5	30 sec	72	1 min	64	30 sec
72	30 sec) x34	95	30 sec) x35	72	40 sec) x40
72	30 sec	50	1 min	72	5 min
4	Pause	72	10 min	4	Pause
		4	Pause		
		Expected band size			
WT: 350 Het: 350 and 500 fl/fl: 500		WT: 700 +/-: 400		tg: 425	

It is recommended that for the NR1 PCR, loud music is playing in the background. Until now Latin music and jazz-funk music have been tested and both work equally well.

3. OPTIC NERVE CLEARING

The clearing protocol and imaging of cleared samples using light-sheet microscopy were performed by Dr. Constanze Depp and Andrew Octavian Sasmita.

3.1. Solutions for optic nerve clearing

Table 5: List of solutions for optic nerve clearing

Name	**Composition**	**Concentration**
PFA in PBS	PFA	4%
	NaCl	137 mM
	KCl	2,7 mM
	Na_2HPO_4	8 mM
	KH_2PO_4	1.5 mM
PTwH	PBS	1 X
	Tween-20	0.2%
	Heparin	10 mg/ml
	NaN_3	5 mM

3.2. Tissue collection

Mice aged 14 weeks were sacrificed by cervical dislocation. Optic nerves were rapidly removed and fixed with 4% paraformaldehyde (PFA – Merck) diluted in PBS for 16 hours. The tissue was then transferred into a solution of PBS containing 0.01% NaN_3 and stored at 4°C until use.

3.3. Tissue clearing

The clearing protocol is a series of steps that will dehydrate, remove lipids and hydrate back the tissue. All the steps are presented in the table below. Overnight steps are marked as ON (Table 6).

Table 6: Tissue clearing for light-sheet microscopy protocol.

Step	Solution	Time	Temperature
Dehydration	50% MeOH/ 50% PBS	1 hour	RT
	80% MeOH/ 20% PBS	1 hour	RT
	100% MeOH	1 hour	RT
	100% MeOH	1 hour	RT
Bleaching	1:1:4 H_2O_2:DMSO:MeOH	ON	4°C
Delipidation	100% MeOH	30 min	4°C
	100% MeOH	3 hours	-20°C
	100% MeOH	ON	4°C
	80% MeOH/ 20% PBS	2 hours	RT
Rehydration	80% MeOH/ 20% PBS	2 hours	RT
	50% MeOH/ 50% PBS	1 hour	RT
	100% PBS	1 hour	RT
	0.2% Triton X-100/PBS	1 hour	RT
	0.2% Triton X-100/PBS	1 hour	RT
Permeabilization	PBS/0.2% Triton X-100/ 20% DMSO/ 0.3 M glycine	ON	37°C
Blocking	0.2% Triton X-100, 10% DMSO and 6% goat serum	3 days	37°C
	PTwH	1 hour	RT
	PTwH	1 hour	RT
Antibody labelling	PTwH/ 0.2% Triton X-100, 5% DMSO and 3% Goat serum + primary antibody (Table 7) antibody	14 days	37°C
	6x PTwH	1 day	RT
	PTwH	ON	37°C
	PTwH/3% Goat serum + secondary antibody (Table 8)	7 days	37°C
Washing	6x PTwH	1 day	RT
Embedding	Phytagel 1.5% w/v in PBS		
Dehydration	20% MeOH/ 80% PBS	1 hour	RT
	40% MeOH/ 60% PBS	1 hour	RT
	60% MeOH/ 40% PBS	1 hour	RT
	100% MeOH	1 hour	RT
Delipidation	1:2 MeOH:dichloromethane	ON	RT
	Dichloromethane	40 min	RT
Clearing	Ethyl cinnamate (Eci)	1 hour	RT
Storage	Eci	-	-

Table 7: Primary antibody list for light-sheet microscopy.

Cell type or structure	Marker	Antibody type and host	Dilution	Supplier
Endothelial cells	Podocalyxin	Rat monoclonal [192703]	1:500	R&D Systems. MAB1556
Perivascular cells	eGFP	Chicken polyclonal	1:500	Alves labs. GFP-1020

Table 8: Secondary antibody list for light-sheet microscopy.

Antibody host	Fluorophore	Dilution	Supplier
Donkey anti-rat	AlexaFluor 555	1:500	Molecular probes
Goat anti-chicken	AlexaFluor 633	1:500	Invitrogen

3.4. Tissue imaging in light sheet

Cleared samples were imaged using a commercial light-sheet microscope, UltraMicroscope II (LaVision Biotec), equipped with a 2x objective lens. The tissue was submerged in a sample cuvette containing ethyl cinnamate (ECI). Images were acquired with the mosaic acquisition mode using 5 µm light sheet thickness, 30% sheet width, 0.154 sheet numerical aperture, 4 µm z-step size, 5-step dynamic focus, and 100 msec exposure time. AlexaFluor 555 was imaged using a 561 nm laser and the fluorescence emission was detected with a 585/40 filter. AlexaFluor 633 was excited with a 640 nm laser and the fluorescence emission was detected using a 680/30 filter. Images were imported into Vision4D v3.2/v3.1 (Arivis) and stitched using the tile sorter configuration. Stitched images were exported and the contrast was adjusted with Fiji (Schindelin et al., 2012).

4. OPTIC NERVE RECORDINGS

4.1. Solutions

Artificial cerebrospinal fluid (aCSF) was constantly bubbled with carbogen (95% O_2 + 5% CO_2) or with a mixture of 20% O_2 + 5% CO_2 + 75% N_2, and superfused the optic nerve in the incubation chamber. The aCSF was prepared as a 2X stock A (Table 9) and 2X stock B (Table 10) that were kept at 4°C, as shown below. On the day of the experiment, stock A and B were mixed in a 1:1 ratio. $CaCl_2$ 4M (Merck) was diluted to reach a concentration of 2 mM in the aCSF and the energy substrates were added to reach a concentration of glucose 3.3 Mm (Sigma Aldrich) and sucrose 6.7 mM (Merck). This solution is denoted as 3.3 mM aCSF. All recordings were performed in 3.3 mM aCSF.

Table 9: aCSF stock A composition. All reagents were manufactured by Merck.

	Concentration (mM)	**Molecular weight (g mol^{-1})**	**Osmolarity (mOsm)**
NaCl	126	58.44	252
KCl	3	74.55	6

Table 10: aCSF stock B composition. All reagents were manufactured by Merck.

	Concentration (mM)	**Molecular weight (g mol^{-1})**	**Osmolarity (mOsm)**
NaH_2PO_4	1.25	137.99	2.5
$NaHCO_3$	26	84.01	52
$MgSO_4$	2	246.48	4

4.1.1. U46619

U46619 (Cayman chemical, 16450) is a thromboxane A2 analogue, used here as a blood vessel constrictor. It binds to the thromboxane A2 (TP) receptor with an EC_{50} = 0.035 µM. The TP receptor is expressed by all pericytes and smooth muscle cells (Vanlandewijck et al., 2018). The stock solution was kept at -20°C according to manufacturer instructions. Based on published data (Gonzales et al., 2020; Mishra et al., 2014) and the EC_{50}, I prepared aCSF with U46619 (100 nM – final concentration) for every experiment by diluting the U46619 stock directly into the freshly prepared aCSF. For 300 ml of aCSF, I used 1.1 µl of U46619 (stock solution).

4.1.2. ACh

Acetylcholine (ACh – Sigma Aldrich, A6625) has a vasodilator effect in the brain vascular system. ACh acts via muscarinic receptors present in endothelial cells (Yamada et al., 2001). Although ACh mechanism of action would suggest a vasoconstriction, the production of nitric oxide by the endothelial cells induces dilation by relaxing perivascular cells and adjacent endothelial cells (Manicam et al., 2016).

The solution of aCSF with Ach (100 µM – final concentration) (Manicam et al., 2016; Yamada et al., 2001) was prepared fresh for every experiment by dissolving the powder directly into the freshly prepared aCSF. For 300 ml of aCSF, I used 5.4 mg of ACh.

4.1.3. TTX

Tetrodotoxin (TTX – Alamone labs, T-550) is a potent blocker of a subclass of voltage-gated sodium channels (Na_V channels). It is extracted from the pufferfish, *Tetraodon pardalis*, and used here to inhibit axonal firing by blocking the Na_V channels that participate in action potential generation and propagation (Chong and Ruben, 2008).

TTX was diluted with ddH_2O to reach a stock concentration of 10 mM, aliquoted into 30 µl vials, and kept at -20°C following manufacturer instructions. A high concentration (1 µM) of TTX was used to get a complete inhibition of all the Na_V channels. For 300 ml of aCSF, I diluted an aliquot (30 µl) of TTX into the freshly prepared aCSF.

4.1.4. L-161,982

L-161,982 (Tocris, 2514) is an antagonist of the prostaglandin E2 receptor EP_4. Although it can inhibit other prostaglandin receptors involved in the vasodilator response like DP and IP, the K_i for these receptors is much higher. The K_i for the EP_4 receptor is 0.024 µM, meanwhile, for DP and IP, it is 5.10 µM and 6.74 µM, respectively.

L-161,982 was dissolved in DMSO to form a stock of 100 mM, as recommended by the manufacturer. The stock was aliquoted into 3 µl vials and kept at -20°C until use. I prepared freshly aCSF with L-161,982 (1 µM) (Mishra et al., 2016) for every experiment by diluting a 3 µl aliquot into 300 ml of aCSF.

4.1.5. Indomethacin

Indomethacin (Tocris, 1708) is a general COX1/2 enzymes inhibitor, and thus an inhibitor of any prostaglandin production. The IC_{50} for human COX1 is 230 nM and for COX2 is 630 nM.

Indomethacin was dissolved in DMSO to form a stock solution of 100 mM, as recommended by the manufacturer. The stock was aliquoted into 150 µl vials and kept at -20°C until use. I prepared freshly aCSF with indomethacin (25 µM) for every experiment by diluting a 75 µl aliquot into 300 ml of aCSF.

4.2. Tissue preparation

For all the optic nerve recording experiments, 14 weeks old mice were used. Mice were anesthetized with a combination of Midazolam (5.0 mg/kg), Medetomidine (0.5 mg/kg) and Fentanyl (0.05 mg/kg) in sterile 0.9% saline solution (MMF) via intraperitoneal injection using 100 µl per 10 g of body weight. After checking that the animal was in deep anaesthesia by pinching the paw, the mice were injected 100 µl of 70 kDa Dextran-Texas red (10 mg/ml – Life Technologies, D1830) dissolved in PBS pH 7.4 via tail vein.

Mice were decapitated and the optic nerves were excised as fast as possible without damaging them. One optic nerve was placed on the interface Brain/Tissue Slice (BTS) chamber system (#65-0073; Harvard apparatus), between the two suction electrodes and kept under constant aCSF flow. The chamber was continuously aerated by humidified carbogen and kept at a constant 35°C using a feedback-driven temperature controller (TC-10, NPI electronic) connected to a temperature probe (TS-100-S, NPI electronic) inserted directly into the BTS chamber. The second nerve was kept in a solution of aCSF at RT with constant oxygen bubbling until it was time to use it in the BTS chamber.

For some experiments where the eGFP reporter was not available, isolectin-IB4 was used to label the basement membrane, and thus find pericyte somas. For this, nerves were incubated in a solution of isolectin-IB4, from *Griffonia simplicifolia* (100 µg/ 100 µl – Thermo Fisher Scientific, I21411) diluted in aCSF 1:200 for 24 min at RT with constant oxygen bubbling. Then one nerve was placed in the BTS chamber and the other stayed in the lectin solution until used.

4.3. Electrophysiological recordings

This protocol has been published elsewhere (Asadollahi et al., 2022; Trevisiol et al., 2017), but for clarity sake I will write it here. The glass suction electrodes were custom made by manually bending the glass capillaries (1.5 mm, #1B150-6, World Precision Instruments) with the flame of a Bunsen burner to an angle between 35 and 40°. The opening on the side where the optic nerve enters was adjusted to the specific diameter of the optic nerve by melting and polishing the tip with the flame of the burner.

To elicit and record the action potential propagation along the axons, an injection of electrons into the media is needed. For this, a chlorinated silver wire was inserted into the suction electrodes. The stimulating electrode was connected to a battery (Stimulus Isolator A 385, World Precision Instruments) that delivered a supramaximal stimulus of 0.75 mA that evoked the compound action potential (CAP).

The recording electrode is connected to the headstage, the signal is amplified 10-fold by a preamplifier (EXT-10-2F, NPI electronic) and subsequently 20-fold by a low-noise preamplifier (SR 560, Stanford Research Systems). The amplified signal is low-passed filtered at 30 kHz, defined by the SR 560 preamplifier, and acquired at 20 or 100 kHz by the HEKA EPC9 amplifier (Heka Elektronik). The reference channel was recorded by an aCSF filled glass capillary, in contact with the bathing aCSF, next to the recording electrode.

To stabilize and manipulate the electrodes, they were attached to two micromanipulators (Luigs & Neumann). To follow the orientation of the optic nerve in the body, the rostral side (to the retina) was inserted into the stimulating electrode, and the caudal side (to the optical chiasm) was inserted into the recording electrode.

During the experiments, nerves were recorded at a baseline stimulation of 0.1 Hz. The stimulation at 16 Hz, 25 Hz, and 100 Hz was done by burst-like stimulation. The burst was done by applying 100 stimuli at the desired frequency separated by 25 msec during which the CAP was recorded. The stimulation at 4 Hz was done by continually stimulating the nerve every 25 msec.

5. BLOOD VESSELS IMAGING IN THE OPTIC NERVE

Imaging of the acute excised optic nerves was performed using a modified up-right confocal laser scanning microscope Zeiss 510 META/NLO (Carl Zeiss AG) equipped with a 63x water immersion objective (Achroplan IR 63x/0.9 W, Carl Zeiss AG). Dextran-Texas red was imaged with the Helium-Neon laser using a laser line of 543 nm and eGFP, or IB4-488, were imaged with the Argon laser using a laser line of 488 nm. The main beam-splitter (HFT UV/488/543/633) and a dichroic beam-splitter (NFT 545) allowed for the simultaneous imaging of the two used lasers. The signal of the 543 nm laser was recorded using a band-pass filter 565-615 nm. A bandpass filter 500-550 nm was used to record the signal from the 488 nm laser.

As the resolution of the microscope is imposed by the Rayleigh criterion, which follows the equation $r = \frac{1.22\lambda}{2n sin\theta} = \frac{0.61\lambda}{NA}$, where r is the minimum distance where two points can be distinguished from each other as different entities (Waters, 2009), λ is the wavelength of the emission of the fluorophore and NA is the numerical aperture of the objective used. In our case, the maximum resolution the microscope can reach is 0.35 µm, thus a pixel size smaller than that will not provide further information, instead, it will increase the bleaching of the tissue. Based on this, I decided to image using a pixel size (px) of 0.37 µm, a frame size of 256 x 256 px, and an image size of 95.1 x 95.1 µm. This resulted in a pixel dwell time of 2.51 µsec and a scan time of 196.61 msec per frame. To keep the imaging time as short and fast as possible, I did not use averaging during acquisition.

Due to the high scattering nature of myelin, I used an open pinhole to increase the amount of light that would hit the detector. The theoretical optical section used was 5.0 µm (2.98 Airy Units). To ensure that the imaged vessel was always being observed in its entirety, I used a z-stack configuration of 17 slices and an interval between slices of 2.51 µm. In total, this gives a z-stack of 40.13 µm, which takes the microscope ~ 17 secs to image. Additionally, there are 3 secs between frames, meaning that a frame was imaged every 20 secs.

6. IMMUNOHISTOCHEMISTRY

6.1. Tissue collection

Mice were sacrificed by CO_2 asphyxiation and transcardially perfused with HBSS with heparin, to prevent blood clots formation, followed by 4% PFA diluted in PBS. The brain was collected and postfixed in 4% PFA ON. The tissue was then changed into a solution of PBS containing 0.01% NaN_3 and stored at 4°C until use.

The brain tissue was sliced using a vibratome (VT1000S, Leica) with a thickness of 60 µm and stored in PBS containing 0.01% NaN_3 until use.

6.2. Solutions immunohistochemistry

The tissue sections were incubated ON in a blocking-permeabilizing solution containing 5% bovine serum albumin (Merck) and 2% Triton-X 100 (Merck) in PBS at 4°C with constant shaking. Slices were then incubated with primary antibodies (Table 11) diluted in the PS/2 solution for 2 days at 4°C with constant shaking. PS/2 solution is the blocking-permeabilizing solution diluted 1:1 in PBS. The tissue was then washed three times with PS/2 solution and incubated ON with the secondary antibodies (Table 12) that were diluted in PS/2 at 4°C with constant shaking. After 2 washes with PS/2 and 3 with PBS, the tissue was incubated for 5 min with DAPI (300 nM in PBS – Thermo Fischer) and mounted using Aqua-Poly Mount (Polysciences, Inc).

Table 11: Primary antibody list.

Cell type or structure	Marker	Antibody type and host	Dilution	Supplier
Basal membrane	Collagen IV	Rabbit polyclonal	1:300	Bio-Rad. 2150-1470
Pericyte	CD13	Rat monoclonal [R3-63]	1:100	Bio-Rad. MCA2183GA

Table 12: Secondary antibody list.

Antibody host	Fluorophore	Dilution	Supplier
Donkey anti-rat	Cy3	1:300	Dianova
Donkey anti-rabbit	AlexaFluor 488	1:300	Molecular Probes

6.3. Tissue imaging with confocal microscopy

Imaging of the brain slices was performed with a Zeiss LSM 880 with Airyscan Fast (Carl Zeiss AG). Images were acquired using a 20x dry objective (Plan-Apochromat 20x/0.80 M27, Carl Zeiss AG). Cy3 fluorophores were excited with a laser line of 561 nm and the emission was recorded using a hybrid detector set to detect between 571-633 nm. AlexaFluor 488 was excited by a laser line of 488 nm and the emission was recorded using a hybrid detector set to detect between 499-553 nm. DAPI was excited using a laser line of 405 nm and the emission was recorded with a PMT set to detect between 437-482 nm. Two main beam-splitter were used to allow for the simultaneous acquisition of different laser lines. One main beam-splitter (MBS 488/561/633) allowed for the Cy3 and AlexaFluor488 imaging and another one (MBS 405) allowed for DAPI imaging.

A z-stack configuration of 37.1 µm was used to image the tissue. Due to the objective and the used fluorophores, the maximum resolution of the microscope was 0.40 µm, thus the pixel size was 0.42 x 0.42 x 1 µm, the frame size was 1024 x 1024 px and the image size was 425.10 x 425.10 µm.

7. DATA ANALYSIS

7.1. CAP

The function and overall health of the optic nerve were monitored by using the CAP signal, which is proportional to the number of excited axons inside the nerve (Saab et al., 2016; Stys et al., 1991). The CAP was recorded as described before (4.3 Electrophysiological recordings) using Patchmaster software (Heka Elektronik). The traces were exported into a format that can be read by MATLAB (MathWorks), in this case, a ".mat" file format was used. The script developed by Dr. Andrea Trevisiol is used to calculate the CAP area that represents the area under the curve of the waveform and plot it over time. The script is presented in the Appendix (1 CAP analysis script). The area under the curve is calculated by integrating the area that starts approximately 0.2 ms after the stimulus artefact and ends at the lowest point of the second peak, which is marked manually. The data was relativized to the mean of the baseline (one minute before the start of the stimulation with 4 Hz or 25 Hz or 100 Hz). The data of several optic nerves were pulled together, averaged, and plotted over time. The variability of the data is shown in those graphs by plotting the standard deviation of the mean.

7.2. Vessel diameter

This section refers to the diameter calculations of the vessels in the optic nerve recordings. The images were acquired using the microscope software Zen 2009 (Carl Zeiss AG). The files were saved as ".LSM" and were opened using Fiji (Schindelin et al., 2012). The vessel diameter analysis consists of a routine composed of 3 different scripts written by Camilo Restrepo Arango shown in the Appendix (2 Vessel diameter – Script 1, 3 Vessel diameter – Script 2, and 4 Vessel diameter – Script 3) and shown schematically in Figure 26.

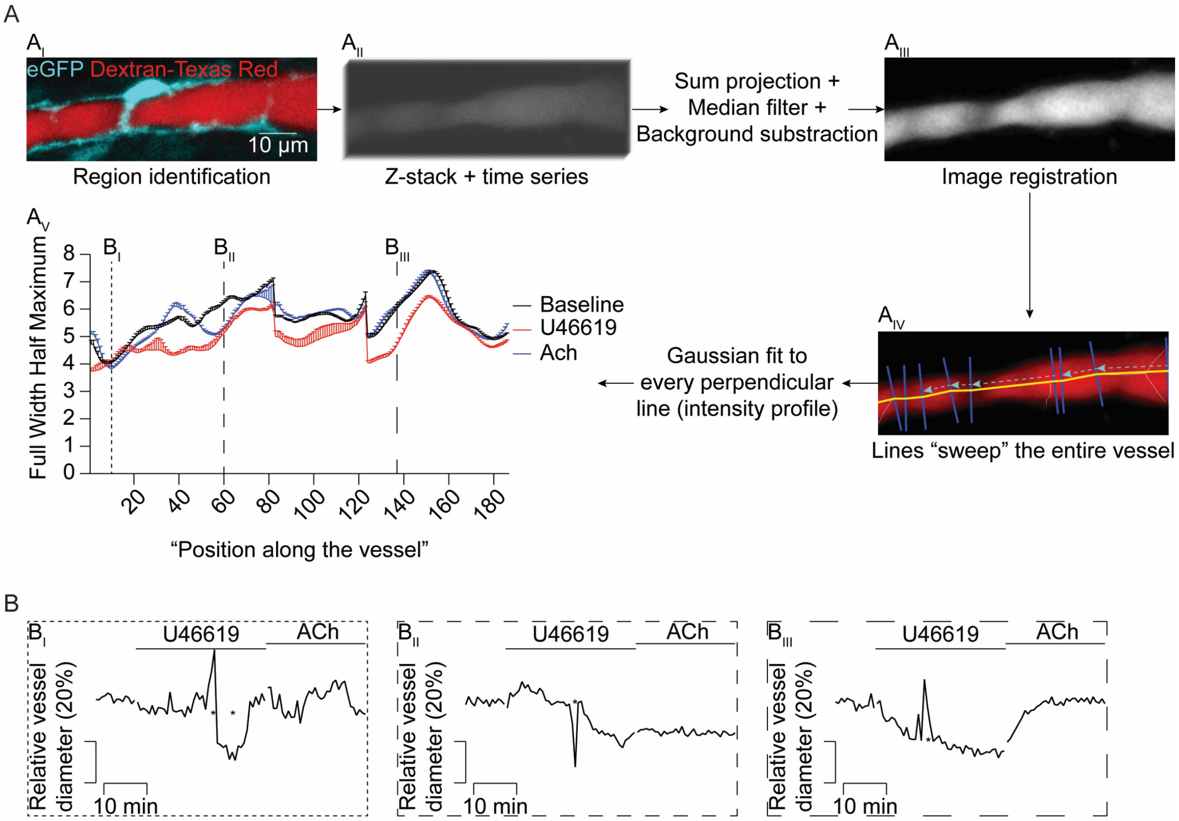

Figure 26: Vessel diameter quantification. ***A)*** *Image processing routine. A_I) Once the desired region is identified based on the morphology of the perivascular cell and the patency of the blood vessel, the experiment can be started. A_{II}) All images taken during the experiment are concatenated into one image. Then the 17 slices are added using the Sum slices algorithm of Fiji. Using a median filter, the image is denoised. A_{III}) The new image is registered to reduce the movements in the x-y axis using one or more plugins in Fiji. A_{IV}) Lines (yellow) are drawn following the centre of the vessel. A perpendicular line (blue) is created and moves along the yellow line as shown by the pale blue dashed arrows. The intensity profile, a Gaussian fit, and the FWHM of each perpendicular line are calculated. A_V) The FWHM is plotted as a function of the position along the vessel. For clarity, data are presented as mean + standard error of the mean.* ***B)*** *To choose a position for further analysis two criteria need to be true: the line of U46619 is lower than the baseline and the curve for ACh needs to be higher than the U46619. B_I) Vessel diameter over the time at the position shown in A_V. There is no change in diameter with the different treatments. B_{II}) Vessel diameter over the time at the position shown in A_V. There is a constriction but there is no dilation with ACh, indicating that in this position the cell is not capable of dilating, possibly because it has died during the experiment. B_{III}) Vessel diameter over the time at the position shown in A_V. This position meets the two necessary criteria for analysis. The peaks marked with an asterisk during the U46619 treatment are due to a cell passing by inside the blood vessel during the acquisition.*

Due to the normal movements of the nerve during the experiments, the number of files per experiment is not constant. Each experiment requires that the researcher visually evaluates that the entire nerve is always being imaged in case the movement creates the nerve to be out of the imaging plane, it is necessary to pause the acquisition, re-centre the nerve, and continue with the acquisition. This creates a new file.

For the analysis, all the files are first concatenated into one file (Image 1). Next, the 17 slices are summed together (Image 2). A median filter with a kernel of 4 px is used to denoise the image (Image 3). The median filter keeps the border of the objects; thus, it is suitable for this analysis. A second median filter with a kernel of 30 px is run over image 3 to create an image with just background (Image 4). The created background will be subtracted from Image 3 to improve the denoising and create a new image (Image 5) (Figure 26 A_{I} and A_{II}). This process does not change the diameter of the vessel (Figure 27).

Image 5 is then registered using one or more Fiji plugins for image registration. StackReg (Thévenaz et al., 1998) is the main plugin used. If this fails to register properly the image, then Image Stabilizer is used (https://imagej.net/plugins/image-stabilizer). In case none of the above plugins works, a manual registration (https://imagej.net/plugins/manual-drift-correction) was performed. Depending on the movement of the nerve, a combination of plugins was used (Figure 26 A_{III}).

The registered image was then segmented using the Li algorithm (Li and Tam, 1998) in Fiji. The segmented image was skeletonized to obtain the centre of the vessel. The centre of the vessel is used as a guide to draw ROIs (region of interest). These ROIs were utilized to calculate the diameter of the vessel. A perpendicular line of 5 pixels width and 60 pixels length was drawn on top of the previous ROIs that mark the centre of the vessel. The intensity profile of the image along that line was calculated and fitted to a Gaussian curve (Figure 26 A_{IV}). The diameter of the vessel is then measured by calculating the Full-Width at Half Maximum (FWHM) of each fitted curve. The perpendicular line will sweep all the ROIs and save the FWHM of each line, thus calculating the diameter of the vessel at each point during the entire duration of the experiment. The data of the last 6 frames before the start of any pharmacological treatment (U46619, ACh, TTX, etc.) or stimulation (4, 25, or 100 Hz), is averaged and plotted over the number of frames of the experiment, creating a graph that shows the FWHM over the number of frames (Figure 26 A_{V}). To avoid any bias of the region, only the frame where the curve of U46619 is below the baseline and, at the same time, the curve of ACh is above the U46619 one, is taken for quantification of the vessel diameter over time. Once this region is identified, the FWHM data is relativized to the baseline (2 min before the start of U46619) and plotted over time (Figure 26 B). In case multiple regions fit these criteria, a visual inspection of the location of the line is performed and if it is clear that they belong to two different pericytes, they are counted as two different measurements, giving an n= 2. This is a common practice in such techniques (Mishra et al., 2014, 2016).

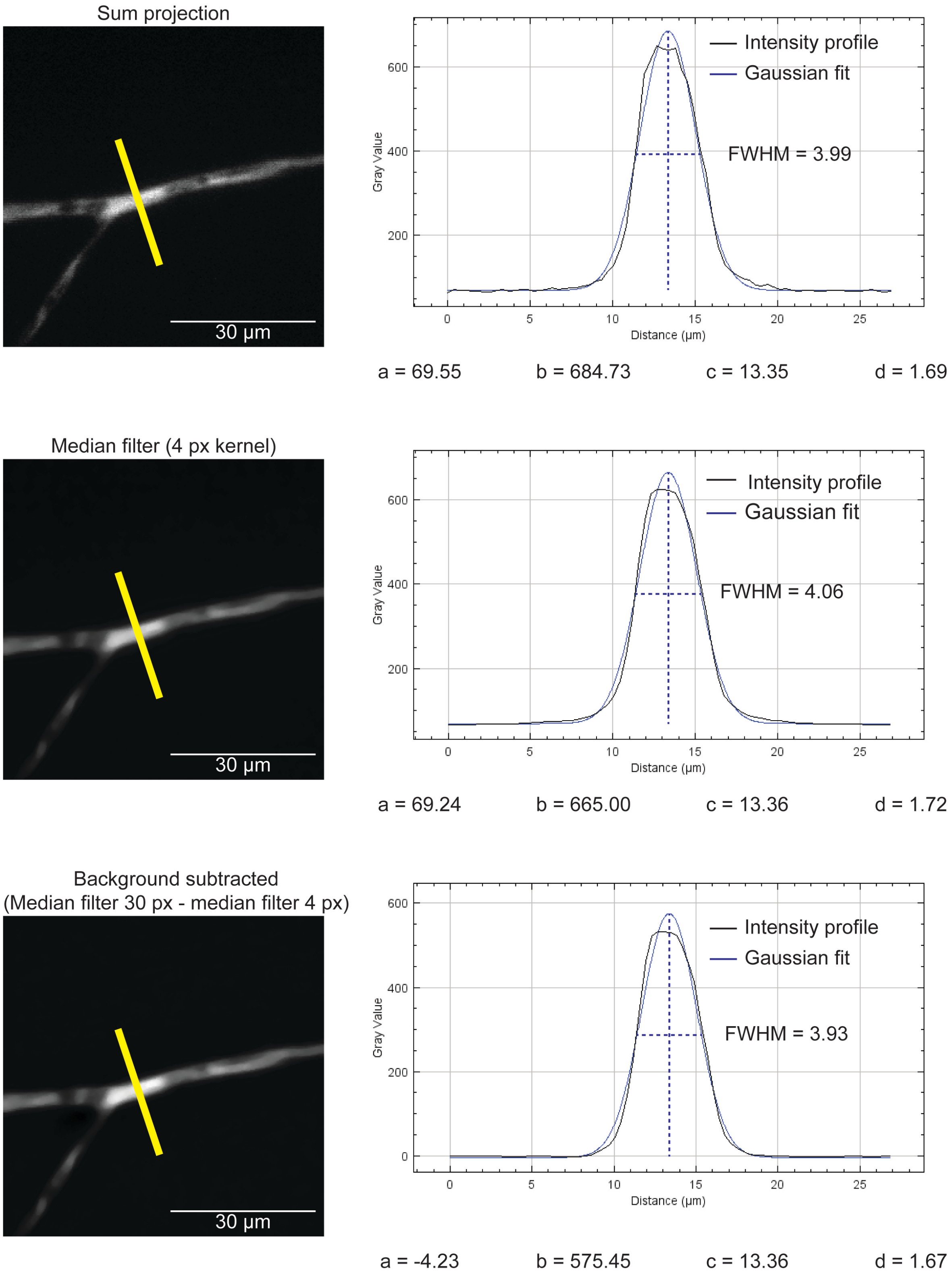

Figure 27: Median filter for denoising does not change the measurements. Image of a vessel after the sum projection, showing one position for intensity measurement (yellow line). The intensity profile is measured along the yellow line. The profile is shown in the graph on the right. The Gaussian fit (blue) is overlapping with the intensity profile (black). The reported values correspond to the values of the Gaussian curve (with offset) $y = a + (b - a) * e^{(-\frac{(x-c)*(x-c)}{2*d*d})}$*, where a: is the offset created by the background, b: is the height of the curve, c: is the position of the centre of the peak and d: is the*

standard deviation. With those values, the Full-Width Half Maximum can be calculated by $FWHM = 2 * \sqrt{2\,ln\,2} * d$. *It represents the vessel diameter. As shown on each graph, the values only change minimally by the application of the different filters, especially between the unfiltered image (sum projection) and the used image (background subtracted).*

7.3. Pericyte number

The pericyte number in brain slices was calculated by counting the number of nuclei, stained by DAPI, in CD13 positive cells in the white matter or the cortex using the cell counter plugin in Fiji. Both regions were delimited by hand in Fiji and the area of the region was calculated. The number of nuclei was extrapolated to have the number of pericytes per mm^2. This was done in two different slices for each animal; thus, each data point corresponds to the average of two technical replicates for each animal.

7.4. Vascular length

The average vascular length in brain slices was calculated using the NeuronJ plugin (Meijering et al., 2004) in Fiji. As well as for the pericyte number, the vessel length was calculated in both white matter and grey matter. The volume of each region was calculated by delimiting it by hand. The vessel is then traced using NeuronJ and the result is extrapolated to be in m/mm^3. This was done in two different slices for each animal; thus, each data point corresponds to the average of two technical replicates for each animal.

8. FUNCTIONAL MAGNETIC RESONANCE IMAGING

8.1. Subject

One subject (the author of this thesis, male, 30 years) took part in four sessions of functional magnetic resonance imaging (fMRI). Each session was composed of two measurements separated by a rest period of 15 min where the participant was taken out of the MRI and allowed to walk and refresh. A measurement is composed of two continuous fMRI measurements starting as a task-based measurement and then continuing as a non-task-based, resting-state measurement. The other two sessions had two only resting-state measurements for the same duration as the combined task / resting-state measurements in the previous two sessions. Before each session, informed written consent was obtained from the subject.

8.2. Magnetic Resonance Imaging

A 3 T system (TIM Trio, Siemens Healthcare, Erlangen Germany) along with a 20-channel head coil was used. In each session, a whole-brain anatomical MR image and two fMRI measurements combining task-based and resting-state or only resting state were obtained.

The anatomical MR image was obtained by sagittal T1-weighted 3D MPRAGE (magnetization-prepared rapid gradient echo) imaging (repetition time (TR) = 1.900 msec, echo time (TE) = 3.57 msec, flip angle = 9°, acquisition matrix = 256 × 256, 176 partitions, spatial resolution = 1 mm × 1 mm × 1 mm).

For functional MRI, a gradient-echo EPI (echo planar imaging) sequence (TR = 1000 msec, TE = 37 msec, flip angle = 60°, acquisition matrix = 64 × 64, field of view = 192 mm × 192 mm, Multiband factor = 2, GRAPPA factor = 2, spatial resolution = 3 mm × 3 mm × 3 mm) was used. Thirty-two slices were positioned to cover the entire brain, except the cerebellum.

8.3. Task

To induce trans-callosal fibre activation, a modified Poffenberger task was used (Tettamanti et al., 2002; Weber et al., 2005). This task triggers both intrahemispheric and interhemispheric fibres activation. If the used visual hemifield is the one from the same side as the hand used for the motor response, the response will be intrahemispheric. If the used visual hemifield is opposite to the side of the hand used for the motor response, an interhemispheric response will be triggered.

The subject was instructed to press a button each time a visual stimulus was shown on a screen. To avoid any effect of handedness, one fMRI measurement was performed using the left hand while the other measurement was done using the right hand.

The visual stimulus consists of a checkerboard that was back-projected by a projector onto an opaque screen covering the back of the bore. The participant could see this screen through a mirror attached to the head coil. A white fixation square on a black background was projected in the centre of the screen, on which the subject was asked to maintain the gaze. The visual stimulation consisted of a narrow strip of black and white checkerboard appearing at the left or right border of the screen, stimulating the left or right visual hemifield. The participant had to press a button with the index finger as fast as possible following each stimulus.

Each fMRI measurement consisted of 15 stimulation periods (12 sec) and 15 rest periods (12 sec). Within the stimulation periods, eight visual stimuli (100 msec) were presented either on the left or right border of the visual field interrupted by a varying interstimulus interval. The total duration of task-based fMRI was 6:20 min, with 1 sec TR, resulting in 380 MR images. When all 15 stimulation periods were shown, the measurement continued for the next 30 min (1800 images) as a resting-state measurement, with the only instruction to keep the eyes open and to gaze at the fixation square. The total time of each measurement was 36:20 min. In the task-based part of the first measurement, the subject pressed the button with the right hand, the second measurement was done with the left hand. There was no interruption between the task-based and the resting-state parts.

In the two control sessions no stimulation or task was performed. In these cases, the entire run of 36.20 min (2180 images) was a resting-state fMRI measurement.

8.4. Data analysis

The data of four fMRI sessions were analysed. The last 30 min (1800 images) resting-state fMRI were considered for data exploration, omitting the first 6:20 min (360 images) of task-based or resting-state fMRI. The entire data analysis was performed using the MRI analysis software “FSL” (FMRIB software library v.6.0, University of Oxford) (Jenkinson et al., 2012; Smith et al., 2004).

As a first step the T1-weighted whole brain structural images were brain extracted using BET (Brain Extraction Tool) (Smith, 2002) using the individual coordinates as the centre of gravity for the mesh surface.

The data was pre-processed in MELODIC using FLIRT for motion correction (Greve and Fischl, 2009; Jenkinson and Smith, 2001; Jenkinson et al., 2002). A high pass filter of 3600 sec was used but turned off during the pre-processing. No spatial smoothing was applied. Two step registration was applied to register the individual fMRI data to the MNI 152 2 mm standard brain using the individual T1-weighted images of each session.

To use a model-free approach, the fMRI measurements were analysed using Independent Component Analysis (ICA) as implemented in MELODIC (Multivariate Exploratory Linear Optimized Decomposition into Independent Components). The resulting data is grouped into "components". A component is a group of voxels with similar time course. The components were characterized using the FSLeyes tool from FSL (https://git.fmrib.ox.ac.uk/fsl/fsleyes/fsleyes/) by two independent researchers. One researcher (the author of this thesis) labelled the components that exhibited voxels in the white matter as "signal". The second research (Renate Schweizer) labelled the components that exhibited an upwards shift in the time course across the length of the measurement as "signal". Each of the eight fMRI data sets (two control sessions – with no task, two active sessions - with the Poffenberger task) was denoised in two different ways: once the component with white matter activation maps as the signal and once using the components with the long rising time course as signal. All 16 of the denoised data sets underwent another ICA analysis using MELODIC with the above pre-processing parameters. The resulting components after denoising were visually explored to look for activated voxels in the white matter and/or time courses with a constant increase across the 30 min.

9. PRESENTATION OF DATA

Vessel diameter profiles over time are presented as mean ± SEM. The quantification of the diameter profiles is presented as box plots with the whiskers indicating the maximum and minimum, the central line of the box represents the median, and the mean is shown by a cross symbol.

For most of the data, unless stated otherwise in the figure legend or in the text, data were checked for normality using the Shapiro-Wilk test (Mishra et al., 2019). If all the groups passed the normality test, then an ordinary one-way ANOVA was performed using the minimum possible multiple comparisons needed or an unpaired two-tailed t-test, only if two groups were compared. The specific number of comparisons is indicated in the figure legend or in the text. For the two groups' comparison, variances were compared using an F-test, if they are different, then the Welch correction was used.

If at least one data set did not pass the normality test, then a Kruskal-Wallis test was performed with multiple comparisons, or only if two groups were compared, then a Mann-Whitney test was performed. p-values that are < 0.05 are shown as an exact number unless stated otherwise in the figure legend. All statistics and data representation were performed using GraphPad Prism 9.3.0 (Graphpad Holdings, LLC).

For the fMRI data, the colour code shown in the figures represent the z-statistic. Contrary to p-values, the z-values indicate the number of standard deviations from the mean. The shown values are the default of the fsleyes program. A z-value > 3 represents at least 3 standard deviations from the mean, which in p-values would represent a value < 0.01.

BIBLIOGRAPHY

Alarcon-Martinez, L., Yilmaz-Ozcan, S., Yemisci, M., Schallek, J., Kılıç, K., Can, A., Di Polo, A., and Dalkara, T. (2018). Capillary pericytes express α-smooth muscle actin, which requires prevention of filamentous-actin depolymerization for detection. Elife *7*, 1–17.

Almeida, A., Moncada, S., and Bolaños, J.P. (2004). Nitric oxide switches on glycolysis through the AMP protein kinase and 6-phosphofructo-2-kinase pathway. Nat. Cell Biol. *6*, 45–51.

van Alst, T.M., Wachsmuth, L., Datunashvili, M., Albers, F., Just, N., Budde, T., and Faber, C. (2019). Anesthesia differentially modulates neuronal and vascular contributions to the BOLD signal. Neuroimage *195*, 89–103.

Ances, B.M., Buerk, D.G., Greenberg, J.H., and Detre, J.A. (2001). Temporal dynamics of the partial pressure of brain tissue oxygen during functional forepaw stimulation in rats. Neurosci. Lett. *306*, 106–110.

Armulik, A., Genové, G., Mäe, M., Nisancioglu, M.H., Wallgard, E., Niaudet, C., He, L., Norlin, J., Lindblom, P., Strittmatter, K., et al. (2010). Pericytes regulate the blood-brain barrier. Nature *468*, 557–561.

Arundine, M., and Tymianski, M. (2003). Molecular mechanisms of calcium-dependent neurodegeneration in excitotoxicity. Cell Calcium *34*, 325–337.

Asadollahi, E., Trevisiol, A., Saab, A.S., Looser, Z.J., Dibaj, P., Kusch, K., Ruhwedel, T., Möbius, W., Jahn, O., Baes, M., et al. (2022). Myelin lipids as nervous system energy reserves. BioRxiv 2022.02.24.481621.

Attwell, D., and Iadecola, C. (2002). The neural basis of functional brain imaging signals. Trends Neurosci. *25*, 621–625.

Attwell, D., and Laughlin, S.B. (2001). An energy budget for signaling in the grey matter of the brain. J. Cereb. Blood Flow Metab. *21*, 1133–1145.

Bak, L.K., and Walls, A.B. (2018). Astrocytic glycogen metabolism in the healthy and diseased brain. J. Biol. Chem. *293*, 7108–7116.

Bak, L.K., Walls, A.B., Schousboe, A., Ring, A., Sonnewald, U., and Waagepetersen, H.S. (2009). Neuronal glucose but not lactate utilization is positively correlated with NMDA-induced neurotransmission and fluctuations in cytosolic Ca2+ levels. J. Neurochem. *109*, 87–93.

Ballanyi, K., and Kettenmann, H. (1990). Intracellular Na+ activity in cultured mouse oligodendrocytes. J. Neurosci. Res. *26*, 455–460.

Barbour, B., Brew, H., and Attwell, D. (1988). Electrogenic glutamate uptake in glial cells is activated by intracellular potassium. Nature *335*, 433–435.

Barros, L.F., Courjaret, R., Jakoby, P., Loaiza, A., Lohr, C., and Deitmer, J.W. (2009). Preferential transport and metabolism of glucose in Bergmann glia over Purkinje cells: A multiphoton study of cerebellar slices. Glia *57*, 962–970.

Bean, B.P. (2007). The action potential in mammalian central neurons. Nat. Rev. Neurosci. *8*, 451–465.

Berghoff, S.A., Spieth, L., and Saher, G. (2022). Local cholesterol metabolism orchestrates remyelination. Trends Neurosci. *xx*, 1–12.

Bergles, D.E., Roberts, J.D.B., Somogyi, P., and Jahr, C.E. (2000). Glutamatergic synapses on oligodendrocyte precursor cells in the hippocampus. Nature *405*, 187–191.

Berthiaume, A.A., Hartmann, D.A., Majesky, M.W., Bhat, N.R., and Shih, A.Y. (2018). Pericyte structural remodeling in cerebrovascular health and homeostasis. Front. Aging Neurosci. *10*, 1–12.

Betsholtz, C., and Keller, A. (2014). PDGF, pericytes and the pathogenesis of idiopathic basal ganglia calcification (IBGC). Brain Pathol. *24*, 387–395.

Betsholtz, C., Lindblom, P., and Gerhardt, H. (2005). Role of pericytes in vascular morphogenesis. Vascular *20*, 115–125.

Bonder, D.E., and McCarthy, K.D. (2014). Astrocytic Gq-GPCR-linked IP3R-dependent Ca2+ signaling does not mediate neurovascular coupling in mouse visual cortex in vivo. J. Neurosci. *34*, 13139–13150.

Bottes, S., and Jessberger, S. (2021). Live imaging of remyelination in the adult mouse corpus callosum. Proc. Natl. Acad. Sci. *118*, e2025795118.

Brown, A.M., and Ransom, B.R. (2007). Astrocyte Glycogen and Brain Energy Metabolism. Glia *55*, 1263–1271.

Brown, A.M., Wender, R., and Ransom, B.R. (2001). Metabolic substrates other than glucose support axon function in central white matter. J. Neurosci. Res. *66*, 839–843.

Brown, A.M., Tekkök, S.B., and Ransom, B.R. (2003). Glycogen regulation and functional role in mouse white matter. J. Physiol. *549*, 501–512.

Brown, A.M., Tekkök, S.B., and Ransom, B.R. (2004). Energy transfer from astrocytes to axons: The role of CNS glycogen. Neurochem. Int. *45*, 529–536.

Brown, A.M., Sickmann, H.M., Fosgerau, K., Lund, T.M., Schousboe, A., Waagepetersen, H.S., and Ransom, B.R. (2005). Astrocyte glycogen metabolism is required for neural activity during aglycemia or intense stimulation in mouse white matter. J. Neurosci. Res. *79*, 74–80.

Budday, S., Steinmann, P., and Kuhl, E. (2015). Physical biology of human brain development. Front. Cell. Neurosci. *9*, 1–17.

Butt, A.M., Pugh, M., Hubbard, P., and James, G. (2004). Functions of optic nerve glia: Axoglial signalling in physiology and pathology. Eye *18*, 1110–1121.

Cardozo, P.L., de Lima, I.B.Q., Maciel, E.M.A., Silva, N.C., Dobransky, T., and Ribeiro, F.M. (2019). Synaptic Elimination in Neurological Disorders. Curr. Neuropharmacol. *17*, 1071–1095.

Carmeliet, P., and Jain, R.K. (2011). Molecular mechanisms and clinical applications of angiogenesis. Nature *473*, 298–307.

Cauli, B. (2004). Cortical GABA Interneurons in Neurovascular Coupling: Relays for Subcortical Vasoactive Pathways. J. Neurosci. *24*, 8940–8949.

Cauli, B., and Hamel, E. (2010). Revisiting the role of neurons in neurovascular coupling. Front. Neuroenergetics *2*, 1–8.

Chan, B.S., Endo, S., Kanai, N., and Schuster, V.L. (2002). Identification of lactate as a driving force for prostanoid transport by prostaglandin transporter PGT. Am. J. Physiol. - Ren. Physiol. *282*, 1097–1102.

Chen, C., She, Z., Tang, P., Qin, Z., He, J., and Qu, J.Y. (2021). Study of neurovascular coupling by using mesoscopic and microscopic imaging. IScience *24*, 103176.

Chen, Y., Sobczak, F., Pais-Roldán, P., Schwarz, C., Koretsky, A.P., and Yu, X. (2019). Mapping the brain-wide network effects by optogenetic activation of the corpus callosum. BioRxiv 810366.

Cholet, N., Pellerin, L., Welker, E., Lacombe, P., Seylaz, J., Magistretti, P., and Bonvento, G. (2001). Local injection of antisense oligonucleotides targeted to the glial glutamate transporter GLAST decreases the metabolic response to somatosensory activation. J. Cereb. Blood Flow Metab. *21*, 404–412.

Chong, H.L., and Ruben, P.C. (2008). Interaction between voltage-gated sodium channels and the neurotoxin, tetrodotoxin. Channels *2*, 407–412.

Christ, G.J., Spray, D.C., El-Sabban, M., Moore, L.K., and Brink, P.R. (1996). Gap Junctions in Vascular Tissues. Circ. Res. *79*, 631–646.

Chuquet, J., Quilichini, P., Nimchinsky, E.A., and Buzsáki, G. (2010). Predominant enhancement of glucose uptake in astrocytes versus neurons during activation of the somatosensory cortex. J. Neurosci. *30*, 15298–15303.

Clarke, D.D., and Sokoloff, L. (1999). Circulation and energy metabolism of the brain. In Basic Neurochemistry : Molecular, Cellular and Medical Aspects, G.J. Siegel, ed. (Philadelphia : Lippincott-Raven Publishers), pp. 637–669.

Cooper, M.L., Pasini, S., Lambert, W.S., D'Alessandro, K.B., Yao, V., Risner, M.L., and Calkins, D.J. (2020). Redistribution of metabolic resources through astrocyte networks mitigates neurodegenerative stress. Proc. Natl. Acad. Sci. U. S. A. *117*, 18810–18821.

Courtemanche, M.J., Sparrey, C.J., Song, X., MacKay, A., and D'Arcy, R.C.N. (2018). Detecting white matter activity using conventional 3 Tesla fMRI: An evaluation of standard field strength and hemodynamic response function. Neuroimage *169*, 145–150.

Courtney, M.J., Li, L.-L., and Lai, Y.Y. (2014). Mechanisms of NOS1AP action on NMDA receptor-nNOS signaling. Front. Cell. Neurosci. *8*, 1–7.

Cruz Hernández, J.C., Bracko, O., Kersbergen, C.J., Muse, V., Haft-Javaherian, M., Berg, M., Park, L., Vinarcsik, L.K., Ivasyk, I., Rivera, D.A., et al. (2019). Neutrophil adhesion in brain capillaries reduces cortical blood flow and impairs memory function in Alzheimer's disease mouse models. Nat. Neurosci. *22*, 413–420.

Danbolt, N.C. (2001). Glutamate uptake. Prog. Neurobiol. *65*, 1–105.

Daneman, R., Zhou, L., Kebede, A.A., and Barres, B.A. (2010). Pericytes are required for blood-brain barrier integrity during embryogenesis. Nature *468*, 562–566.

Debernardi, R., Pierre, K., Lengacher, S., Magistretti, P.J., and Pellerin, L. (2003). Cell-specific expression pattern of monocarboxylate transporters in astrocytes and neurons observed in different mouse brain cortical cell cultures. J. Neurosci. Res. *73*, 141–155.

Depp, C., Sun, T., Sasmita, A.O., Spieth, L., Berghoff, S.A., Steixner-Kumar, A.A., Subramanian, S., Möbius, W., Göbbels, S., Saher, G., et al. (2021). Ageing-associated myelin dysfunction drives amyloid deposition in mouse models of Alzheimer's disease. BioRxiv 2021.07.31.454562.

Devor, A., Hillman, E.M.C., Tian, P., Waeber, C., Teng, I.C., Ruvinskaya, L., Shalinsky, M.H., Zhu, H., Haslinger, R.H., Narayanan, S.N., et al. (2008). Stimulus-induced changes in blood flow and 2-deoxyglucose uptake dissociate in ipsilateral somatosensory cortex. J. Neurosci. *28*, 14347–14357.

Devor, A., Sakadžić, S., Saisan, P.A., Yaseen, M.A., Roussakis, E., Srinivasan, V.J., Vinogradov, S.A., Rosen, B.R., Buxton, R.B., Dale, A.M., et al. (2011). "Overshoot" of O2 is required to maintain baseline tissue oxygenation at locations distal to blood vessels. J. Neurosci. *31*, 13676–13681.

Díaz-García, C.M., Meyer, D.J., Nathwani, N., Rahman, M., Martínez-François, J.R., and Yellen, G. (2021). The distinct roles of calcium in rapid control of neuronal glycolysis and the tricarboxylic acid cycle. Elife *10*, 1–30.

Dienel, G.A. (2012). Brain lactate metabolism: The discoveries and the controversies. J. Cereb. Blood Flow Metab. *32*, 1107–1138.

Doll, A., Hölzel, B.K., Boucard, C.C., Wohlschläger, A.M., and Sorg, C. (2015). Mindfulness is associated with intrinsic functional connectivity between default mode and salience networks. Front. Hum. Neurosci. *9*.

Doyle, S., Hansen, D.B., Vella, J., Bond, P., Harper, G., Zammit, C., Valentino, M., and Fern, R. (2018). Vesicular glutamate release from central axons contributes to myelin damage. Nat. Commun. *9*.

Duvernoy, H.M., Delon, S., and Vannson, J.L. (1981). Cortical blood vessels of the human brain. Brain Res. Bull. *7*, 519–579.

Enager, P., Piilgaard, H., Offenhauser, N., Kocharyan, A., Fernandes, P., Hamel, E., and Lauritzen, M. (2009). Pathway-specific variations in neurovascular and neurometabolic coupling in rat primary somatosensory cortex. J. Cereb. Blood Flow Metab. *29*, 976–986.

Felix, L., Delekate, A., Petzold, G.C., and Rose, C.R. (2020). Sodium Fluctuations in Astroglia and Their Potential Impact on Astrocyte Function. Front. Physiol. *11*.

Fernandez-Klett, F., Offenhauser, N., Dirnagl, U., Priller, J., and Lindauer, U. (2010). Pericytes in capillaries are contractile in vivo, but arterioles mediate functional hyperemia in the mouse brain. Proc. Natl. Acad. Sci. *107*, 22290–22295.

Fields, R.D. (2011). Nonsynaptic and nonvesicular ATP release from neurons and relevance to neuron-glia signalling. Semin. Cell Dev. Biol. *22*, 214–219.

Filosa, J.A., Bonev, A.D., Straub, S. V., Meredith, A.L., Wilkerson, M.K., Aldrich, R.W., and Nelson, M.T. (2006). Local potassium signaling couples neuronal activity to vasodilation in the brain. Nat. Neurosci. *9*, 1397–1403.

Fox, P.T., Raichle, M.E., Mintun, M.A., and Dence, C. (1988). Nonoxidative glucose consumption during focal physiologic neural activity. Science *241*, 462–464.

Fraser, L.M., Stevens, M.T., Beyea, S.D., and D'Arcy, R.C.N. (2012). White versus gray matter: fMRI hemodynamic responses show similar characteristics, but differ in peak amplitude. BMC Neurosci. *13*.

Fünfschilling, U., Supplie, L.M., Mahad, D., Boretius, S., Saab, A.S., Edgar, J., Brinkmann, B.G., Kassmann, C.M., Tzvetanova, I.D., Möbius, W., et al. (2012). Glycolytic oligodendrocytes maintain myelin and long-term axonal integrity. Nature *485*, 517–521.

Garthwaite, J., and Boulton, C.L. (1995). Nitric Oxide Signaling in the Central Nervous System. Annu. Rev. Physiol. *57*, 683–706.

Garthwaite, G., Bartus, K., Malcolm, D., Goodwin, D., Kollb-Sielecka, M., Dooldeniya, C., and Garthwaite, J. (2006). Signaling from Blood Vessels to CNS Axons through Nitric Oxide. J. Neurosci. *26*, 7730–7740.

Gawryluk, J.R., Mazerolle, E.L., and D'Arcy, R.C.N. (2014). Does functional MRI detect activation in white matter? A review of emerging evidence, issues, and future directions. Front. Neurosci. *8*, 1–12.

Glück, C., Ferrari, K.D., Binini, N., Keller, A., Saab, A.S., Stobart, J.L., and Weber, B. (2021). Distinct signatures of calcium activity in brain mural cells. Elife *10*, 1–27.

Goldman, S.A., and Kuypers, N.J. (2015). How to make an oligodendrocyte. Dev. *142*, 3983–3995.

Gong, S., Zheng, C., Doughty, M.L., Losos, K., Didkovsky, N., Schambra, U.B., Nowak, N.J., Joyner, A., Leblanc, G., Hatten, M.E., et al. (2003). A gene expression atlas of the central nervous system based on bacterial artificial chromosomes. Nature *425*, 917–925.

Gonzales, A.L., Klug, N.R., Moshkforoush, A., Lee, J.C., Lee, F.K., Shui, B., Tsoukias, N.M., Kotlikoff, M.I., Hill-Eubanks, D., and Nelson, M.T. (2020). Contractile pericytes determine the direction of blood flow at capillary junctions. Proc. Natl. Acad. Sci. U. S. A. *117*, 27022–27033.

Gordon, G.R.J., Choi, H.B., Rungta, R.L., Ellis-Davies, G.C.R., and MacVicar, B.A. (2008). Brain metabolism dictates the polarity of astrocyte control over arterioles. Nature *456*, 745–750.

Grajauskas, L.A., Frizzell, T., Song, X., and D'Arcy, R.C.N. (2019). White Matter fMRI Activation Cannot Be Treated as a Nuisance Regressor: Overcoming a Historical Blind Spot. Front. Neurosci. *13*.

Grant, R.I., Hartmann, D.A., Underly, R.G., Berthiaume, A.A., Bhat, N.R., and Shih, A.Y. (2019). Organizational hierarchy and structural diversity of microvascular pericytes in adult mouse cortex. J. Cereb. Blood Flow Metab. *39*, 411–425.

Greve, D.N., and Fischl, B. (2009). Accurate and robust brain image alignment using boundary-based registration. Neuroimage *48*, 63–72.

Gross, P.M., Sposito, N.M., Pettersen, S.E., and Fenstermacher, J.D. (1986). Differences in function and structure of the capillary endothelium in gray matter, white matter and a circumventricular organ of rat brain. J. Vasc. Res. *23*, 261–270.

Grutzendler, J., and Nedergaard, M. (2019). Cellular Control of Brain Capillary Blood Flow: In Vivo Imaging Veritas. Trends Neurosci. 1–9.

Guo, B., Zhou, F., Li, M., and Gore, J.C. (2022). Latency structure of BOLD signals within white matter in resting-state fMRI. Magn. Reson. Imaging.

Halestrap, A.P. (2012). The monocarboxylate transporter family-Structure and functional characterization. IUBMB Life *64*, 1–9.

Hall, C.N., Reynell, C., Gesslein, B., Hamilton, N.B., Mishra, A., Sutherland, B.A., O'Farrell, F.M., Buchan, A.M., Lauritzen, M., and Attwell, D. (2014). Capillary pericytes regulate cerebral blood flow in health and disease. Nature *508*, 55–60.

Hallmann, R., Horn, N., Selg, M., Wendler, O., Pausch, F., and Sorokin, L.M. (2005). Expression and function of laminins in the embryonic and mature vasculature. Physiol. Rev. *85*, 979–1000.

Hamel, E. (2006). Perivascular nerves and the regulation of cerebrovascular tone. J. Appl. Physiol. *100*, 1059–1064.

Hamilton, N., Vayro, S., Kirchhoff, F., Verkhratsky, A., Robbins, J., Gorecki, D.C., and Butt, A.M. (2008). Mechanisms of ATP- and glutamate-mediated calcium signaling in white matter astrocytes. Glia *56*, 734–749.

Harb, R., Whiteus, C., Freitas, C., and Grutzendler, J. (2013). In vivo imaging of cerebral microvascular plasticity from birth to death. J. Cereb. Blood Flow Metab. *33*, 146–156.

Hariharan, A., Robertson, C.D., Garcia, D.C.G., and Longden, T.A. (2022). Brain Capillary Pericytes are Metabolic Sentinels that Control Blood Flow through K ATP Channel Activity. BioRxiv 1–29.

Harraz, O.F., Longden, T.A., Eubanks, D.H., and Nelson, M.T. (2018). PIP2depletion promotes TRPV4 channel activity in mouse brain capillary endothelial cells. Elife *7*, 1–24.

Harris, J.J., and Attwell, D. (2012). The Energetics of CNS White Matter. J. Neurosci. *32*, 356–371.

Hartmann, D.A., Underly, R.G., Grant, R.I., Watson, A.N., Lindner, V., and Shih, A.Y. (2015). Pericyte structure and distribution in the cerebral cortex revealed by high-resolution imaging of transgenic mice. Neurophotonics *2*, 041402.

Hartmann, D.A., Berthiaume, A.A., Grant, R.I., Harrill, S.A., Koski, T., Tieu, T., McDowell, K.P., Faino, A. V., Kelly, A.L., and Shih, A.Y. (2021). Brain capillary pericytes exert a substantial but slow influence on blood flow. Nat. Neurosci. *24*, 633–645.

Heeger, D.J., and Ress, D. (2002). What does fMRI tell us about neuronal activity? Nat. Rev. Neurosci. *3*, 142–151.

Herard, A.S., Dubois, A., Escartin, C., Tanaka, K., Delzescaux, T., Hantraye, P., and Bonvento, G. (2005). Decreased metabolic response to visual stimulation in the superior colliculus of mice lacking the glial glutamate transporter GLT-1. Eur. J. Neurosci. *22*, 1807–1811.

Herrero-mendez, A., Almeida, A., Fernández, E., Maestre, C., Moncada, S., and Bolaños, J.P. (2009). The bioenergetic and antioxidant status of neurons is controlled by continuous degradation of a key glycolytic enzyme by APC/C – Cdh1. Nat. Cell Biol. *11*, 747–754.

Hill, R.A., Tong, L., Yuan, P., Murikinati, S., Gupta, S., and Grutzendler, J. (2015). Regional Blood Flow in the Normal and Ischemic Brain Is Controlled by Arteriolar Smooth Muscle Cell Contractility and Not by Capillary Pericytes. Neuron *87*, 95–110.

Hillman, E.M.C. (2014). Coupling Mechanism and Significance of the BOLD Signal: A Status Report. Annu. Rev. Neurosci. *37*, 161–181.

Hirrlinger, J., and Nave, K.-A. (2014). Adapting brain metabolism to myelination and long-range signal transduction. Glia *62*, 1749–1761.

Honjin, R., Sakato, S., and Yamashita, T. (1977). Electron Microscopy of the Mouse Optic Nerve : A Quantitative Study of the Total Optic Nerve Fibers. Arch. Histol. Japan *40*, 321–332.

Horiuchi, T., Dietrich, H.H., Hongo, K., and Dacey, R.G. (2002). Mechanism of extracellular K+-induced local and conducted responses in cerebral penetrating arterioles. Stroke *33*, 2692–2699.

Hosford, P.S., and Gourine, A. V. (2019). What is the key mediator of the neurovascular coupling response? Neurosci. Biobehav. Rev. *96*, 174–181.

Howarth, C., Gleeson, P., and Attwell, D. (2012). Updated energy budgets for neural computation in the neocortex and cerebellum. J. Cereb. Blood Flow Metab. *32*, 1222–1232.

Iadecola, C. (2013). The Pathobiology of Vascular Dementia. Neuron *80*, 844–866.

Iadecola, C. (2017). The Neurovascular Unit Coming of Age: A Journey through Neurovascular Coupling in Health and Disease. Neuron *96*, 17–42.

J. Magistretti, P., and Allaman, I. (2016). Brain Energy and Metabolism. In Neuroscience in the 21st Century: From Basic to Clinical, D.W. Pfaff, and N.D. Volkow, eds. (New York, NY:

Springer New York), pp. 1879–1909.

Jabbour, H.N., and Sales, K.J. (2004). Prostaglandin receptor signalling and function in human endometrial pathology. Trends Endocrinol. Metab. *15*, 398–404.

Jenkinson, M., and Smith, S. (2001). A global optimisation method for robust affine registration of brain images. Med. Image Anal. *5*, 143–156.

Jenkinson, M., Bannister, P., Brady, M., and Smith, S. (2002). Improved Optimization for the Robust and Accurate Linear Registration and Motion Correction of Brain Images. Neuroimage *17*, 825–841.

Jenkinson, M., Beckmann, C.F., Behrens, T.E.J., Woolrich, M.W., and Smith, S.M. (2012). FSL. Neuroimage *62*, 782–790.

Ji, X., Ferreira, T., Friedman, B., Liu, R., Liechty, H., Bas, E., Chandrashekar, J., and Kleinfeld, D. (2021). Brain microvasculature has a common topology with local differences in geometry that match metabolic load. Neuron *109*, 1168-1187.e13.

Kadekaro, M., Crane, A.M., and Sokoloff, L. (1985). Differential effects of electrical stimulation of sciatic nerve on metabolic activity in spinal cord and dorsal root ganglion in the rat. Proc. Natl. Acad. Sci. U. S. A. *82*, 6010–6013.

Kanemaru, K., Sekiya, H., Xu, M., Satoh, K., Kitajima, N., Yoshida, K., Okubo, Y., Sasaki, T., Moritoh, S., Hasuwa, H., et al. (2014). In Vivo visualization of subtle, transient, and local activity of astrocytes using an ultrasensitive Ca2+ indicator. Cell Rep. *8*, 311–318.

Kanow, M.A., Giarmarco, M.M., Jankowski, C.S., Tsantilas, K., Engel, A.L., Du, J., Linton, J.D., Farnsworth, C.C., Sloat, S.R., Rountree, A., et al. (2017). Biochemical adaptations of the retina and retinal pigment epithelium support a metabolic ecosystem in the vertebrate eye. Elife *6*.

Kasischke, K.A., Vishwasrao, H.D., Fisher, P.J., Zipfel, W.R., and Webb, W.W. (2004). Neural activity triggers neuronal oxidative metabolism followed by astrocytic glycolysis. Science (80-.). *305*, 99–103.

Kessaris, N., Fogarty, M., Iannarelli, P., Grist, M., Wegner, M., and Richardson, W.D. (2006). Competing waves of oligodendrocytes in the forebrain and postnatal elimination of an embryonic lineage. Nat. Neurosci. *9*, 173–179.

Kirst, C., Skriabine, S., Vieites-Prado, A., Topilko, T., Bertin, P., Gerschenfeld, G., Verny, F., Topilko, P., Michalski, N., Tessier-Lavigne, M., et al. (2020). Mapping the Fine-Scale Organization and Plasticity of the Brain Vasculature. Cell *180*, 780-795.e25.

Kisler, K., Nelson, A.R., Montagne, A., and Zlokovic, B. V. (2017). Cerebral blood flow regulation and neurovascular dysfunction in Alzheimer disease. Nat. Rev. Neurosci. *18*, 419–434.

Kisler, K., Lazic, D., Sweeney, M.D., Plunkett, S., El Khatib, M., Vinogradov, S.A., Boas, D.A., Sakadžić, S., and Zlokovic, B. V. (2018). In vivo imaging and analysis of cerebrovascular hemodynamic responses and tissue oxygenation in the mouse brain. Nat. Protoc. *13*, 1377–1402.

Kisler, K., Nikolakopoulou, A.M., Sweeney, M.D., Lazic, D., Zhao, Z., and Zlokovic, B. V. (2020). Acute Ablation of Cortical Pericytes Leads to Rapid Neurovascular Uncoupling. Front. Cell. Neurosci. *14*.

Knot, H.J., Zimmermann, P.A., and Nelson, M.T. (1996). Extracellular K+-induced hyperpolarizations and dilatations of rat coronary and cerebral arteries involve inward rectifier K+ channels. J. Physiol. *492*, 419–430.

Köhler, S., Winkler, U., and Hirrlinger, J. (2019). Heterogeneity of Astrocytes in Grey and White Matter. Neurochem. Res.

Kovacs-Oller, T., Ivanova, E., Bianchimano, P., and Sagdullaev, B.T. (2020). The pericyte connectome: spatial precision of neurovascular coupling is driven by selective connectivity maps of pericytes and endothelial cells and is disrupted in diabetes. Cell Discov. *6*, 39.

Kukley, M., Capetillo-Zarate, E., and Dietrich, D. (2007). Vesicular glutamate release from axons in white matter. Nat. Neurosci. *10*, 311–320.

Kur, J., and Newman, E.A. (2014). Purinergic control of vascular tone in the retina. J. Physiol. *592*, 491–504.

Kuwabara, T. (1975). Development of the optic nerve of the rat. Invest. Ophthalmol. *14*, 732–745.

Lappe-Siefke, C., Goebbels, S., Gravel, M., Nicksch, E., Lee, J., Braun, P.E., Griffiths, I.R., and Nave, K.-A. (2003). Disruption of Cnp1 uncouples oligodendroglial functions in axonal support and myelination. Nat. Genet. *33*, 366–374.

Laughton, J.D., Bittar, P., Charnay, Y., Pellerin, L., Kovari, E., Magistretti, P.J., and Bouras, C. (2007). Metabolic compartmentalization in the human cortex and hippocampus: Evidence for a cell- and region-specific localization of lactate dehydrogenase 5 and pyruvate dehydrogenase. BMC Neurosci. *8*, 1–6.

Lecoq, J., Tiret, P., Najac, M., Shepherd, G.M., Greer, C.A., and Charpak, S. (2009). Odor-evoked oxygen consumption by action potential and synaptic transmission in the olfactory bulb. J. Neurosci. *29*, 1424–1433.

Lecoq, J., Parpaleix, A., Roussakis, E., Ducros, M., Houssen, Y.G., Vinogradov, S.A., and Charpak, S. (2011). Simultaneous two-photon imaging of oxygen and blood flow in deep cerebral vessels. Nat. Med. *17*, 893–898.

Lee, Y., Morrison, B.M., Li, Y., Lengacher, S., Farah, M.H., Hoffman, P.N., Liu, Y., Tsingalia, A., Jin, L., Zhang, P.-W., et al. (2012). Oligodendroglia metabolically support axons and contribute to neurodegeneration. Nature *487*, 443–448.

Leenders, K.L., Perani, D., Lammertsma, A.A., Heather, J.D., Buckingham, P., Jones, T., Healy, M.J.R., Gibbs, J.M., Wise, R.J.S., Hatazawa, J., et al. (1990). Cerebral blood flow, blood volume and oxygen utilization: Normal values and effect of age. Brain *113*, 27–47.

Lemaistre, J.L., Sanders, S.A., Stobart, M.J., Lu, L., Knox, J.D., Anderson, H.D., and Anderson, C.M. (2012). Coactivation of NMDA receptors by glutamate and D-serine induces dilation of isolated middle cerebral arteries. J. Cereb. Blood Flow Metab. *32*, 537–547.

Leybaert, L. (2005). Neurobarrier coupling in the brain: A partner of neurovascular and neurometabolic coupling? J. Cereb. Blood Flow Metab. *25*, 2–16.

Leybaert, L., De Bock, M., Van Moorhem, M., Decrock, E., and De Vuyst, E. (2007). Neurobarrier coupling in the brain: Adjusting glucose entry with demand. J. Neurosci. Res. *85*, 3213–3220.

Li, C.H., and Tam, P.K.S. (1998). An iterative algorithm for minimum cross entropy thresholding. Pattern Recognit. Lett. *19*, 771–776.

Li, B., Ohtomo, R., Thunemann, M., Adams, S.R., Yang, J., Fu, B., Yaseen, M.A., Ran, C., Polimeni, J.R., Boas, D.A., et al. (2019a). Two-photon microscopic imaging of capillary red blood cell flux in mouse brain reveals vulnerability of cerebral white matter to hypoperfusion. J. Cereb. Blood Flow Metab. 1–12.

Li, M., Newton, A.T., Anderson, A.W., Ding, Z., and Gore, J.C. (2019b). Characterization of the hemodynamic response function in white matter tracts for event-related fMRI. Nat. Commun. *10*, 1–11.

Li, M., Gao, Y., Anderson, A.W., Ding, Z., and Gore, J.C. (2021). Dynamic variations of resting - state BOLD signal spectra in white matter. BioRxiv *1*.

Li, Z., Okamoto, K.-I., Hayashi, Y., and Sheng, M. (2004). The importance of dendritic mitochondria in the morphogenesis and plasticity of spines and synapses. Cell *119*, 873–887.

Lind, B.L., Brazhe, A.R., Jessen, S.B., Tan, F.C.C., and Lauritzen, M.J. (2013). Rapid stimulus-evoked astrocyte Ca2+ elevations and hemodynamic responses in mouse somatosensory cortex in vivo. Proc. Natl. Acad. Sci. U. S. A. *110*, E4678-87.

Lindauer, U., Leithner, C., Kaasch, H., Rohrer, B., Foddis, M., Füchtemeier, M., Offenhauser, N., Steinbrink, J., Royl, G., Kohl-Bareis, M., et al. (2010). Neurovascular coupling in rat brain operates independent of hemoglobin deoxygenation. J. Cereb. Blood Flow Metab. *30*, 757–768.

Logothetis, N.K., Pauls, J., Augath, M., Trinath, T., and Oeltermann, A. (2001). Neurophysiological investigation of the basis of the fMRI signal. Nature *412*, 150–157.

Longden, T.A., and Nelson, M.T. (2015). Vascular inward rectifier K+ channels as external K+ sensors in the control of cerebral blood flow. Microcirculation *22*, 183–196.

Longden, T.A., and Nelson, M.T. (2016). Vascular Inward Rectifier K+ channels as External K+ Sensors in the Control of Cerebral Blood Flow. Microcirculation *22*, 183–196.

Longden, T.A., Dabertrand, F., Koide, M., Gonzales, A.L., Tykocki, N.R., Brayden, J.E., Hill-Eubanks, D., and Nelson, M.T. (2017). Capillary K+-sensing initiates retrograde hyperpolarization to increase local cerebral blood flow. Nat. Neurosci. *20*, 717–726.

Longden, T.A., Mughal, A., Hennig, G.W., Harraz, O.F., Shui, B., Lee, F.K., Lee, J.C., Reining, S., Kotlikoff, M.I., König, G.M., et al. (2021). Local IP3 receptor-mediated Ca2+ signals compound to direct blood flow in brain capillaries. Sci. Adv. *7*.

Lücker, A., Weber, B., and Jenny, P. (2015). A dynamic model of oxygen transport from capillaries to tissue with moving red blood cells. Am. J. Physiol. - Hear. Circ. Physiol. *308*, H206–H216.

Luders, E., Thompson, P.M., and Toga, A.W. (2010). The Development of the Corpus Callosum in the Healthy Human Brain. J. Neurosci. *30*, 10985–10990.

Ludmer, P.L., Selwyn, A.P., Shook, T.L., Wayne, R.R., Mudge, G.H., Alexander, R.W., and Ganz, P. (1986). Paradoxical vasoconstriction induced by acetylcholine in artherosclerotic coronary arteries. N. Engl. J. Med. *315*, 1046–1051.

Lundgaard, I., Osório, M.J., Kress, B.T., Sanggaard, S., and Nedergaard, M. (2014). White matter astrocytes in health and disease. Neuroscience *276*, 161–173.

Mächler, P., Wyss, M.T., Elsayed, M., Stobart, J., Gutierrez, R., Von Faber-Castell, A., Kaelin, V., Zuend, M., San Martín, A., Romero-Gómez, I., et al. (2016). In Vivo Evidence for a Lactate Gradient from Astrocytes to Neurons. Cell Metab. *23*, 94–102.

Magistretti, P.J., and Chatton, J.Y. (2005). Relationship between L-glutamate-regulated intracellular Na+ dynamics and ATP hydrolysis in astrocytes. J. Neural Transm. *112*, 77–85.

Mangia, S., Simpson, I.A., Vannucci, S.J., and Carruthers, A. (2009). The in vivo neuron-to-astrocyte lactate shuttle in human brain: Evidence from modeling of measured lactate levels during visual stimulation. J. Neurochem. *109*, 55–62.

Manicam, C., Staubitz, J., Brochhausen, C., Grus, F.H., Pfeiffer, N., and Gericke, A. (2016). The Gatekeepers in the Mouse Ophthalmic Artery: Endothelium-Dependent Mechanisms of Cholinergic Vasodilation. Sci. Rep. *6*, 1–13.

Marzi, C.A. (1999). The Poffenberger paradigm: a first, simple, behavioural tool to study interhemispheric transmission in humans. Brain Res. Bull. *50*, 421–422.

Mazerolle, E.L., D'Arcy, R.C.N., and Beyea, S.D. (2008). Detecting functional magnetic resonance imaging activation in white matter: Interhemispheric transfer across the corpus callosum. BMC Neurosci. *9*, 1–11.

Meijering, E., Jacob, M., Sarria, J.-C.F., Steiner, P., Hirling, H., and Unser, M. (2004). Design and validation of a tool for neurite tracing and analysis in fluroescence microscopy images. Cytom. Part A *58A*, 167–176.

Meyer, N., Richter, N., Fan, Z., Siemonsmeier, G., Pivneva, T., Jordan, P., Steinhäuser, C., Semtner, M., Nolte, C., and Kettenmann, H. (2018). Oligodendrocytes in the Mouse Corpus Callosum Maintain Axonal Function by Delivery of Glucose. Cell Rep. *22*, 2455–2468.

Micu, I., Ridsdale, A., Zhang, L., Woulfe, J., McClintock, J., Brantner, C.A., Andrews, S.B., and Stys, P.K. (2007). Real-time measurement of free Ca2+ changes in CNS myelin by two-photon microscopy. Nat. Med. *13*, 874–879.

Micu, I., Plemel, J.R., Lachance, C., Proft, J., Jansen, A.J., Cummins, K., van Minnen, J., and Stys, P.K. (2016). The molecular physiology of the axo-myelinic synapse. Exp. Neurol. *276*, 41–50.

Micu, I., Plemel, J.R., Caprariello, A. V., Nave, K.-A., and Stys, P.K. (2018). Axo-myelinic neurotransmission: A novel mode of cell signalling in the central nervous system. Nat. Rev. Neurosci. *19*, 49–57.

Millecamps, S., and Julien, J.P. (2013). Axonal transport deficits and neurodegenerative diseases. Nat. Rev. Neurosci. *14*, 161–176.

Mishra, A., Hamid, A., and Newman, E.A. (2011). Oxygen modulation of neurovascular coupling in the retina. Proc. Natl. Acad. Sci. *108*, 17827–17831.

Mishra, A., O'Farrell, F.M., Reynell, C., Hamilton, N.B., Hall, C.N., and Attwell, D. (2014). Imaging pericytes and capillary diameter in brain slices and isolated retinae. Nat. Protoc. *9*, 323–336.

Mishra, A., Reynolds, J.P., Chen, Y., Gourine, A. V., Rusakov, D.A., and Attwell, D. (2016). Astrocytes mediate neurovascular signaling to capillary pericytes but not to arterioles. Nat. Neurosci. *19*, 1619–1627.

Mishra, P., Pandey, C.M., Singh, U., Gupta, A., Sahu, C., and Keshri, A. (2019). Descriptive statistics and normality tests for statistical data. Ann. Card. Anaesth. *22*, 67–72.

Molyneaux, B.J., Arlotta, P., Menezes, J.R.L., and Macklis, J.D. (2007). Neuronal subtype specification in the cerebral cortex. Nat. Rev. Neurosci. *8*, 427–437.

Montagne, A., Nikolakopoulou, A.M., Zhao, Z., Sagare, A.P., Si, G., Lazic, D., Barnes, S.R., Daianu, M., Ramanathan, A., Go, A., et al. (2018). Pericyte degeneration causes white matter dysfunction in the mouse central nervous system. Nat. Med. *24*, 326–337.

Mullershausen, F., Lange, A., Mergia, E., Friebe, A., and Koesling, D. (2006). Desensitization of NO / cGMP Signaling in Smooth Muscle : Blood Vessels Versus Airways. Mol. Pharmacol. *69*, 1969–1974.

Mullis, K., Faloona, F., Scharf, S., Saiki, R., Horn, G., and Erlich, H. (1986). Specific enzymatic amplification of DNA in vitro: the polymerase chain reaction. Cold Spring Harb.

Symp. Quant. Biol. *LI*, 263–273.

Nave, K.-A. (2010). Myelination and the trophic support of long axons. Nat. Rev. Neurosci. *11*, 275–283.

Nave, K.-A., and Trapp, B.D. (2008). Axon-Glial Signaling and the Glial Support of Axon Function. Annu. Rev. Neurosci. *31*, 535–561.

Nave, K.-A., and Werner, H.B. (2014). Myelination of the Nervous System: Mechanisms and Functions. Annu. Rev. Cell Dev. Biol. *30*, 503–533.

Nehlig, A., Wittendorp-Rechenmann, E., and Lam, C.D. (2004). Selective uptake of [14c]2-deoxyglucose by neurons and astrocytes: High-resolution microautoradiographic imaging by cellular 14C-trajectography combined with immunohistochemistry. J. Cereb. Blood Flow Metab. *24*, 1004–1014.

Nizar, K., Uhlirova, H., Tian, P., Saisan, P.A., Cheng, Q., Reznichenko, L., Weldy, K.L., Steed, T.C., Sridhar, V.B., MacDonald, C.L., et al. (2013). In vivo Stimulus-Induced Vasodilation Occurs without IP3 Receptor Activation and May Precede Astrocytic Calcium Increase. J. Neurosci. *33*, 8411–8422.

Offenhauser, N., Thomsen, K., Caesar, K., and Lauritzen, M. (2005). Activity-induced tissue oxygenation changes in rat cerebellar cortex: interplay of postsynaptic activation and blood flow. J. Physiol. *565*, 279–294.

Ogawa, S., Lee, T.M., Kay, A.R., and Tank, D.W. (1990). Brain magnetic resonance imaging with contrast dependent on blood oxygenation. Proc. Natl. Acad. Sci. U. S. A. *87*, 9868–9872.

De Oliveira, F. (1966). Pericytes in diabetic retinopathy. Br. J. Opthalmology *50*, 134–143.

Olthof, B.M., Gartside, S.E., and Rees, A. (2018). Puncta of neuronal nitric oxide synthase (nNOS) mediate NMDA-receptor signalling in the auditory midbrain. J. Neurosci. *39*, 876–887.

Orentas, D.M., Hayes, J.E., Dyer, K.L., and Miller, R.H. (1999). Sonic hedgehog signaling is required during the appearance of spinal cord oligodendrocyte precursors. Development *126*, 2419–2429.

Orthmann-Murphy, J.L., Abrams, C.K., and Scherer, S.S. (2008). Gap junctions couple astrocytes and oligodendrocytes. J. Mol. Neurosci. *35*, 101–116.

Otsu, Y., Couchman, K., Lyons, D.G., Collot, M., Agarwal, A., Mallet, J.M., Pfrieger, F.W., Bergles, D.E., and Charpak, S. (2015). Calcium dynamics in astrocyte processes during neurovascular coupling. Nat. Neurosci. *18*, 210–218.

Ouardouz, M., Nikolaeva, M.A., Coderre, E., Zamponi, G.W., McRory, J.E., Trapp, B.D., Yin, X., Wang, W., Woulfe, J., and Stys, P.K. (2003). Depolarization-Induced Ca2+ Release in Ischemic Spinal Cord White Matter Involves L-type Ca2+ Channel Activation of Ryanodine Receptors. Neuron *40*, 53–63.

Pariyadath, V., Stein, E.A., and Ross, T.J. (2014). Machine learning classification of resting state functional connectivity predicts smoking status. Front. Hum. Neurosci. *8*, 425.

Parpaleix, A., Houssen, Y.G., and Charpak, S. (2013). Imaging local neuronal activity by monitoring PO2 transients in capillaries. Nat. Med. *19*, 241–246.

Patel, A.B., Lai, J.C.K., Chowdhury, G.M.I., Hyder, F., Rothman, D.L., Shulman, R.G., and Behar, K.L. (2014). Direct evidence for activity-dependent glucose phosphorylation in neurons with implications for the astrocyte-to-neuron lactate shuttle. Proc. Natl. Acad. Sci. U. S. A. *111*, 5385–5390.

Pellerin, L., and Magistretti, P.J. (1994). Glutamate uptake into astrocytes stimulates aerobic glycolysis: A mechanism coupling neuronal activity to glucose utilization. Proc. Natl. Acad. Sci. U. S. A. *91*, 10625–10629.

Perge, J.A., Koch, K., Miller, R., Sterling, P., and Balasubramanian, V. (2009). How the optic nerve allocates space, energy capacity, and information. J. Neurosci. *29*, 7917–7928.

Philippot, C., Griemsmann, S., Jabs, R., Seifert, G., Kettenmann, H., and Steinhäuser, C. (2021). Astrocytes and oligodendrocytes in the thalamus jointly maintain synaptic activity by supplying metabolites. Cell Rep. *34*.

Porras, O.H., Loaiza, A., and Felipe Barros, L. (2004). Glutamate mediates acute glucose transport inhibition in hippocampal neurons. J. Neurosci. *24*, 9669–9673.

Porras, O.H., Ruminot, I., Loaiza, A., and Barros, L.F. (2008). Na(+)-Ca(2+) cosignaling in the stimulation of the glucose transporter GLUT1 in cultured astrocytes. Glia *56*, 59–68.

Powers, W.J., Hirsch, I.B., and Cryer, P.E. (1996). Effect of stepped hypoglycemia on regional cerebral blood flow response to physiological brain activation. Am. J. Physiol. *270*, H554-9.

Rich, L.R., Harris, W., and Brown, A.M. (2019). The Role of Brain Glycogen in Supporting Physiological Function. Front. Neurosci. *13*.

Richmond, T.S. (1997). Cerebral resuscitation after global brain ischemia: Linking research to practice. AACN Adv. Crit. Care *8*, 171–181.

Roche, M., Chaigneau, E., Rungta, R.L., Boido, D., Weber, B., and Charpak, S. (2019). In vivo imaging with a water immersion objective affects brain temperature, blood flow and oxygenation. Elife *8*, 1–12.

Rolfes, L., Riek-Burchardt, M., Pawlitzki, M., Minnerup, J., Bock, S., Schmidt, M., Meuth, S.G., Gunzer, M., and Neumann, J. (2021). Neutrophil granulocytes promote flow stagnation due to dynamic capillary stalls following experimental stroke. Brain. Behav. Immun. *93*, 322–330.

Rose, C.R., and Chatton, J.Y. (2016). Astrocyte sodium signaling and neuro-metabolic coupling in the brain. Neuroscience *323*, 121–134.

Rouach, N., Koulakoff, A., Abudara, V., Willecke, K., and Giaume, C. (2008). Hippocampal Synaptic Transmission. Science *322*, 1551–1555.

Rowitch, D.H., and Kriegstein, A.R. (2010). Developmental genetics of vertebrate glial-cell specification. Nature *468*, 214–222.

Roy, B., and Garthwaite, J. (2006). Nitric oxide activation of guanylyl cyclase in cells revisited. Proc. Natl. Acad. Sci. U. S. A. *103*, 12185–12190.

Rungta, R.L., Zuend, M., Aydin, A.K., Martineau, É., Boido, D., Weber, B., and Charpak, S. (2021). Diversity of neurovascular coupling dynamics along vascular arbors in layer II/III somatosensory cortex. Commun. Biol. *4*.

Saab, A.S., Tzvetavona, I.D., Trevisiol, A., Baltan, S., Dibaj, P., Kusch, K., Möbius, W., Goetze, B., Jahn, H.M., Huang, W., et al. (2016). Oligodendroglial NMDA Receptors Regulate Glucose Import and Axonal Energy Metabolism. Neuron *91*, 119–132.

Sawada, K., Echigo, N., Juge, N., Miyaji, T., Otsuka, M., Omote, H., Yamamoto, A., and Moriyama, Y. (2008). Identification of a vesicular nucleotide transporter. Proc. Natl. Acad. Sci. U. S. A. *105*, 5683–5686.

Schaeffer, S., and Iadecola, C. (2021). Revisiting the neurovascular unit. Nat. Neurosci. *24*, 1198–1209.

Schaffenrath, J., Huang, S.F., Wyss, T., Delorenzi, M., and Keller, A. (2021). Characterization of the blood–brain barrier in genetically diverse laboratory mouse strains. Fluids Barriers CNS *18*, 1–15.

Schiller, J., Schiller, Y., and Clapham, D.E. (1998). Amplification of calcium influx into dendritic spines during associative pre- and postsynaptic activation: the role of direct calcium influx through the NMDA receptor. Nat. Neurosci. *1*, 114–118.

Schindelin, J., Arganda-Carreras, I., Frise, E., Kaynig, V., Longair, M., Pietzsch, T., Preibisch, S., Rueden, C., Saalfeld, S., Schmid, B., et al. (2012). Fiji: An open-source platform for biological-image analysis. Nat. Methods *9*, 676–682.

Schulz, K., Sydekum, E., Krueppel, R., Engelbrecht, C.J., Schlegel, F., Schröter, A., Rudin, M., and Helmchen, F. (2012). Simultaneous BOLD fMRI and fiber-optic calcium recording in rat neocortex. Nat. Methods *9*, 597–602.

Seager, R., Lee, L., Henley, J.M., and Wilkinson, K.A. (2020). Mechanisms and roles of mitochondrial localisation and dynamics in neuronal function. Neuronal Signal. *4*, NS20200008.

Sefton, A.J., Horsburgh, G.M., and Lam, K. (1985). The Development of the Optic Nerve in Rodents. Aust. N. Z. J. Ophthalmol. *13*, 135–145.

Shaw, K., Bell, L., Boyd, K., Grijseels, D.M., Clarke, D., Bonnar, O., Crombag, H.S., and Hall, C.N. (2021). Neurovascular coupling and oxygenation are decreased in hippocampus compared to neocortex because of microvascular differences. Nat. Commun. *12*, 1–16.

Shigetomi, E., Kracun, S., Sofroniew, M. V, and Khakh, B.S. (2010). A genetically targeted optical sensor to monitor calcium signals in astrocyte processes. Nat. Neurosci. *13*, 759–766.

Shih, A.Y., Driscoll, J.D., Drew, P.J., Nishimura, N., Schaffer, C.B., and Kleinfeld, D. (2012). Two-photon microscopy as a tool to study blood flow and neurovascular coupling in the rodent brain. J. Cereb. Blood Flow Metab. *32*, 1277–1309.

Siegenthaler, J.A., Choe, Y., Patterson, K.P., Hsieh, I., Li, D., Jaminet, S.C., Daneman, R., Kume, T., Huang, E.J., and Pleasure, S.J. (2013). Foxc1 is required by pericytes during fetal brain angiogenesis. Biol Open *2*, 647–659.

Smith, S.M. (2002). Fast robust automated brain extraction. Hum. Brain Mapp. *17*, 143–155.

Smith, S.M., Jenkinson, M., Woolrich, M.W., Beckmann, C.F., Behrens, T.E.J., Johansen-Berg, H., Bannister, P.R., De Luca, M., Drobnjak, I., Flitney, D.E., et al. (2004). Advances in functional and structural MR image analysis and implementation as FSL. Neuroimage *23*, S208–S219.

Sokoloff, L. (1992). The brain as a chemical machine. Prog. Brain Res. *94*, 19–33.

Sotelo-Hitschfeld, T., Niemeyer, M.I., Mächler, P., Ruminot, I., Lerchundi, R., Wyss, M.T., Stobart, J., Fernández-Moncada, I., Valdebenito, R., Garrido-Gerter, P., et al. (2015). Channel-mediated lactate release by K+ -stimulated astrocytes. J. Neurosci. *35*, 4168–4178.

Srinivasan, R., Huang, B.S., Venugopal, S., Johnston, A.D., Chai, H., Zeng, H., Golshani, P., and Khakh, B.S. (2015). Ca(2+) signaling in astrocytes from Ip3r2(-/-) mice in brain slices and during startle responses in vivo. Nat. Neurosci. *18*, 708–717.

Stobart, J.L.L., Lu, L., Anderson, H.D.I., Mori, H., and Anderson, C.M. (2013). Astrocyte-induced cortical vasodilation is mediated by D-serine and endothelial nitric oxide synthase. Proc. Natl. Acad. Sci. *110*, 3149–3154.

Stratman, A.N., and Davis, G.E. (2012). Endothelial cell-pericyte interactions stimulate basement membrane matrix assembly: influence on vascular tube remodeling, maturation, and stabilization. Microsc. Microanal. *18*, 68–80.

Stumpf, S.K., Berghoff, S.A., Trevisiol, A., Spieth, L., Düking, T., Schneider, L. V., Schlaphoff, L., Dreha-Kulaczewski, S., Bley, A., Burfeind, D., et al. (2019). Ketogenic diet ameliorates axonal defects and promotes myelination in Pelizaeus–Merzbacher disease. Acta Neuropathol. *138*, 147–161.

Sturrock, R.R. (1980). Myelination of the Mouse Corpus Callosum. Neuropathol. Appl. Neurobiol. *6*, 415–420.

Stys, P.K., Ransom, B.R., and Waxman, S.G. (1991). Compound action potential of nerve recorded by suction electrode: a theoretical and experimental analysis. Brain Res. *546*, 18–32.

Südhof, T.C. (2012). Calcium control of neurotransmitter release. Cold Spring Harb. Perspect. Biol. *4*.

Suh, S.W., Hamby, A.M., and Swanson, R.A. (2007). Hypoglycemia, Brain Energetics, and Hypoglycemic Neuronal Death. Glia *55*, 1280–1286.

Sweeney, P.W., Walker-Samuel, S., and Shipley, R.J. (2018). Insights into cerebral haemodynamics and oxygenation utilising in vivo mural cell imaging and mathematical modelling. Sci. Rep. *8*, 1–15.

Takano, T., He, W., Han, X., Wang, F., Xu, Q., Wang, X., Oberheim Bush, N.A., Cruz, N., Dienel, G.A., and Nedergaard, M. (2014). Rapid manifestation of reactive astrogliosis in acute hippocampal brain slices. Glia *62*, 78–95.

Tekkök, S.B., Brown, A.M., Westenbroek, R., Pellerin, L., and Ransom, B.R. (2005). Transfer of glycogen-derived lactate from astrocytes to axons via specific monocarboxylate transporters supports mouse optic nerve activity. J. Neurosci. Res. *81*, 644–652.

Tettamanti, M., Paulesu, E., Scifo, P., Maravita, A., Fazio, F., Perani, D., and Marzi, C.A. (2002). Interhemispheric transmission of visuomotor information in humans: fMRI evidence. J. Neurophysiol. *88*, 1051–1058.

Thévenaz, P., Ruttimann, U.E., and Unser, M. (1998). A pyramid approach to subpixel registration based on intensity. IEEE Trans. Image Process. *7*, 27–41.

Tischbirek, C.H., Birkner, A., and Konnerth, A. (2017). In vivo deep two-photon imaging of neural circuits with the fluorescent Ca2+ indicator Cal-590. J. Physiol. *595*, 3097–3105.

Trevisiol, A., Saab, A.S., Winkler, U., Marx, G., Imamura, H., Möbius, W., Kusch, K., Nave, K.-A., and Hirrlinger, J. (2017). Monitoring ATP dynamics in electrically active white matter tracts. Elife *6*, 1–17.

Tsai, H.H., Niu, J., Munji, R., Davalos, D., Chang, J., Zhang, H., Tien, A.C., Kuo, C.J., Chan, J.R., Daneman, R., et al. (2016). Oligodendrocyte precursors migrate along vasculature in the developing nervous system. Science (80-.). *351*, 379–384.

Tsai, P.S., Kaufhold, J.P., Blinder, P., Friedman, B., Drew, P.J., Karten, H.J., Lyden, P.D., and Kleinfeld, D. (2009). Correlations of neuronal and microvascular densities in murine cortex revealed by direct counting and colocalization of nuclei and vessels. J. Neurosci. *29*, 14553–14570.

Tsien, J.Z., Huerta, P.T., and Tonegawa, S. (1996). The essential role of hippocampal CA1

NMDA receptor-dependent synaptic plasticity in spatial memory. Cell *87*, 1327–1338.

Vane, J.R., Bakhle, Y.S., and Botting, R.M. (1998). Cyclooxygenases 1 and 2. Annu. Rev. Pharmacol. Toxicol. *38*, 97–120.

Vanlandewijck, M., He, L., Mäe, M.A., Andrae, J., Ando, K., Del Gaudio, F., Nahar, K., Lebouvier, T., Laviña, B., Gouveia, L., et al. (2018). A molecular atlas of cell types and zonation in the brain vasculature. Nature *554*, 475–480.

Vasudevan, A., Long, J.E., Crandall, J.E., Rubenstein, J.L.R., and Bhide, P.G. (2008). Compartment-specific transcription factors orchestrate angiogenesis gradients in the embryonic brain. Nat. Neurosci. *11*, 429–439.

Wahl, M., Lauterbach-Soon, B., Hattingen, E., Jung, P., Singer, O., Volz, S., Klein, J.C., Steinmetz, H., and Ziemann, U. (2007). Human motor corpus callosum: Topography, somatotopy, and link between microstructure and function. J. Neurosci. *27*, 12132–12138.

Wakhloo, D., Scharkowski, F., Curto, Y., Javed Butt, U., Bansal, V., Steixner-Kumar, A.A., Wüstefeld, L., Rajput, A., Arinrad, S., Zillmann, M.R., et al. (2020). Functional hypoxia drives neuroplasticity and neurogenesis via brain erythropoietin. Nat. Commun. *11*, 1–12.

Wang, Y., Fathali, H., Mishra, D., Olsson, T., Keighron, J.D., Skibicka, K.P., and Cans, A.-S. (2019). Counting the Number of Glutamate Molecules in Single Synaptic Vesicles. J. Am. Chem. Soc. *141*, 17507–17511.

Waters, J.C. (2009). Accuracy and precision in quantitative fluorescence microscopy. J. Cell Biol. *185*, 1135–1148.

Waxman, S.G. (1997). Axon-glia interactions: Building a smart nerve fiber. Curr. Biol. *7*, R406–R410.

Webb, R.C. (2003). Smooth muscle contraction and relaxation. Am. J. Physiol. - Adv. Physiol. Educ. *27*, 201–206.

Weber, B., Treyer, V., Oberholzer, N., Jaermann, T., Boesiger, P., Brugger, P., Regard, M., Buck, A., Savazzi, S., and Marzi, C.A. (2005). Attention and interhemispheric transfer: a behavioral and fMRI study. J. Cogn. Neurosci. *17*, 113–123.

Wei, H.S., Kang, H., Rasheed, I.Y.D., Zhou, S., Lou, N., Gershteyn, A., McConnell, E.D., Wang, Y., Richardson, K.E., Palmer, A.F., et al. (2016). Erythrocytes Are Oxygen-Sensing Regulators of the Cerebral Microcirculation. Neuron *91*, 851–862.

Wolf, T., Lindauer, U., Villringer, A., and Dirnagl, U. (1997). Excessive oxygen or glucose supply does not alter the blood flow response to somatosensory stimulation or spreading depression in rats. Brain Res. *761*, 290–299.

Xia, C.Y., Xu, J.K., Pan, C.H., Lian, W.W., Yan, Y., Ma, B.Z., He, J., and Zhang, W.K. (2020). Connexins in oligodendrocytes and astrocytes: Possible factors for demyelination in multiple sclerosis. Neurochem. Int. *136*, 104731.

Xie, H., Chung, D.Y., Kura, S., Sugimoto, K., Aykan, S.A., Wu, Y., Sakadžić, S., Yaseen, M.A., Boas, D.A., and Ayata, C. (2019). Differential effects of anesthetics on resting state functional connectivity in the mouse. J. Cereb. Blood Flow Metab.

Yamada, M., Lamping, K.G., Duttaroy, A., Zhang, W., Cui, Y., Bymaster, F.P., McKinzie, D.L., Felder, C.C., Deng, C.X., Faraci, F.M., et al. (2001). Cholinergic dilation of cerebral blood vessels is abolished in M(5) muscarinic acetylcholine receptor knockout mice. Proc. Natl. Acad. Sci. U. S. A. *98*, 14096–14101.

Yellen, G. (2018). Fueling thought: Management of glycolysis and oxidative phosphorylation in neuronal metabolism. J. Cell Biol. *217*, 2235–2246.

Yu, Y., Herman, P., Rothman, D.L., Agarwal, D., and Hyder, F. (2018). Evaluating the gray and white matter energy budgets of human brain function. J. Cereb. Blood Flow Metab. *38*, 1339–1353.

Zeller, K., Rahner-welsch, S., and Kuschinsky, W. (1997). Distribution of Glutl Glucose Transporters in Different Brain Structures Compared to Glucose Utilization and Capillary Density of Adult Rat Brains. Blood 204–209.

Zhang, D., Liang, B., Wu, X., Wang, Z., Xu, P., Chang, S., Liu, B., Liu, M., and Huang, R. (2015). Directionality of large-scale resting-state brain networks during eyes open and eyes closed conditions. Front. Hum. Neurosci. *9*.

Ziemens, D., Oschmann, F., Gerkau, N.J., and Rose, C.R. (2019). Heterogeneity of Activity-Induced Sodium Transients between Astrocytes of the Mouse Hippocampus and Neocortex: Mechanisms and Consequences. J. Neurosci. *39*, 2620 LP – 2634.

Zimmermann, K.W. (1923). Der Feinere Bau der Blutcapillaren (Springer-Verlag GmbH Berlin Heidelberg 1923).

Ziskin, J.L., Nishiyama, A., Rubio, M., Fukaya, M., and Bergles, D.E. (2007). Vesicular release of glutamate from unmyelinated axons in white matter. Nat. Neurosci. *10*, 321–330.

Zonta, M., Angulo, M.C., Gobbo, S., Rosengarten, B., Hossmann, K.-A., Pozzan, T., and Carmignoto, G. (2003). Neuron-to-astrocyte signaling is central to the dynamic control of brain microcirculation. Nat. Neurosci. *6*, 43–50.

APPENDIX

1. CAP ANALYSIS SCRIPT

```matlab
%% script to analyze and plot CAP by Andrea. Script works on .mat exported data from Patchmaster v2.9x

% data can be exported from both channels (I-mon should be channel-1, V-mon on channel 2).
% if only one channel, *A/D is found, value of pre-amplification used is required.

% the script uses .1 - .9 ms as range for waveform offset & automatically detects the range for integration of the CAP area by:
% 1) calculating the mean of the baseline waveforms
% 2a) using the prompt 'end of stim' [ms] to detect the beginning of the evoked CAP on the average waveforms
% 2b) if the rise of the evoked CAP response cannot be found, the user is required to add it manually by inserting a datatip to determine the left range for integration
% 3) using the peak latency of the baseline multiplied by a factor, e.g. 125%, to set the right end of the integration

% range for calc of peak amplitude and latency has to be inserted manually by adding two datatips that determine the range where to find the waveform MAX

% the script will output the analyzed data as .xlsx in the subfolder 'Analysis' along with the final figure and the variables used for analysis
% The script won't run on exported data which might contain traces with both,one AND two channels, hence export only one type of data at time

clear all; clc
[FileName,PathName] = uigetfile('*.mat','Select the MATLAB code file');
[~,NameNoExt,Ext] = fileparts(FileName);
ScriptFolder = cd(PathName);
S = load(fullfile(PathName,FileName));
off1 = 0.1;
off2 = 0.9;
Pix_SS = get(0,'screensize');
fig_ysize = 0.8;
fig1=figure('Name',NameNoExt,...
    'Color', [0.99 0.99 0.99],...
    'Position', [0 round((Pix_SS(1,4)*(1-fig_ysize))) Pix_SS(1,3) round((Pix_SS(1,4)*fig_ysize))],...
    'Units', 'pixels',...
    'NumberTitle','off');
title('CAP');
%% separate channels
Ch1 = struct;
```

```
Ch2 = struct;
for f = fieldnames(S)'
    if str2num(f{1}(end)) == 1
        Ch1.(f{1}) = S.(f{1});
    elseif str2num(f{1}(end)) == 2
        Ch2.(f{1}) = S.(f{1});
    end
end
f = fieldnames(S)';
t0 = S.(char(f(1,1)))(1,1);
check = fieldnames(Ch2);
TF = double(isempty(check));
switch TF
    case 1
        prompt={'AD-channel! enter value for signal amplification used:',...
            'end of stimulation (ms)'...
            'Select baseline number of traces:',...
            'Enter right cut-off range for integration (n x peak latency):'};
        name = 'Amplification';
        defaultans = {'500','1.05','1:120','1.25'};
        answ = inputdlg(prompt,name,[1 40],defaultans);
        Mag = sprintf('%s*', answ{1,1});
        Mag = sscanf(Mag, '%f*');
        stims = str2num(answ{2,1});
        base = str2num(answ{3,1});
        rx = str2num(answ{4,1});
    case 0
        prompt={'end of stimulation (ms)'...
            'Select baseline number of traces:',...
            'Enter right cut-off range for integration (n x peak latency):'};
        name = 'Amplification';
        defaultans = {'1.05','1:120','1.25'};
        answ = inputdlg(prompt,name,[1 40],defaultans);
        stims = str2num(answ{1,1});
        base = str2num(answ{2,1});
        rx = str2num(answ{3,1});

end
%% channel 1
h = 1;
switch TF
    case 0
        s1 = subplot(1,2,1);
    case 1
end
for g = fieldnames(Ch1)'
    waveform = Ch1.(g{1});
    cap_time_ch1(h)=(waveform(1,1)-t0)/60;
```

```
    x = (waveform(:,1)-waveform(1,1))*1.00e+3;
    y = waveform(:,2)-mean(waveform(min(find(x>
off1&x<off2)):max(find(x>off1&x<off2)),2));
    switch TF
        case 0
            y = y.*1.00e+6;
        case 1
            y = y.*(1000/Mag);
    end
    Ch_1.(g{1}) = [x,y];
    y = sgolayfilt(y,4,23);
    plot(x,y);
    hold on;
    h = h+1;
end
xlim([0 10]);
switch TF
    case 0
        xlabel(s1,'ms');
        ylabel(s1,'nA');
        title('Current');
    case 1
        xlabel('ms');
        ylabel('/muV');
        title('Voltage');
end
%% channel 2
switch TF
    case 0
        h = 1;
        for g = fieldnames(Ch2)'
            s2 = subplot(1,2,2);
                waveform = Ch2.(g{1});
                cap_time_ch2(h)=(waveform(1,1)-t0)/60;
                x = (waveform(:,1)-waveform(1,1))*1.00e+3;
                y = waveform(:,2)-mean(waveform(min(find(x>
off1&x<off2)):max(find(x>off1&x<off2)),2));
                Ch_2.(g{1}) = [x,y];
                y = sgolayfilt(y,4,23);
                plot(x,y);
                hold on
                h = h+1;
        end
        xlabel(s2,'ms');
        ylabel(s2,'mV');
        title('Voltage');
    case 1
end
```

```
xlim([0 10]);

%% grab range for CAP Area analysis
f_names = fieldnames(Ch_1)';
k = 1;
for j = base
    wav = Ch_1.(f_names{j});
    W(:,:,k) = wav;
    k = k + 1;
end
awb = mean(W,3); % average waveform baseline
x0 = awb(:,1);
y0 = awb(:,2);
try
    logic0 = x0>stims;
awbCut = x0(logic0);
[p l] = findpeaks(-y0(logic0),'MinPeakProminence',.2);
%     plot(awb_x,awb_y)
    hold on
    plot(awbCut(l(1,1)),-p(1,1),'k^','MarkerFaceColor','g');
    left = awbCut(l(1,1));
catch
datacursormode on;
dcm_obj = datacursormode(gcf);
set(dcm_obj,'Enable','on');
disp('select LEFT cut-off for CAP Area Analysis, then press ENTER')
ff = msgbox('select LEFT cut-off for CAP Area Analysis, then press ENTER','insert ONE datatip','help');
pause;
c_info2 = getCursorInfo(dcm_obj);
left = c_info2(1).Position(1,1);
end

    wav_x = x0(x0>left);
    wav_y = y0(x0>left);
    MMM = wav_x(wav_y == max(wav_y));
    latBase = mean(MMM);
right = rx*(mean(latBase));
hold on
rr = x0>=left&x0<right;
a= area(x0(rr),y0(rr),'FaceColor',[0 0 0],'LineStyle','none');
a.FaceAlpha = .3;

%% channel 1
h = 1;
for g = fieldnames(Ch_1)'
    i = Ch_1.(g{1});
    x1=i(:,1);
```

```
    y1=i(:,2);
    cap_range=x1(x1>=left&x1<=right);
    cap_area_ch1(h)=trapz(cap_range,y1(x1>=left&x1<=right));
    h = h+1;
end
%% channel 2
switch TF
    case 0
        h = 1;
        for g = fieldnames(Ch_2)'
            i = Ch_2.(g{1});
            x1=i(:,1);
            y1=i(:,2);
            cap_range=x1(x1>=left&x1<=right);
            cap_area_ch2(h)=trapz(cap_range,y1(x1>=left&x1<=right));
            h = h+1;
        end
    case 1
end
%% grab range for CAP amplitude and latency analysis
dcm_obj = datacursormode(gcf);
set(dcm_obj,'Enable','on');
disp('select RANGE for CAP amplitude-latency Analysis, then press ENTER')
ff = msgbox('select RANGE for CAP amplitude-latency Analysis, then press
ENTER','insert TWO datatips','help');
pause;
c_info3 = getCursorInfo(dcm_obj);
range0 = sort(vertcat(c_info3(1).Position(1,1),c_info3(2).Position(1,1)),'ascend')';
left0 = range0(1,1);
right0 = range0(1,2);
    if c_info3(1).Position(1,1)>c_info3(2).Position(1,1);
        xcap0 = c_info3(1).Target.XData;
        ycap0 = c_info3(1).Target.YData;
    else
        xcap0 = c_info3(2).Target.XData;
        ycap0 = c_info3(2).Target.YData;
    end
h = 1;
%% channel 1
for f = fieldnames(Ch_1)'
    i = Ch_1.(f{1});
    x2=i(:,1);
    y2=i(:,2);
    cap_range=x2(x2>=left0&x2<=right0);
    cap_amplitude_ch1(h)=max(y2(x2>=left0&x2<=right0));
    cap_latency_ch1(h)=mean(x2(y2==max(y2(x2>=left0&x2<=right0))))-stims;
    h = h+1;
end
```

```
%% channel 2
switch TF
    case 0
        h = 1;
        for f = fieldnames(Ch_2)'
            i = Ch_2.(f{1});
            x2=i(:,1);
            y2=i(:,2);
            cap_range=x2(x2>=left0&x2<=right0);
            cap_amplitude_ch2(h)=max(y2(x2>=left0&x2<=right0));
            cap_latency_ch2(h)=mean(x2(y2==max(y2(x2>=left0&x2<=right0))))-stims;
            h = h+1;
        end
    case 1
end

%% get all the var, plot and store analyzed data
cap_time_ch1 = cap_time_ch1';
cap_area_ch1 = cap_area_ch1';
cap_amplitude_ch1 = cap_amplitude_ch1';
cap_latency_ch1 = cap_latency_ch1';
switch TF
    case 0
        cap_time_ch2 = cap_time_ch2';
        cap_area_ch2 = cap_area_ch2';
        cap_amplitude_ch2 = cap_amplitude_ch2';
        cap_latency_ch2 = cap_latency_ch2';
    case 1
end

fig2=figure('Name',NameNoExt,...
    'Color', [0.99 0.99 0.99],...
    'Position', [0 round((Pix_SS(1,4)*(1-fig_ysize)/2)) Pix_SS(1,3)
round((Pix_SS(1,4)*fig_ysize))],...
    'Units', 'pixels',...
    'NumberTitle','off');
title('CAP Analysis');
hold on
dot_operator = char(8901);
%% subplot 1
switch TF
    case 0
        sub1 = subplot(1,2,1);
    case 1
end
        sz =75;
        yyaxis left
        scatter(cap_time_ch1,cap_area_ch1,sz,'filled','p',...
```

```
            'LineWidth',.1,...
            'MarkerEdgeColor',[1 0 0],...
            'MarkerFaceColor',[.9 .3 .3]);
        hold on
switch TF
    case 0
        sub1 = subplot(1,2,1);
    case 1
end
        sz =50;
        yyaxis left
        scatter(cap_time_ch1,cap_amplitude_ch1,sz,'filled','o',...
            'LineWidth',.05,...
            'MarkerEdgeColor',[0, 0.4470, 0.7410],...
            'MarkerFaceColor',[0, 0.4470, 0.7410]);
        hold on
switch TF
    case 0
        sub1 = subplot(1,2,1);
        xlabel(sub1,'min');
        ylabel(sub1,strcat('nA',dot_operator,'ms    ',' - ','    nA    '));
        title('Current')
    case 1
        xlabel('min');
        ylabel(strcat('mV',dot_operator,'ms    ',' - ','    /muV    ',' - ','   ms'));
        title('Voltage')
end
        sz =50;
        yyaxis right
        ylabel('ms (peak latency)')
        scatter(cap_time_ch1,cap_latency_ch1,sz,'filled','s',...
            'LineWidth',.05,...
            'MarkerEdgeColor',[0.850, 0.325, 0.098],...
            'MarkerFaceColor',[0.850, 0.325, 0.098]);
        hold on
%% subplot 2
switch TF
    case 0
        sub2 = subplot(1,2,2);
        sz =100;
        yyaxis left;
        scatter(cap_time_ch2,cap_area_ch2,sz,'filled','p',...
            'LineWidth',.1,...
            'MarkerEdgeColor',[1 0 0],...
            'MarkerFaceColor',[.9 .3 .3]);
        sz =50;
        subplot(1,2,2);
        hold on
```

```
    yyaxis left
    xlabel(sub2,'min');
    ylabel(sub2,strcat('mV',dot_operator,'ms     ',' - ','     mV    '));
    scatter(cap_time_ch2,cap_amplitude_ch2,sz,'filled','o',...
      'LineWidth',.05,...
      'MarkerEdgeColor',[0, 0.4470, 0.7410],...
      'MarkerFaceColor',[0, 0.4470, 0.7410]);
    sz =50;
    subplot(1,2,2);
    yyaxis right;
    ylabel(sub2,'ms (peak latency)');
    scatter(cap_time_ch2,cap_latency_ch2,sz,'filled','s',...
      'LineWidth',.05,...
      'MarkerEdgeColor',[0.850, 0.325, 0.098],...
      'MarkerFaceColor',[0.850, 0.325, 0.098]);
    title('Voltage')
  case 1
end

legend('CAP Area','CAP Amplitude','CAP Latency','Location','best')

subdir = [PathName,'Analysis_files'];
  [status, msg, msgID] = mkdir(subdir);
  cd(subdir);
  warning('off',msgID);
file = strcat(subdir,'\',strtok(FileName,'.'),'.xlsx');
strange = strcat(num2str(range(1,1)),'_ms_',num2str(range(1,2)),'_ms');
strange0 = strcat(num2str(range0(1,1)),'_ms_',num2str(range0(1,2)),'_ms');
switch TF
  case 0
    head =
{'time_zero_I',strcat('cap_area_I_',strange),strcat('cap_amplitude_I_',strange0),strcat('cap
_latency_I_',strange0),...

'time_zero_V',strcat('cap_area_V_',strange),strcat('cap_amplitude_V_',strange0),strcat('ca
p_latency_V_',strange0)};
    T = table(cap_time_ch1,cap_area_ch1,cap_amplitude_ch1,cap_latency_ch1,...
     cap_time_ch2,cap_area_ch2,cap_amplitude_ch2,cap_latency_ch2);
    save([NameNoExt,'_Vars'],'Ch_1','Ch_2', 'cap_time_ch1', 'cap_area_ch1',
'cap_amplitude_ch1', 'cap_latency_ch1', ...
    'cap_area_ch1', 'cap_amplitude_ch1', 'cap_latency_ch1', 'strange', 'strange0');
  case 1
    head =
{'time_zero_V',strcat('cap_area_V_',strange),strcat('cap_amplitude_V_',strange0),strcat('c
ap_latency_V_',strange0)};
    T = table(cap_time_ch1,cap_area_ch1,cap_amplitude_ch1,cap_latency_ch1);
    save([NameNoExt,'_Vars'],'Ch_1', 'cap_time_ch1', 'cap_area_ch1',
'cap_amplitude_ch1', 'cap_latency_ch1', 'strange', 'strange0');
```

```
end
writetable(T,file,'Sheet',1);
xlswrite(file,head,1,'A1:H1');
savefig(fig2,NameNoExt);
cd(ScriptFolder);
clearvars -except Ch_1 Ch_2 cap_time_ch1 cap_area_ch1 cap_amplitude_ch1
cap_latency_ch1 ...
    cap_time_ch2 cap_area_ch2 cap_amplitude_ch2 cap_latency_ch2 NameNoExt
PathName strange strange0
```

2. VESSEL DIAMETER – SCRIPT 1

```
/*

 * Macro 1/2 for vessel diameter analysis.

 */

run("Close All");

run("Collect Garbage");

//I define the main directory where the images are

dir = getDirectory("Choose a Directory ");

//I creaet a new folder where the results will be saved called Results

resultsDir = dir + File.separator + "Results" + File.separator;

File.makeDirectory(resultsDir);

//I run the functions that I define down

runConcatenate();

runZProjection();

runFilterForDenoising();

runFilterForBackgroundCreate();

runFilterForBackgroundSub();

//openFiles will open all .lsm of the folder, thus the time series need to be in an exclusive
folder

function openFiles() {

        fileList = getFileList(dir);

        for (i = 0; i < fileList.length; i++) {

                path = dir + fileList[i];

                if (endsWith(path, ".lsm")) {

                        open(path);
```

```
		}
	}
}
function runConcatenate() {
	img = resultsDir + "1) Concatenate.tiff";
	if (File.exists(img)) {
		open(img);
	} else {
		openFiles();
		run("Concatenate...", "all_open open");
		saveAs("Tiff", img);
	}
}
function runZProjection() {
	img = resultsDir + "2) SumSlices.tiff";
	if (File.exists(img)) {
		open(img);
	} else {
		run("Z Project...", "projection=[Sum Slices] all");
		saveAs("Tiff", img);
		}
}
function runFilterForDenoising() {
	img = resultsDir + "3) Median Filter 4 px.tiff";
	if (File.exists(img)) {
		open(img);
	} else {
		run("Duplicate...", "duplicate");
		run("Median...", "radius=4 stack");
		saveAs("Tiff", img);
		close("3) Median Filter 4 px.tiff");
```

```
        }
}
function runFilterForBackgroundCreate() {
        img = resultsDir + "4) Background created 30 px.tiff";
        if (File.exists(img)) {
                open(img);
        } else {
                run("Median...", "radius=30 stack");
                saveAs("Tiff", img);
        }
}
function runFilterForBackgroundSub() {
        img = resultsDir + "4) Background subtracted.tiff";
        if (File.exists(img)) {
                open(img);
        } else {
                open(resultsDir + "3) Median Filter 4 px.tiff");
                imageCalculator("Subtract create 32-bit stack", "3) Median Filter 4 px.tiff","4) Background created 30 px.tiff");
                saveAs("Tiff", img);
        }
}
run("Close All");
showMessage(" -- Listones!!! va 1/3 --");
```

3. VESSEL DIAMETER – SCRIPT 2

```
/*
 * Macro 2/2 for vessel diameter analysis.
 */
run("Close All");
run("Collect Garbage");
//I define the main directory where the images are
```

```
dir = getDirectory("Choose a Directory ");

//I run the functions that I define down

runSegmentation();
runSkeletonization();
runMerge();
function runSegmentation() {
	img = dir + "6) Segmentation.tiff";
	if (File.exists(img)){
		open(img);
	} else {
		open(dir + "5) Registered.tif");
		setAutoThreshold("Li dark");
		run("Convert to Mask", "method=Li background=Dark black");
		saveAs("Tiff", img);
	}
}
function runSkeletonization() {
	img = dir + "7) Skeletonization.tiff";
	if (File.exists(img)) {
		open(img);
	} else {
		run("Skeletonize", "stack");
		run("32-bit");
		saveAs("Tiff", img);
		close("6) Segmentation.tiff");
	}
}
function runMerge() {
	img = dir + "8) Merge.tiff";
```

```
        if (File.exists(img)){
                open(img);
        } else {
                open(dir + "5) Registered.tif");
                run("Merge Channels...", "c1=[7) Skeletonization.tiff] c2=[5) Registered.tif] 
create");
                saveAs("Tiff", img);
                waitForUser ("Draw lines and saved them in manager");
                roiManager("save", dir + "Lines for quantification.zip");


        }
}
showMessage(" -- Listones!!! va 2/3 --");
```

4. VESSEL DIAMETER – SCRIPT 3

```
run("Collect Garbage");
// Line length
N = 60;
// Line width
lineWidth = 5;
// Units of movement
step = 1;
cleanComputedRois();
runLineSweep();


// This is to erase the perpendicular ROIs
function cleanComputedRois() {
        selectWindow("ROI Manager");
        n = roiManager("Count") - 1;
        // for all the ROIs of the manager
        while (n >= 0) {
                roiManager("Select", n);
```

```
		roiName = Roi.getName();
		if (startsWith(roiName, "perp_")) {
			// delete
			roiManager("Select", n);
			roiManager("delete");
		}
		n = n - 1;
	}
}
function runLineSweep() {
	selectWindow("ROI Manager");
	n = roiManager("Count");
	// for all the ROIs of the manager
	resultRow = 0;
	expectedResults = 0;
	for (i=0; i<n; i++) {
		// It is not the first Roi so I check the points
		roiManager("Select", i);
		Roi.getCoordinates(x, y);
		first = 0;
		second = 1;

		if (i > 0) {
			// previous roi
			roiManager("Select", i-1);
			Roi.getCoordinates(x_1, y_1);
			// If the first point if the current ROI is equal to any other point
			// of the previous then that is the first point (p1)
			if ((x[1] == x_1[0] && y[1] == y_1[0]) || (x[1] == x_1[1] && y[1] ==
y_1[1])) {
				first = 1;
```

```
                second = 0;
        }
}

p1_x = x[first];
p1_y = y[first];
p2_x = x[second];
p2_y = y[second];

// Vectors
dx = p1_x - p2_x;
dy = p1_y - p2_y;
dist = sqrt(dx*dx + dy*dy);
dx /= dist;
dy /= dist;
// Calculation of coordinates for the perpendicular points
// to the first point of the ROI
x3 = p1_x + (N/2)*dy;
y3 = p1_y - (N/2)*dx;
x4 = p1_x - (N/2)*dy;
y4 = p1_y + (N/2)*dx;
// Creates the line
makeLine(x3, y3, x4, y4, lineWidth);
// adds it to ROI manager
roiManager("Add");
// Selects the new ROI
roiManager("Select", i+n);
// Change the name
roiManager("Rename", "perp_" + i);
// Here it moves from p1 to p2
// You have to calculate the unit vector between p1 and p2
```

```
// The vector between P1 and P2 is V = (u, v)
// so it is unity vector then you divide by the magnitude of  V:
// sqrt(deltaX^2 + deltaY^2)

dx = p2_x - p1_x;
dy = p2_y - p1_y;
dist = sqrt(dx*dx + dy*dy);
dx = (dx / dist) * step;
dy = (dy / dist) * step;
expectedResults += (round(dist)/step);
//--------------------- Here calculates the FWHM --------------------------
// For each point of the line
z=0;
while(z < round(dist)) {
        for (s = 1 ; s <= nSlices ; s++) {
                setSlice(s);
                getPixelSize(unit, pixelWidth, pixelHeight);
                getDimensions(width, height, channels, slices, frames);

                if (pixelWidth != pixelHeight) {
                        exit("Please select an image with pixel aspect ratio of
one.")
                }

                profile = getProfile();
                profileLength = profile.length;

                X = newArray(profileLength);
                for(k = 0 ; k < profileLength ; k++){
                        X[k] = k * pixelHeight;
                }
```

```
                    Fit.doFit("Gaussian", X, profile);
                    r2 = Fit.rSquared;
                    sigma = Fit.p(3);
                    FWHM = abs(2 * sqrt(2 * log(2)) * sigma);
                    // pone los resultados en la tabla
                    setResult("n", resultRow, resultRow + 1);
                    setResult("Slice " + getSliceNumber(), resultRow, FWHM);
                }
                resultRow += 1;
                // It makes the translation of the ROI
                roiManager("Select", i+n);
                roiManager("translate", dx, dy);
                z += (1*step);
                //print(z, round(dist));
            };
            //print("-----------");
        }
        updateResults();
        print("Expected results: ", expectedResults, " - Actual results: ", nResults);
}
run("Collect Garbage");
showMessage(" -- Listones!!! va 3/3 --");
```